UNIVERSITAT ROVIRA I VIRGILI

ELECTROSPRAY SCALE-UP FOR THE PRODUCTION OF PARTICLES OF PHARMACEUTICAL INTEREST

Nikolas Sochorakis Saloustros

ADVERTIMENT. L'accés als continguts d'aquesta tesi doctoral i la seva utilització ha de respectar els drets de la persona autora. Pot ser utilitzada per a consulta o estudi personal, així com en activitats o materials d'investigació i docència en els termes establerts a l'art. 32 del Text Refós de la Llei de Propietat Intel·lectual (RDL 1/1996). Per altres utilitzacions es requereix l'autorització prèvia i expressa de la persona autora. En qualsevol cas, en la utilització dels seus continguts caldrà indicar de forma clara el nom i cognoms de la persona autora i el títol de la tesi doctoral. No s'autoritza la seva reproducció o altres formes d'explotació efectuades amb finalitats de lucre ni la seva comunicació pública des d'un lloc aliè al servei TDX. Tampoc s'autoritza la presentació del seu contingut en una finestra o marc aliè a TDX (framing). Aquesta reserva de drets afecta tant als continguts de la tesi com als seus resums i índexs.

ADVERTENCIA. El acceso a los contenidos de esta tesis doctoral y su utilización debe respetar los derechos de la persona autora. Puede ser utilizada para consulta o estudio personal, así como en actividades o materiales de investigación y docencia en los términos establecidos en el art. 32 del Texto Refundido de la Ley de Propiedad Intelectual (RDL 1/1996). Para otros usos se requiere la autorización previa y expresa de la persona autora. En cualquier caso, en la utilización de sus contenidos se deberá indicar de forma clara el nombre y apellidos de la persona autora y el título de la tesis doctoral. No se autoriza su reproducción u otras formas de explotación efectuadas con fines lucrativos ni su comunicación pública desde un sitio ajeno al servicio TDR. Tampoco se autoriza la presentación de su contenido en una ventana o marco ajeno a TDR (framing). Esta reserva de derechos afecta tanto al contenido de la tesis como a sus resúmenes e índices.

WARNING. Access to the contents of this doctoral thesis and its use must respect the rights of the author. It can be used for reference or private study, as well as research and learning activities or materials in the terms established by the 32nd article of the Spanish Consolidated Copyright Act (RDL 1/1996). Express and previous authorization of the author is required for any other uses. In any case, when using its content, full name of the author and title of the thesis must be clearly indicated. Reproduction or other forms of for profit use or public communication from outside TDX service is not allowed. Presentation of its content in a window or frame external to TDX (framing) is not authorized either. These rights affect both the content of the thesis and its abstracts and indexes.

UNIVERSITAT
ROVIRA i VIRGILI

Electrospray scale-up for the production of particles of pharmaceutical interest

Nikolas Sochorakis

DOCTORAL THESIS

2018

Nikolas Sochorakis

Electrospray scale-up for the production of particles of pharmaceutical interest

DOCTORAL THESIS

Departament d'Enginyeria Química

UNIVERSITAT ROVIRA i VIRGILI

Tarragona

2018

Nikolas Sochorakis

Electrospray scale-up for the production of particles of pharmaceutical interest

DOCTORAL THESIS

Supervised by

Dr. Joan Rosell-Llompart

Department of chemical engineering

UNIVERSITAT ROVIRA i VIRGILI

Tarragona

2018

Universitat
Rovira i Virgili

Escola Tècnica Superior d'Enginyeria Química

Departament d'Enginyeria Química

Avinguda dels Països Catalans, 26

43007 Tarragona (Spain)

Tel. +34 977 55 96 03

http://www.etseq.urv.es/deq/

In Tarragona, July 5, 2018

I STATE that the present study, entitled "Scale-up of electrosprays for the production of nanoparticles of pharmaceutical interest", presented by Mr. Nikolas Sochorakis for the award of the degree of Doctor, has been carried out under my supervision at the Department of Chemical Engineering of this university.

Signed by the doctoral thesis supervisor:

Joan Rosell Llompart

Aknowledgments

My warmest thanks to Prof. Joan Rosell-Llompart and Prof. Jordi Grifoll-Taverna for their solid support for the completion of this Thesis.

There no more suitable place to thank Nuria Juanpere for her ability to create sense out of chaos.

I also want to thank all my office colleagues and most importantly friends Antonio Carrasco , Evgenii Lliasenko, Elena Alarcon, Elena Barbero, Carlos Hernandez, Laura Escorihuela and Reida Akdemir for their cheerful attitude and happy sparks that discharged the workplace. My special thanks to Dr. Eszter Bodnar, and her wonderful family, for being a gentle guidance in and out of the lab. Another big thank you goes to the guys who fueled this research with generous amount of caffeine the Carlos and Ignaci bros.

I have to mention all the wonderful people that I made friendship with over this whole time outside of the lab, Dr Miriam Jauset Rubio, Dr Llorenc Terrades, Tania Diaz, Dr Nouran Yehia, Oumaya Msehli, Luka Maglione and many others that influenced many decisions

Finally, I want to thank my brother Manos Sochorakis, Dr. Giorgos Vernardos and the PPR group for their patience and resolution.

I would like to aknowledge the personel of the SRCiT especially Lucas Vojkuvka, Mercè Moncusí Mercadé and Núria Argany Figueras for all their valuable help. Ernest Alcarraz, of the ETSEQ machine shop for his valuable insights and Jordi Mare for the help in the electronic systems design.

This work has been supported by the Spanish MINECO under grants DPI2015-68969-P and DPI2012-35687, the Catalan government under grant 2014 SGR 1640, URV project URV-PFRB2-1759 and BES-2013-064098 Spanish fellowship. I want to aknowledge the financial support from the DEW group during the last months of the Thesis completion.

Thank you Dr. Gulsen Betul Aktas for riding with me along this journey.

To my beloved mother and father

Table of contents

Scaling up of extractor-free electrosprays in linear arrays

Summary

Electrospray provides unique atomization of liquids, whereby micro- or nano-droplets with very narrow size distributions are generated. To scale up this process, many electrospray emitters must be operated while keeping the flow rate per emitter unchanged to preserve stability. We have studied the conditions leading to robust spraying in linear arrays of electrosprays in which the counter electrode is far compared to the inter-emitter separation. Strong electrostatic interactions are expected between the spray plumes and the electrified drops which are at the emitters (Taylor cones). In our design, a row of emitter tubes protrudes out of a backplate, and the counter electrode is a flat collector plate set at a high negative potential. In addition, electrodes at both ends of the array enable uniform electrical field conditions, while preventing electrical gaseous discharges. We show that this geometry is scalable without bound, both by electric field computations, as by experiments performed under different geometrical configurations, liquid flow rates per emitter, and electrical conductivities of the liquid (mainly, NaCl/MEG solutions). The onset voltage required to stabilize the spraying at all emitter positions approaches a plateau as the number of operated emitters increases.

The same linear electrospray array setup has been used to generate polymer micro/nano particles loaded with an active pharmaceutical ingredient (API). Our model API was turmeric, a potent anti-inflammatory natural substance that is non-water soluble and therefore suffers from low bio-availability. The API and a highly hydrophilic polymer (PVP) were dissolved in ethanol. The solution has been electrospray dried using the linear electrospray array, resulting in PVP-Curcumin spherical particles of 0.5 µm average size. Micronized particles of a hydrophilic polymer-API formulation, can be considered as a general method, for improving the bioavailability of poorly water-soluble APIs. Position sensitive analysis at areas of interest (AOI) in each spot has been performed using SEM to identify the distribution of sizes and morphology of the deposited micro-particles showing good reproducibility for each batch. Particles accumulate over time on the collector plate, producing ovoidal deposition spots below each of the emitters. These spots are poorly aligned sometimes due to the electrostatic interaction between the neighboring spray-plumes. We show that the spots divergence from the array plane reflects minute misalignment of the emitters from such plane. We have tested the efficacy of a horizontal electrode to restore the symmetry of the deposition spots; aiming to facilitating the eventual recollection of the produced particles in practical scenarios. Apart from a silicon wafer particle collector, we demonstrate that it is possible to deposit particles directly on filter paper, at ambient conditions.

We have also developed a single emitter EHD printing device that can jet-print lines directly on cellulose or nitrocellulose paper with no prior treatment and demonstrate this method by printing a lateral flow biosensor, aimed at inexpensive point-of-care diagnostics. The advantage of our method is that the size of the jet generated upon EHD jet printing is several times smaller than the emitter capillary size preventing clogging. The “inks” are water-based protein solutions without any other polymer addition. We tackled the issue of stabilizing a cone-jet for a high surface tension solution by using a laminar co-axial gas co-flow around the EHD emitter. In addition, for the final lateral flow assembly we have used a novel modular DNA- binding protein that can be modified to detect different DNA targets. Upon detection, the assays produce a colorimetric signal in the form of a line directly on the paper strip. As a conclusion, we have successfully printed nitrocellulose paper-based biosensors for the detection of the human papilloma virus-DNA target.

List of publications and conferences

Publications:

- Sochorakis, N., Grifoll, J., and Rosell-Llompart, J. (2018). Scaling up of extractor-free electrosprays in linear arrays. Chem. Eng. Sci., In Press, https://doi.org/10.1016/j.ces.2018.09.006
- Sochorakis, N,Bodnar,E., Grifol, J., Rosell-Llompart, J.,(2014), Scaling of linearly aligned electrosprays, “2nd Iberian Meeting on Aerosol Science and Technology: Proceedings Book RICTA 2014.” Joan Rosell-Llompart and Jordi Grifoll (Editors). Publicacions URV, Tarragona, 2014. ISBN-13: 978-84-695-9978-5. http://digital.publicacionsurv.cat/index.php/purv/catalog/book/65

Conferences:

- IAC 2018--Oral presentation, St.Louis, Missouri
- RICTA 2018 --Poster presentation, Bilbao, Spain
- RICTA 2017 --Poster presentation (1st award), Barcelona, Spain.
- EAC 2017, 2017 -- Poster presentation, Zürich, Switzerland.
- EAC 2016 --Oral talk, Tours, France.
- RICTA 2016 --Poster presentation, Aveiro, Portugal.
- EAC 2015 --Oral talk, Milano, Italy.
- RICTA 2015 --Poster presentation, Elche, Spain.
- AT2015 -- Poster presentation, Tampere, Finland.
- IAC 2014 -- Poster presentation, Busan, South Korea.
- RICTA 2014 --Poster presentation, Tarragona, Spain

EAC: European Aerosol Conference,
IAC: International Aerosol Conference,
AT: Aerosol Technology,
RICTA: Iberian Meeting on Aerosol Science and Technology

List of figures and schemes

Page

Chapter 1

Chapter 2

Chapter 3

Chapter 4

Chapter 1

Introduction

Since antiquity powders have been in high esteem for masonry, for food preservation, and for medicine. Nowadays we know that surface to mass ratio plays a key role in the physicochemical properties of a material. In the hunt to mass produce these materials, traditional techniques like milling are still in use while new techniques are being developed, such as spray drying. In this context, electrohydrodynamic atomization of liquids is a relatively modern alternative to other liquid atomization schemes.

A typical setup consists of a capillary tube used as electrode, fed with liquid from one side, and its open end positioned against a counter electrode. The liquid flow feed is such that pendent drops are formed at the open end, or tip, of the capillary tube. A high voltage difference is established between the counter electrode and the capillary tip that causes electrical charges initially in the liquid to accumulate at the liquid-air interface. When the electrostatic force exceeds the surface tension force, the pendent drop assumes a conical shape that expels a thin jet through its apex, which is much smaller than the capillary tube internal diameter (Fig 1.1). This shape is termed the Taylor-cone in honor to G. I. Taylor who first developed a mathematical model for it (Taylor,1964). Further downstream, the jet experiences periodic varicose instabilities and breaks-up into a shroud of droplets commonly of a bimodal distribution; the main and satellite droplets. As the droplets travel towards the opposing electrode, depending on their volatility, they may evaporate and shrink to the point the charge to volume ratio will exceed the Rayleigh limit. The same forces that caused the cone-jet formation at the tip, will act to create a secondary in-flight jet emission from the droplet itself, termed “Coulombic explosion” (Hunter and Ray, 2009, Rosell-Llompart et al., 2018). The progeny droplets generated by the coulombic explosion are fractions of the primary droplet, but even so the droplet size distribution range of an electrospray system remains unparalleled and is almost solely dependent on volumetric liquid flow rate.

A wide range of liquid solutions can be electrosprayed and more specifically in this work we are interested in polymer-drug dissolutions. It has been found that according to their size particles can passively target different areas of the body as they cross specific physiological barriers (Banerjee et al., 2016, Saraiva et al., 2016, Islam et al., 2017). In addition, it is possible to engineer particles with complex internal composition (e.g. core-shell particles) by merging two or more liquid streams of suitable chemical compositions within the same Taylor cone (e.g. coaxially) (Rosell-Llompart et al., 2018; Xie et al., 2015). These are all valid reasons to use electrospray in medicinal particle production. However, for the industry to adopt to this technique the production rate should be scaled up from the laboratory scale. To do that the same flow rate through each emitter must be maintained, so multiplexing of emitter sources becomes necessary to achieve higher total throughput.

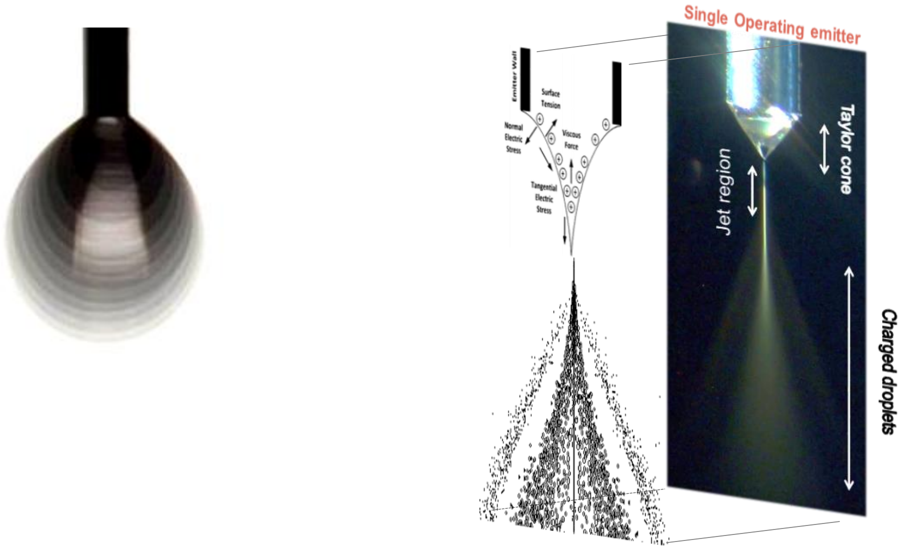

A. High Voltage OFF

B. High Voltage ON

Figure 1.1: A. Droplet formation at the capillary tip when no high voltage is applied (photo overlap), B. Stable cone-jet electrospray as the necessary high voltage difference is established between the capillary and the counter-electrode.

Narrowing down the field of applications to pharmaceutics, we decided to study linear multiplexed electrospray 1-D arrays emitters for the production of polymeric nanoparticles. Linear 1-D arrays simplify droplet-drying for polymer particle generation, a process that may be challenging in denser emitter arrangements; e.g. hexagonal or square 2D geometries.

We executed a parametrical study of an 11-emitter 1-D linear array system, expanded by computational models to a simplified 1-D, N-emitter system. We also show the interactions between plumes and symmetry breaking effect at high voltages

The same 11-needle 1-D linear array setup was used for the production of polymeric nanoparticles. The purpose was to proof-test our system with polymer- API (Active Pharmaceutical Ingredient) loaded liquid. The synthesized polymer particles, made in most cases of poly-vinyl-pyrrolidone (PVP) were loaded with curcumin a substance that is used traditionally in eastern medicine, while recent studies show its potency as a drug (Cartiera et al., 2010, Jurenka 2009).

In the course of this research, we have realized that it was possible to electrospray in the cone-jet mode on paper substrates. Paper is such a widespread, cheap and common material along with its other properties - flexible, biodegradable and recyclable - that incremental improvements in its functionality can have huge impacts in everyday life. For this reason, many research groups have focused their efforts in creating paper-based printable flexible electronics, microfluidic devices and disposable biosensors (Gonzalez-Macia et al., 2010, Wu et al., 2018) More specifically we got interested in lateral flow assay biosensors as no specialized technology is required for their use (Koczula et al., 2016). These devices can reduce the cost, increase the speed and decentralize diagnostics of patients. Lateral flow biosensors generate colorimetric signal in the form of a line as a standard. We present two methods of single step protein deposition on paper-based materials with a single emitter setup. Our initial plan was to use electrospray to deposit a protein solution on the sensor surface and take advantage of the low flow rate and large coverage area owing to droplet repulsion for achieving a stronger colorimetric signal with little amount of deposited protein. We have discovered that the same setup- for higher flow rates- is able to generate a stable and focused EHD-jet. The EHD-jet printed trace has proved ideal, both in speed and accuracy, for our application. However, both techniques- electrospray deposition and EHD-jet printing - are compared and presented in this thesis as alternate methods to already existing biosensor printing techniques, with the emphasis shifted on the later.

References

Banerjee, A., Qi, J., Gogoi, R., Wong, J., and Mitragotri, S. (2016). Role of nanoparticle size, shape and surface chemistry in oral drug delivery. J. Control. Release, 238:176–185.

Cartiera, M.S., Ferreira, E.C., Caputo, C., Egan, M.E., Caplan, M.J., and Saltzman, W.M. (2010). Partial correction of cystic fibrosis defects with PLGA nanoparticles encapsulating curcumin. Mol. Pharm., 7(1):86–93.

Gonzalez-Macia, L., Morrin, A., Smyth, M.R., and Killard, A.J. (2010). Advanced printing and deposition methodologies for the fabrication of biosensors and biodevices. Analyst, 135(5):845–867.

Hunter, H.C. and Ray, A.K. (2009). On progeny droplets emitted during Coulombic fission of charged microdrops. Phys. Chem. Chem. Phys., 11(29):6156–6165.

Islam, M.A., Barua, S., and Barua, D. (2017). A multiscale modeling study of particle size effects on the tissue penetration efficacy of drug-delivery nanoparticles. BMC Syst. Biol., 11(1):1–13.

Jurenka, J. (2009). Anti-inflammatory Properties of Curcumin, a Major Constituent of Curcuma longa: A Review of Preclinical and Clinical Research. Altern. Med. Rev., 14(2):141–151.

Koczula, K.M. and Gallotta, A. (2016). Lateral flow assays. Essays Biochem., 60(1):111–120.

Rosell-Llompart, J., Grifoll, J., and Loscertales, I.G. (2018). Electrosprays in the cone-jet mode: From Taylor cone formation to spray development. J. Aerosol Sci., In press.

Saraiva, C., Praça, C., Ferreira, R., Santos, T., Ferreira, L., and Bernardino, L. (2016). Nanoparticle-mediated brain drug delivery: Overcoming blood-brain barrier to treat neurodegenerative diseases. J. Control. Release, 235:34–47.

Taylor, G. (1964). Disintegration of water drops in an electric field. Proc. R. Soc. A Math. Phys. Eng. Sci., 280(1382):383–397.

Wu, X., Suvarnapathaki, S., Walsh, K., and Camci-Unal, G. (2018). Paper as a scaffold for cell cultures: Teaching an old material new tricks. MRS Commun., 8(1):1–14.

Chapter 2

Scaling up of extractor-free electrosprays in linear arrays

Abstract

Electrospray provides unique atomization of liquids, whereby micro- or nano-droplets with very narrow size distributions are generated. To scale up this process, many electrospray emitters must be operated while keeping the flow rate per emitter unchanged to preserve stability. To cope with the electrostatic repulsion between the various elements in the system, it is common to position the emitters very near a counter electrode. Instead, we have studied the conditions leading to robust spraying in linear arrays of electrosprays in which the counter electrode is far compared to the inter-emitter separation. Strong electrostatic interactions are expected between the spray plumes and the electrified drops which are at the emitters (Taylor cones). In our design, a row of emitter tubes protrude out of a backplate, and the counter electrode is a flat collector plate set at a high negative potential. In addition, electrodes at both ends of the array enable uniform electrical field conditions, while preventing electrical gaseous discharges. We show that this geometry is scalable without bound, both by electric field computations, as by experiments performed under different geometrical configurations, liquid flow rates per emitter, and electrical conductivities of the liquid (mainly, NaCl/MEG solutions). The onset voltage required to stabilize the spraying at all emitter positions approaches a plateau as the number of operated emitters increases. Eventually, as the voltage becomes high enough, the sprays misalign. In this case, the emissions directions are in consonance with minute zig-zag misalignments of the emitters, revealing the importance of small asymmetries in the electrostatic forces.

Keywords:

aerosol, electrohydrodynamic atomization, electrospray, electrostatic spraying, multiplexing, space charge

2.1 Introduction

Electrospray, or *electrohydrodynamic spraying*, is an unparalleled liquid atomization process, whose scaling up remains a challenge. It is based on the stabilization of a liquid jet at the end of electrified conical menisci (called Taylor cones) produced by the action of an intense electric field. This jet undergoes periodic capillary breakup, releasing uniformly sized droplets. Electrospray is capable of producing dense sprays of quasi size-monodisperse droplets, in a wide size range from microns to nanometers (Rosell-Llompart et al., 2018). These droplets have been used for making engineered nano/micro-sized particles with extremely narrow size distributions, or thin films, out of a wide range of materials present in the droplets. In addition, it is possible to engineer particles with complex internal composition (e.g. core-shell particles) by merging two or more liquid streams of suitable chemical compositions within the same Taylor cone (e.g. coaxially) (Rosell-Llompart et al., 2018; Xie et al., 2015).

However, the scaling up of electrospray process is not trivial, as it involves operating multiple Taylor cones in a small space in the presence of strong electrostatic fields. The liquid rate passing through a single Taylor cone is constrained because stabilizing the cone and its jet relies on delicate balances between forces (e.g. interfacial electric and surface tension stresses). For example, to produce micrometer-radius droplets requires a volumetric rate typically of ~10^{-11} m^3/s. Such small rates suffice for analytical chemistry applications of electrospray, namely *electrospray ionization mass spectrometry* or ESI-MS (Fenn, 2003), as a source of particles for calibration of aerosol instruments (Hogrefe et al., 2004; Steiner et al., 2017), or other lab scale experimentation. However, obviously, such low rates do not suffice to meet industrial demands of potential applications.

At lab scale, electrospray arrays have been implemented in virtually every application of electrospray: Pharmaceutical particle synthesis (Almería et al., 2010, 2011; Kawakami, 2012), surface coating (Tang & Gomez, 2015), micro-electronics cooling (Deng & Gomez, 2011), mass spectrometry in nanospray mode (Kelly et al., 2007, 2008a; Mao et al., 2011), microprotein arrays (Bhatnagar, 2007), 3D printing (Wang et al., 2015), micro-combustion (Kyritsis et al., 2004; Deng, Klemic et al., 2007), colloidal spacecraft propulsion (Velásquez-García et al., 2006; Krpoun & Shea, 2009), and nanofiber production by electrospinning (Zhou et al., 2009). Studied geometries include 2D square and hexagonal patterns, and 1D linear and circular ones (Lhernould et al., 2011). Obviously, 2D arrays can accommodate greater emitter density than 1-D geometries. Yet, 1D arrays can be convenient to use when emitter density needs not be extremely high. In addition, drying of the droplets for producing particles is very straightforward in 1D electrospray arrays.

Despite significant progress in this area, reliability continues to be challenging. The multiplexing of electrosprays is dependent on attaining similar electric field at all Taylor cones' positions in the array. This has often been achieved by means of the so-called *extractor electrode*, a perforated plate or a ring which is positioned near each Taylor cone and is set to a different voltage. The droplets pass through an aperture on the extractor electrode, and are attracted to an additional electrode located downstream which holds a suitable electric potential. By keeping a small separation between Taylor cones and the extractor electrode, the cones become electrostatically shielded from one another as well as from the spray charge (Bocanegra et al., 2005; Deng et al., 2006, 2009; Almería et al., 2010). The extractor electrode solution, however, is not without issues, especially when used at atmospheric pressure with 2D arrays and very small droplets (Bocanegra et al. 2005; Deng & Gomez, 2007; Deng et al., 2009; Higuera 2013; Kempen et al., 2016).

Compared to dense 2D arrays, in dense 1D arrays the electrostatic interactions among emitters are significantly reduced; as well as between the emitters and the sprays. Hence, robust operation of dense 1D arrays *without* an extractor electrode should be possible within some region of the operational parameter space. Table 2.1 lists previous studies on the operation and/or design of 1D linear arrays. Such studies have either used extractor electrodes or a droplet collection electrode located near the Taylor cones. The only 1D arrays for which the reported separation between the emitters and the counter electrode was large compared to the emitters' pitch had a pitch of many mm; therefore, such arrays are not considered to be "dense" here (Almekinders & Jones, 1999; Kawakami, 2012). In the present study we consider 1D linear arrays *without* an extractor electrode, in which the droplet collection electrode is at a large distance compared to the emitters pitch. In addition, our capillary tube emitters protrude out of a backplate, set parallel to the collection plate.

We address the question of whether such "linearly dense" arrays of Taylor cones are up-scalable without bound, by studying how the onset voltage scales with the number of operated (spraying) emitters. Since the counter electrode sits far from the Taylor cones, strong electrostatic interactions between the cones are expected, resulting in non-uniform electrostatic field. To offset this issue, several studies (Rulison & Flagan, 1993; Hubacz & Marijnissen, 2003; Quang Tran et al., 2010) have used passive (non-spraying) electrodes at the edges of the array which improve the electric field uniformity (a strategy also used on 2D arrays by Deng et al. 2006). One of our goals has been to assess this question with the constraints of our arrays, and evolve previous designs of such electrodes to obtain robust stability. Another goal of the present work is to report on symmetry breaking of the electrosprays which develops as the applied voltage becomes large enough.

For the experimental work, we have used a common solvent (ethylene glycol) mixed with electrolytes to attain electrical conductivities appropriate to obtain droplets' diameters of order 1 µm. This study includes the following factors: the number of operated emitters, the separation between the collector and backplate, and the liquid volumetric flow rate. A novel method used in this study is the continuous recording of the current-time traces emitted by each Taylor cone, individually, which allows monitoring the stability of the spraying. The experimental methodology has been complemented with numerical solutions of the electric field.

Table 2.1 – Prior studies using 1D-linear electrospray emitter arrays (with > 5 emitters; atmospheric pressure)[1,2]

References (in chrono-logical order)	Kind of study, application	Emitters type	Emitters number x pitch	Extractor plate?	Emitter - counter electrode[3] separation	End electrodes?	Droplet diameter range (µm)
Rulison & Flagan (1993)	Parametric study on array operation	Metal capillary tubes, plus 1 dummy one at each array end	6 × several pitches	No	Not reported	Yes	N.A.
Almekinders & Jones (1999)	Technical note	Sawtooth ("serrations")	24 × 6.5 mm	No	Large (>> 1 cm)	No	112-260 VMD
Kelly et al. (2007, 2008a)	LC / nanoESI-MS	Pulled fused-silica capillaries	19 × 0.5 mm 9 × 1 mm	No	1 mm 1 – 1.5 mm	No	N.A. (< 1, probably)
Kim et al. (2007)	Lab-on-a-chip / nanoESI-MS	Monolithic silica emitters protruding from Si wafer	10 × 0.010 mm	Yes	Not reported (not used)	No	N.A.
Wang et al. (2007)	Biomolecules pulsed deposition	Silica in MEMS device (10 µm emitter diameter)	10 × 0.2 mm	No	0.2 mm	No	N.A.
Quang Tran et al. (2010)	Operation and design	Tubes milled on PMMA	10 × 2 mm	Yes	4 mm	No	N.A.
Mao et al. (2011)	nanoES – MS	Linear Monolithic silica emitters	10 x 0.040 mm	No	Not reported	No	N.A.
Lhernould et al. (2011)	Operation and design	PC slab with holes (I.D. 0.15 mm)	8 x 2 mm	Yes	0.8 mm	No	N.A.
Kawakami (2012)	Pharma particles production	Stainless steel needles (1 mm diameter)	8 × 10 mm	No	150 mm	No	N.A.
Lojewski et al. (2013)	Operation and design	Tubes milled on brass and on PC	51 × 0.5 mm	Yes	Not reported	No	6.5 – 12 d_{10}
Kim & Kim (2014)	Operation and design	Sawtooth, plus 2 dummy teeth at each end	10 × 8 mm	No	10 mm	Yes	16 – 21 d_{10}
Kumar et al. (2018)	Parametric study on array operation	Stainless steel emitters (0.2 mm I.D.)	5 x 1.5 mm	No	2.5 mm	No	N.A.
Zhao et al. (2017)	Technical note	Sawtooth, cut from paper	9 × 3 mm	No	About 5 mm	No	6.9 d_{10}

[1] We have considered only arrays with more than 5 emitters.

[2] Abbreviations: LC = liquid chromatography; MS = mass spectrometry; N.A.= not available; nanESI = nano-electrospray ionization; PC = polycarbonate; PDMS = poly(dimethyl siloxane); PMMA = poly(methyl methacrylate); VMD = volume median diameter

[3] The counter electrode is the extractor electrode, if one is present. It is the mass spectrometer inlet, if one is used.

2.2 Materials and methods

All reagents were used as purchased, without further purification. Sodium chloride (Sigma-Aldrich, ≥99%, AR grade) was dissolved in ethylene glycol (MEG, Scharlau, Reagent grade) at various concentrations using a magnetic stirrer (Table 2.2). Acetic acid (Sigma-Aldrich, glacial) was mixed with H_2O prior to mixing with ethylene glycol. All solutions were prepared at room temperature, and their compositions and electrical conductivities are shown in Table 2.2. These conductivities are consistent with extrapolated values from data reported by Sandengen & Kaasa, 2006.

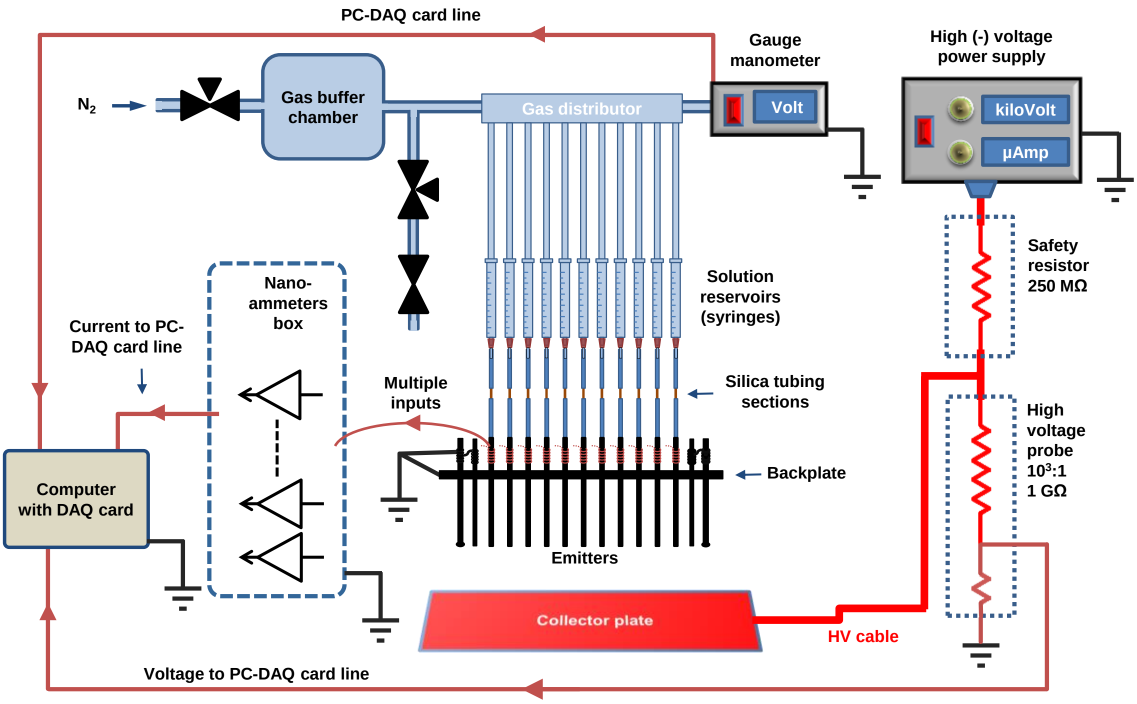

Fig. 2.1. Schematic of the setup.

2.2.1 Electrospray generation setup

The schematic of the setup is shown in Fig. 2.1. A solution is loaded into the liquid reservoirs from which it is supplied to the electrospray emitters when the reservoirs are gas-pressurized. Each reservoir (tuberculin 1.0 mL Henke Sass Wort NORM-JECT syringes without plunger) is vertically positioned and is connected to a 27-gauge × ½" hypodermic needle fitted to a capillary PTFE line (Teknokroma, 360 µm I.D., 580 µm, 550 mm length) which leads to an electrospray emitter tube. To achieve independent control of the liquid supply rate and the applied voltage, in each line we have inserted a short section of fused silica tubing (100 µm I.D., 100 mm length) which elevates the hydrodynamic resistance such that the reservoir gauge pressure exceeded 1 psi. This value greatly exceeds the Laplace pressure at the emitter exit; which is the surface tension coefficient over emitter outer radius $^{\gamma}/_{R}$ (0.015 psi for ethylene glycol). The pressure was measured with a digital manometer and the flow rate were computed from flow rate versus gauge pressure calibrations performed with zero applied voltage.

The electrospray emitters are 100 mm long sections of 304 stainless-steel capillary tubing (Tubos Capilares, Spain; O.D. 400 µm, I.D. 160 µm) square-cut and polished on their exit end. They protrude out of the *backplate*, which is a perforated metal plate held parallel to the collector plate. The support structure rests on the collector *plate* with four Delrin© legs which sit on insulating spacers used for controlling height (not shown). Initially a rectangular brass plate was used as collector. Later on, we added a stainless steel perforated metal plate on top of the collector plate, with absorbent paper sandwiched between the two, to prevent puddle formation due to liquid accumulation. The collector plate and backplate are sized 85 x 235 mm, defining a parallel-capacitor in which the emitters and the electrosprays are shielded from external electrical conditions and perturbations. The emitters are sandwiched in a sub-assembly consisting of two Delrin© mirror blocks with precut groves, press fit together by two screws (not shown). Additional electrodes are placed at the ends of the array, as described later (sec. 3.2). For the 11 emitters at 2.5 mm pitch, the standard deviation for the emitter separations (along the array or x-axis) is only 0.09 mm, and that for the cross-array (y-axis) displacements from a perfect line is only 0.06 mm.

The electric field necessary for electrospraying is provided by a negative high voltage (HV) power supply connected (Ultravolt, HV-RACK-4-250-0032, 0 to -15 kV range) to the collector through a high voltage-rated 250 MΩ safety-resistor so that the electrospray polarity is positive (Chang-Mou et al., 2011). We continuously monitor the applied electric potential at the collector V_C by means of a HV probe (Testec, TT-HVP-40, 10^9 Ω), as shown in Fig. 2.1. The reason for setting the collector at high voltage instead of the emitters is that they and the backplate are earth-grounded through nanoammeters of homemade design (based on op-amp current-to-voltage converter design) housed in a shielded box. The output voltages from the nanoammeters, digital manometer, and high voltage probe are fed to a National instruments PCI 6221 DAQ card on a desktop computer. Fig. 2.2 shows example traces for a typical run in which the collector voltage was adjusted manually at a constant vial pressure (thus steady liquid supply), starting with zero voltage. The current traces show steps when the spraying transitions from one mode to another. In addition, the current is a monotonous function of flow rate. Therefore, differences in current can be used to detect differences on the hydrodynamic resistance of the supply lines, or occasional changes caused by partial clogging.

2.2.2 Imaging of sprays and cones

The spraying modes could be easily identified by following the current traces as well as the liquid meniscus shape at the exit of each emitter tube. The meniscus is imaged best under *brightfield* conditions, for which a LED backlight was positioned behind the emitter array, and the array was imaged from the opposite side (front view). In this case, image contrast arises from attenuation of light by the cones, while attenuation by the sprays is small. To image the spray plumes *darkfield* illumination was used, whereby image contrast arises from light scattered (rather than attenuated) by the droplets. In this case, the backlight was replaced by a black velvet cloth, which provided a dark background, while the sprays were illuminated from two white LED spot lamps positioned symmetrically at roughly 45º from the array mid plane. Additional views of the sprays were taken from a side, in order to reconstruct the directions of the micro-jets in 3D (section 2.5.2). Front view images were shot with an OLYMPUS PEN E-PL7 photo camera with a Nikkor macro lens (60 mm, 1:2.8). Side images were taken with an OLYMPUS PEN EP-1 photo camera and a ZUIKO 14-42 mm zoom lens. Most of the images we show later are enhanced for brightness and contrast, while some are presented with their tone scale inverted ("negative images") to better show the spray outline.

2.2.3 Spraying protocol

Electrospraying was carried in laboratory air, whose temperature (T) and relative humidity (between 35% and 64% for all the experiments) was determined with a Vaisala HM34 meter. A typical experimental run starts with setting the gas pressure to achieve the desired flow rate. Some minutes are required for the pressure to stabilize and for the liquid to fill the lines. Once the flow rate is steady, the data acquisition is initiated, and the applied voltage is ramped-up manually, and pictures are shot frequently. The main spraying modes which we differentiate in the experiments described are the *intermittent cone-jet* and the *steady cone-jet* modes (Rosell-Llompart et al., 2018). The former one, also known as *pulsating mode* (Smith, 1986; Bober & Chen, 2011), is characterized by a lower current level, and is encountered before the steady mode, as voltage is increased. Fig. 2.2 shows several transitions between the two modes, triggered by small adjustments of the collector voltage.

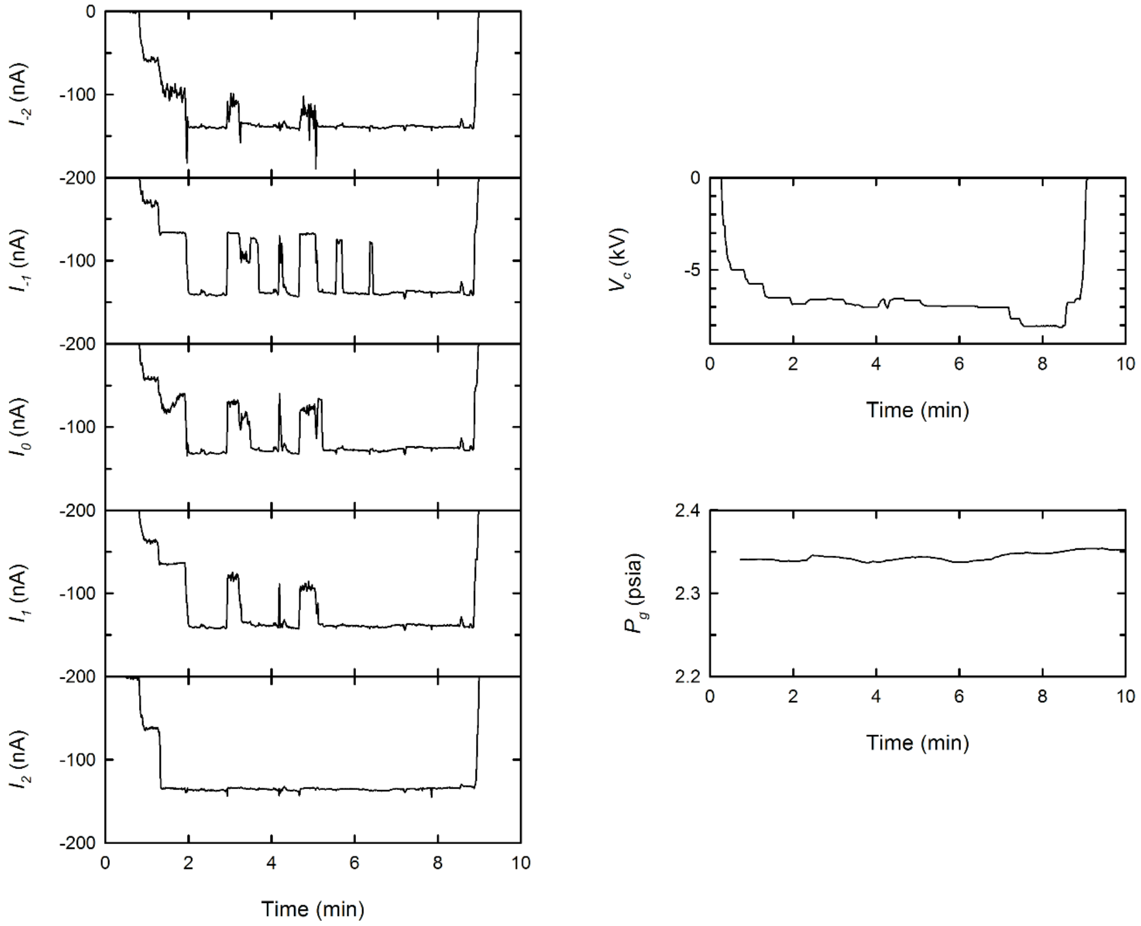

Fig. 2.2. Collected raw data from an example run with a 5-emitter array. The currents are represented by symbols of the kind I_i, where *i* is the emitter index with 0 referring to the central emitter. The collector voltage V_c was varied manually. The gauge pressure P_g is proportional to the liquid flow rate.

Table 2.2 - Solute concentrations and electrical conductivities of ethylene glycol solutions.

Solution code	**Solutes and nominal mass fractions**	**Electrical conductivity, S/m**
SC025	NaCl 0.0025%	4.2×10^{-4} (at 22.8 ºC)
SC027	NaCl 0.0027%	2.9×10^{-4} (at 20.6 ºC)
SC250	NaCl 0.0250%	2.3×10^{-3} (at 24.9 ºC)
SC900	NaCl 0.0900%	1.1×10^{-2} (at 21.5 ºC)
AW	Acetic acid 1.900% Water 3.610%	3.8×10^{-4} (at 21.6 ºC)

2.3 Theoretical approach

2.3.1 Electric field computations

Our experimental array geometries include a backplate, which is a conducting plate located behind the emitters, which are at the same electric potential as the backplate. The two plates (backplate and collector) define a parallel-capacitor gap, which hosts the linear array of emitters and sprays, and shields them from external perturbations. To find out whether dense linear arrays of Taylor cones are scalable without bound, we have investigated how the electric field scales with the number of operated emitters. "Dense" here means that the separation between the emitters' tips and the collector is large compared to the spacing between emitters (pitch). Since we aim to gather physical insights, our numerical computations are for simplified systems: The field due to a linear array of lines-of-charge, which emulate the space charge of electrosprays (section 2.3.2, Grifoll J., 2018), and the field in an array of emitters without space charge (section 2.3.3, Grifoll J., 2018).

2.3.2 Electric field scaling due to space charge (lines-of-charge)

We start by asking how the electric field grows as more lines-of-charge (space charge) are added in the capacitor gap. In our simplified system, each line-of-charge is straight, joining the two conducting parallel plates, and has uniform charge density λ (C/m). The plates are of infinite extent, so we can use the *method of images* to solve the electrostatics problem (Jackson, 1998). In our computation, we assume no voltage difference between the two plates. Fig. 2.3a shows the first few of the infinite series of image charges of a single line-of-charge. The electric field due to the line-of-charge and its first J image lines-of-charge pairs computed at the mid plane between the plates and at a distance x from the line has modulus

$$E_x(x;\ K) = \frac{\lambda}{4\pi\varepsilon_o H}\,\frac{2H}{x}\left\{\frac{1}{\sqrt{\left(2\frac{x}{H}\right)^2+1}} + \sum_{j=1}^{J}(-1)^j\left[\frac{1}{\sqrt{\left(\frac{2x/H}{2j+1}\right)^2+1}} - \frac{1}{\sqrt{\left(\frac{2x/H}{2j-1}\right)^2+1}}\right]\right\} \tag{2.1}$$

Here, ε_0 is the electric permittivity of vacuum, and H is the separation between the plates. The first term inside {...} is the contribution due to the real line-of-charge while the summation over index j is due to its image-charges. This summation must be solved numerically but converges rapidly as J increases (Fig. 2.3b). To be on the safe side, we have used $J = 1000$ in all remaining computations.

Next, we have used this equation to compute the electric field modulus due to a linear array of lines-of-charge, at the array edge and the mid-plane between the plates (Fig. 2.4a): $E_T = \sum_{i=2}^{N} E_{xi}$, where i is the line index, N is the number of lines, and E_{xi} is given by equation (1), where x are the distances from each line i to line 1 (where the field is computed), $x = (i-1)P$. Fig. 2.4b shows how the field modulus at the edge of the array increases as an array is expanded by adding lines, thus increasing the array width W. At values of W comparable to H, the field modulus (data set labelled "total" in Fig. 2.4b) asymptotes out rapidly. This trend is much slower if only the real charges are considered. Therefore, the image charge lines accelerate the convergence. In order words, the electric field due to a line-of-charge becomes strongly shielded by the two plates at distances from the line which are farther than about H. This picture holds true for other line densities as shown in Fig. 2.4c. In fact, the approach toward the asymptote becomes faster for denser arrays (smaller pitch P). As a corollary, in a long array, the electric field strength due to the space charge (lines-of-charge) is nearly zero everywhere except within a distance of about H from the array edge. A similar picture arises in 2D (square $N \times N$) arrays of lines-of-charge between two parallel plates, although the electric field strength is greater, as expected (see Fig. 2.4d).

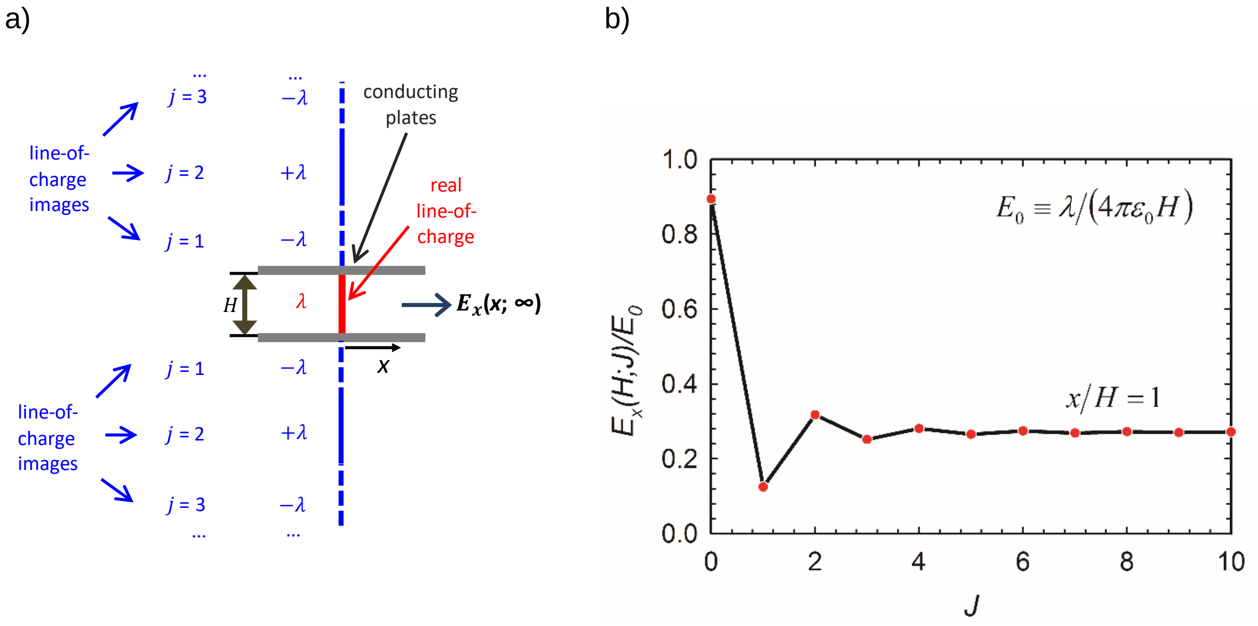

Fig. 2.3. Electric field computation due to a single line of charge placed between two conducting infinite plates. (a) Real and image line-of-charge elements considered in the computation of E_x, the x-component of the electric field computed at the midplane between the two plates, at a distance x from the line-of-charge. (b) Effect of the number of images J considered in the computation of E_x using Eq. (2.1), non-dimensionalized with $E_0 \equiv \lambda/(4\pi\varepsilon_o H)$.

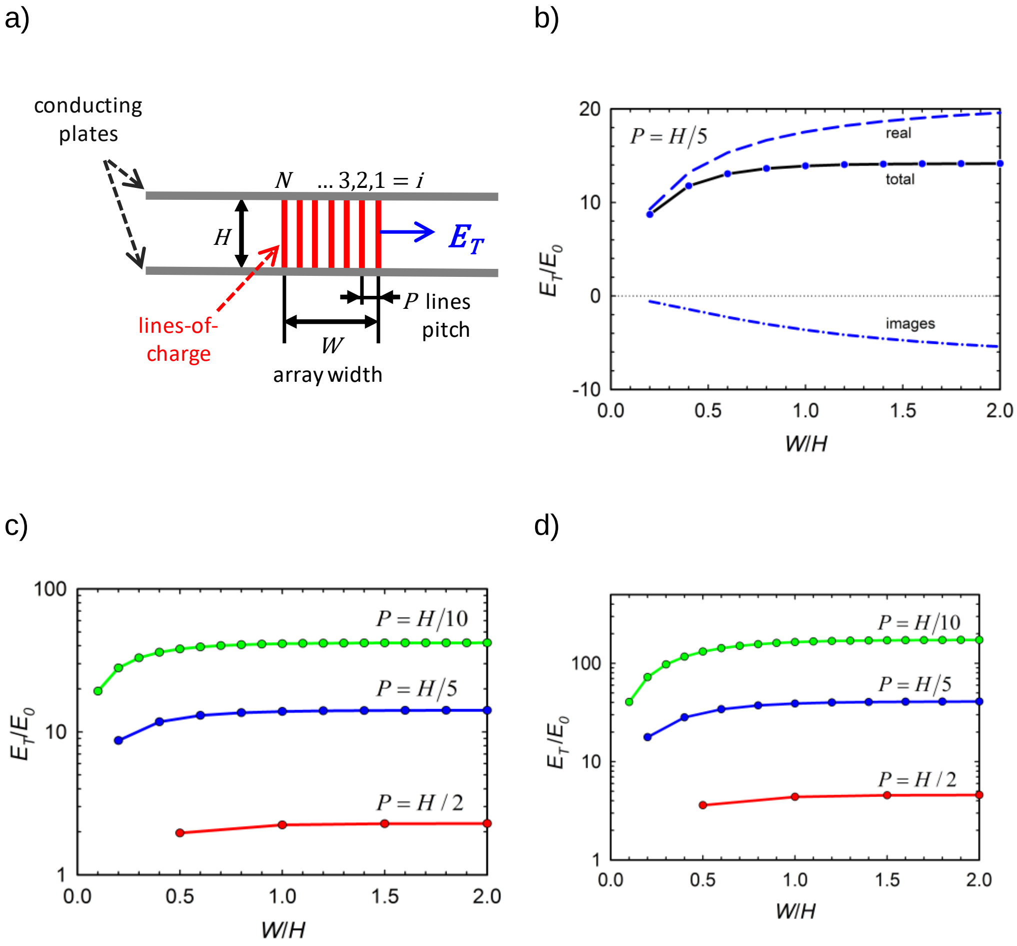

Fig. 2.4. Electric field for a linear array of N lines-of-charge lying across two parallel conducting plates, at the at the edge of the array. a) Geometrical parameters definition and location of the electric field whose modulus is computed. (b) Electric field modulus ("total") and contributions from the "real" charge and its "images". (c) Total electric field modulus *versus* non-dimensionalized array width W/H, for various array line densities H/P. The modulus is non-dimensionalized with $E_0 \equiv \lambda/(4\pi\varepsilon_o H)$. $J = 1000$ in Eq. (2.1). (d) Total electric field modulus calculation at the corner of a square $N \times N$ array of lines-of-charge, at the mid-plane between two parallel conducting plates.

2.3.3 Electric field created by an array of protruding tube emitters

For an array of equally spaced emitters, the electric field at the emitters' tips intensifies towards the two ends of the array. To assess the severity of this "array-end effect" and to guide our designs of array-end passive electrodes, we have solved Laplace's equation for the electrostatic potential ϕ in a linear array of cylindrical electrodes ($\nabla^2\phi = 0$) using COMSOL Multiphysics 5.2. Space charge has been left out for simplicity. In addition, we have assessed the role played by emitter protrusion from the backplate (L). Fig. 2.5 shows the computational domain, taken by symmetry as 1/4 of the whole system. The backplate is set at the same potential as the emitters, like in our experiments. The emitters are terminated with a hemisphere, resembling a pendant drop, to avoid electric field divergences caused by sharp edges (Fig. 2.5c). The geometrical parameters are taken from our experimental geometry.

Fig. 2.6a shows the electric potential ϕ along the x direction at the base of the emitters' cylindrical portion ($y = 0$, $z = -L$) (labelled "equator" in Fig. 2.5c). Minus the slope of the potential, $-d\phi/dx$, is the electric field x-component E_x. For emitters i= 1, 2, 3, the slope of the potential is nearly equal on the two sides of the emitter, the field becoming increasingly asymmetric as the emitters approach the array end. Fig. 2.6b shows the normalized field strength at the equator of the hemispherical cap *versus* the emitter's azimuth (θ_i). The two last positions (i = 5 and 6) "see" an electric field that is significantly stronger and azimuthally less uniform than the other emitters' positions. The near constancy of the field strength for the inner emitters is possible because D is small compared to P.

The effect from emitter protrusion (L) on the field strength is shown in Fig. 2.7. The strength is taken for the central emitter, although its value is similar as for others except at the array ends, as discussed earlier. The field strength increases with L as the backplate shielding reduces, and is expected to approach an asymptote for large L. In other words, the location of the backplate becomes less important as its distance from the emitters' tips becomes large compared to the emitter to collector distance (H). In practice, often one seeks to reduce the range of operating voltages, and, as predicted by these computations, we can decrease the operating voltage by increasing L, but after some L the gain is minimal.

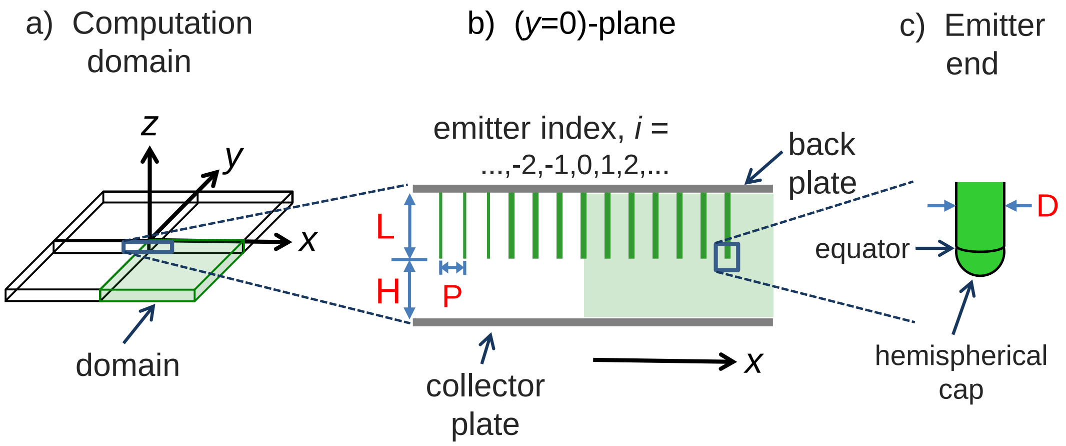

Fig. 2.5. System geometry for electrostatic field computation in absence of space charge.

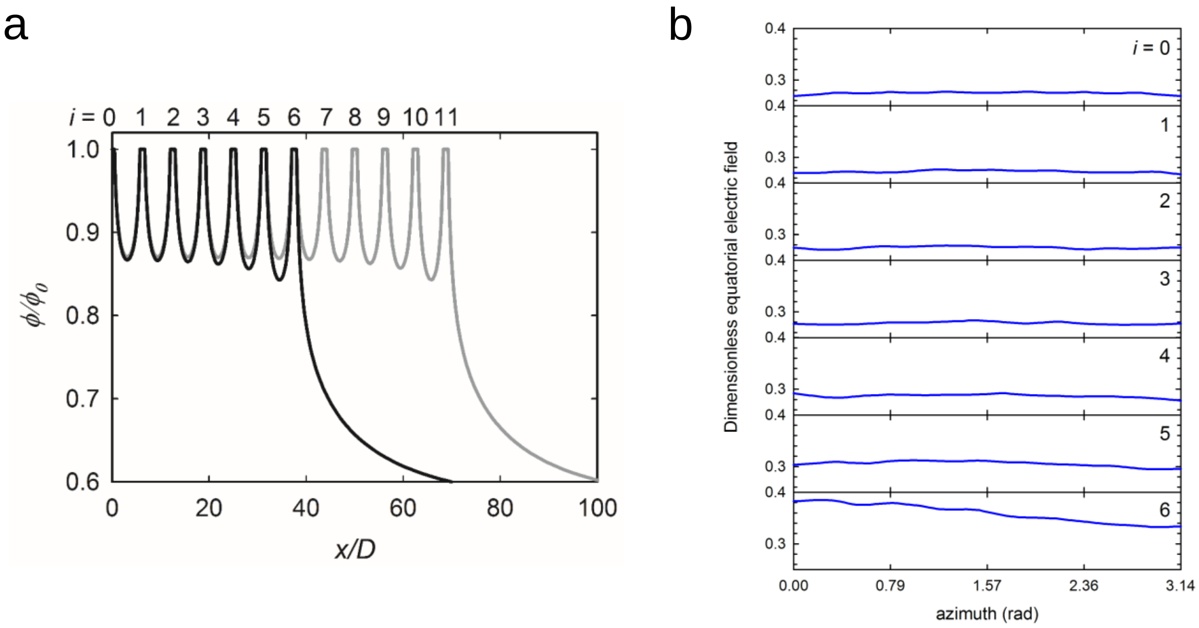

Fig. 2.6. (a) Electric potential ϕ along the line cutting through the emitters' hemispheres' equators (i.e. line $z = -L$; see Fig. 2.5), for a 13- and 23-emitter linear arrays, normalized by the potential difference between plates, ϕ_0. (b) Electric field strength *versus* azimuth on the emitter's hemisphere's equatorial plane. The electric field strength has been non-dimensionalized with $E_0 = \phi_0/D$. Zero azimuth corresponds to the x direction (pointing towards edge of the array). Emitter diameter D = 0.4 mm, pitch P = 2.5 mm, emitter protrusion L = 15 mm, and collector distance H = 20 mm

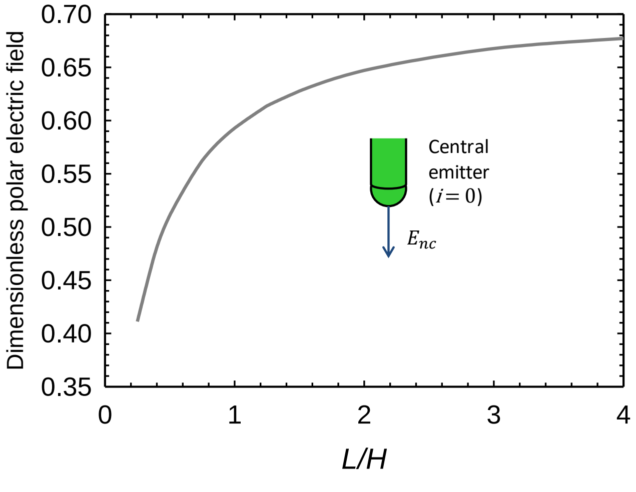

Fig. 2.7. Electric field strength at the pole of the central emitter (see inset) as a function of emitter protrusion from the backplate L, in a 13-emitter linear array as shown in figure 2.5. Emitter diameter D = 0.4 mm, pitch P = 2.5 mm, collector distance H = 10 mm. The electric field strength is non-dimensionalized using $E_0 = \phi_0/D$.

2.4 Designs of electrodes at the array ends and their effects on Taylor cones

The numerical simulations in the previous section tell us that linear arrays of electrosprays can be scaled up without bound, while distortions of the electrostatic field are confined to the array extremes. Encouraged by this conclusion, we proceeded to implement real linear arrays and to study their behavior.

The previous computations advise the use of the two parallel plate geometry to obtain fast electrostatic shielding of the space charge (sec. 3.1.1). In addition, they advise using non-spraying emitter-like electrodes at the two ends of the array, which we refer to as *end-electrodes*. Previous works (Rulison & Flagan, 1993; Quang Tran et al., 2010) have used one passive emitter at each end of a linear array. We, on the other hand, consider end electrodes at the last *two* positions of the array (at both ends), and have considered different geometries for the emitters. Table 2.3 shows the parameters for the array configurations used in this study.

Table 2.3 - Array configurations used in this work (wherein the number of emitters is not reported, as it is considered adjustable for each configuration)

Parameter	Symbol	Array configuration		
		A	B	C
Emitter outer diameter (mm)	D	0.40	0.40	0.40
Emitter pitch (center-to-center separation) (mm)	P	2.5	2.5	2.5
Emitter protrusion from the back plate (mm)	L	16	10.6	23.2
Emitter to collector distance (mm)	H	13	20.4	7.9;10;13
Number of end electrodes on each side of the array	–	2	2	2
End electrode diameter (mm)	–	0.40	0.40	0.40 and 1.2
End electrode protrusion from the emitter ends plane (mm)	–	0	1.6	0

Fig. 2.8 shows three of the end-electrodes configurations that we have tested. The arrays shown differ in emitters' number; but this parameter is immaterial for the present discussion. The first design, configuration A, comprises two pairs of passive emitters, marked with a *. In configuration B, the four passive emitters protrude from the emitters' exit plane, and this change helps straighten the outermost Taylor cones. (Protrusion of the passive electrodes (one on each array terminus) had been previously proposed by Hubacz & Marijnisen, 2003). In both configurations A and B, our system was prone to electric discharges when operating large voltages in air. To address this issue configuration C was developed, in which the end-electrodes do not protrude, and the outermost end-electrode is fat. These end electrodes were made by inserting metal head pins into snug-fitting metal capillary tubing.

As shown in Fig. 2.7, the field strength decreases rapidly with L, as L becomes smaller than H. Therefore, in all the arrays considered here, the emitter protrudes from the backplate by a greater distance than the emitter to collector distance: $L/H > 1$. In this way, the electric field at the emitters' tips is strong enough to electrospray at relatively low voltage.

Array configuration A

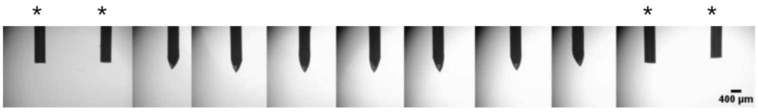

Array configuration B

Array configuration C

Fig. 2.8. Configurations of array-end electrodes used in this study. Such electrodes are marked with a *, while the spraying emitters show Taylor cones. Note that the configuration letter (A, B, C) does not identify the number of spraying emitters, and corresponds to the configurations in Table 2.3. The thin end-electrodes are passive (non-spraying) emitters.

The Taylor cones' shape adjusts itself to changes in applied voltage, to accommodate the condition of steady state. Fig. 2.9 shows that the Taylor cone length and angle are quite sensitive to changes in voltage. If, while liquid is continuously supplied, the voltage (absolute value) is suddenly reduced, the rate at which liquid is removed from the Taylor cone by the electric field decreases; and consequently, the Taylor cone volume increases, thus elongating. At the same time, the cone angle decreases, which intensifies the field strength in that region

(Fernandez de la Mora, 1992). Eventually, the steady-flow condition is restored, as the liquid flow rate passing through the cone and the microjet equates the supply rate.

In Fig. 2.9 we can assess the electric field strength differences *along* the array, by comparing the differences in cone length and seeing how much V_c must change for the center cone to experience the same changes. In panel (c) the field strength differences between the array-end cones and the central cone must be in the order of only a few %, since the cone length difference is less than that experienced by the center cone between panel (c) (-4.95 kV) and panel (b) (-5.16 kV), a 4.2% change.

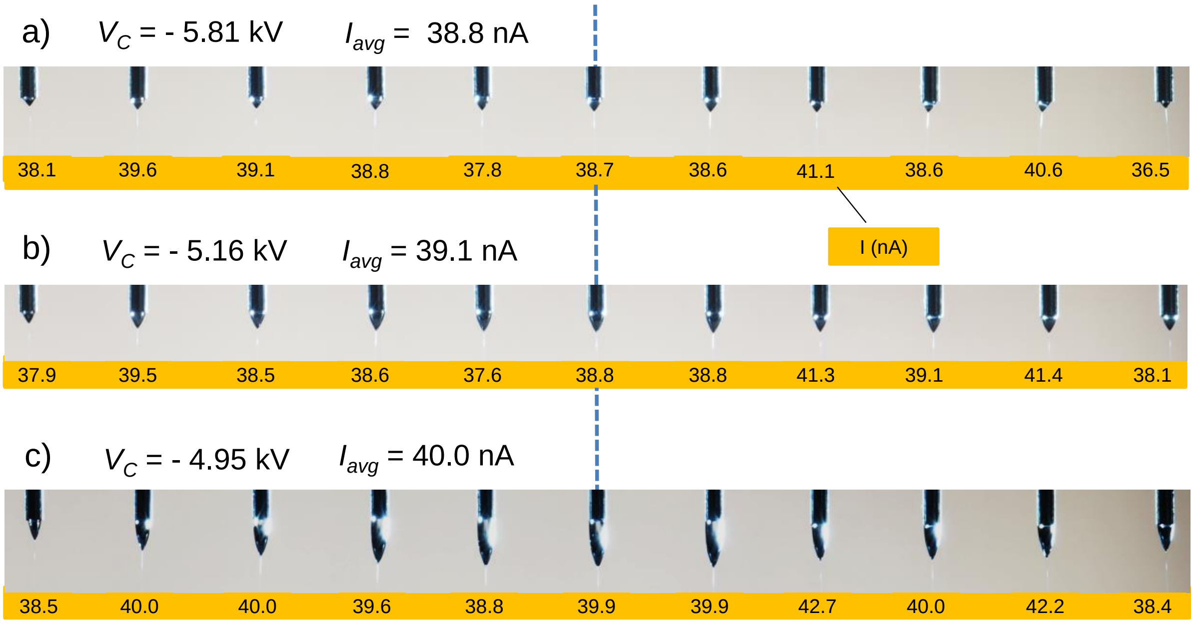

Fig. 2.9. Effect of applied voltage on Taylor cone elongation, in 11-emitter array with configuration C (Table 2.3). Flow rate per needle of 1.58 µl/min; T = 23.5 °C; solution SC025. The dotted line shows the center of the array for reference. Values below the Taylor cones refer to the time-averaged electrical current in nA measured on each emitter.

2.5 Spray plume patterns in the steady cone-jet mode

We have studied how the spray plumes in steady cone-jet mode are influenced by the presence of other spray plumes, and how they evolve with voltage. We also demonstrate the importance of complementing 2D planar imaging with stereoscopic imaging for interpreting the spray plume patterns correctly. First, we compare the plume patterns in the steady and intermittent cone-jet spraying modes. The steady cone-jet mode is characterized by a stationary spray and meniscus in the shape of a cone-jet, while the intermittent cone-jet mode appears when the tip of the meniscus oscillates rapidly, resulting in intermittent sprays. The frequency of the intermittency is usually too high to be perceived, unless a high-speed camera or a fast photodetector is used, but we have easily distinguished the two modes by the difference in meniscus appearance (Rosell-Llompart et al., 2018) and the current traces. Fig. 2.10 shows an array in which some emitters (positions -1 to +4, indicated by an arrow) undergo a transition from the intermittent cone-jet mode (panel (a)) to the steady cone-jet mode (panel (b)) when the voltage is increased at constant flow rate. In the transition, the spray plumes become significantly narrower because, compared to the intermittent mode, the specific charge on the droplets increases. Therefore, they attain higher velocity in the field, thus requiring a longer distance to lose their inertia and start moving electrophoretically (of order $Vo\times \tau$, where Vo is the initial speed and τ is the droplet dynamic relaxation time; Rosell-Llompart et al., 2018). On losing their inertia, the droplets are seeded into more "centrally" located electrophoretic paths than in the intermittent mode case, leading to a narrower plume spread. The figure also shows that in the intermittent mode the sprays overlap at the edges, while sprays in the stable cone-jet mode are clearly separated. The crossing of different electrophoretic trajectories in the steady state is impossible for a mono-mobile charged aerosol (since the droplets' velocity vector equals the sum of the gas velocity and the product of electric field and the droplet's electrical mobility – constant for the mono-mobile aerosol-, and both of these vectors are uniquely defined in space). Therefore, the overlapping of the intermittent sprays is either due to sprays falling on different planes (more likely) or due to intermittent changes in the electric field recorded in the single long-exposure image (less likely).

This experiment also shows differences in the repulsion between the sprays in the different modes. The sprays in positions -2 and +5, are clearly re-oriented (repelled more) after the transition, reflecting that the space charge in the space occupied by sprays -1 to +4 has increased when they go from intermittent to steady cone-jet mode. On the other hand, the sprays in cone-jet mode in positions -5, -4, -3 are virtually identical before and after the transition.

2.5.1 Spray patterns uniformity near minimum voltage

Based on the calculations from section 2.3, we would expect to find two distinct regions in a very long linear array of electrospray emitters (at least, in the backplate-and-collector "condenser" configuration, considered here): An "inner" region, in which the sprays are unaffected by the actual length of the array, and two "outer" regions, located at either end of the array, where "end effects" are concentrated. This is the result of the fact that the electrostatic repulsion from faraway sprays do not amount to a relevant force. To check whether this picture holds in reality, we have determined the sizes of these regions by following the evolution of the spray plumes as a function of the number of operated emitters for a given array N_{on}. The comparison is made at near the "onset voltage" V_{up} condition, namely at the applied

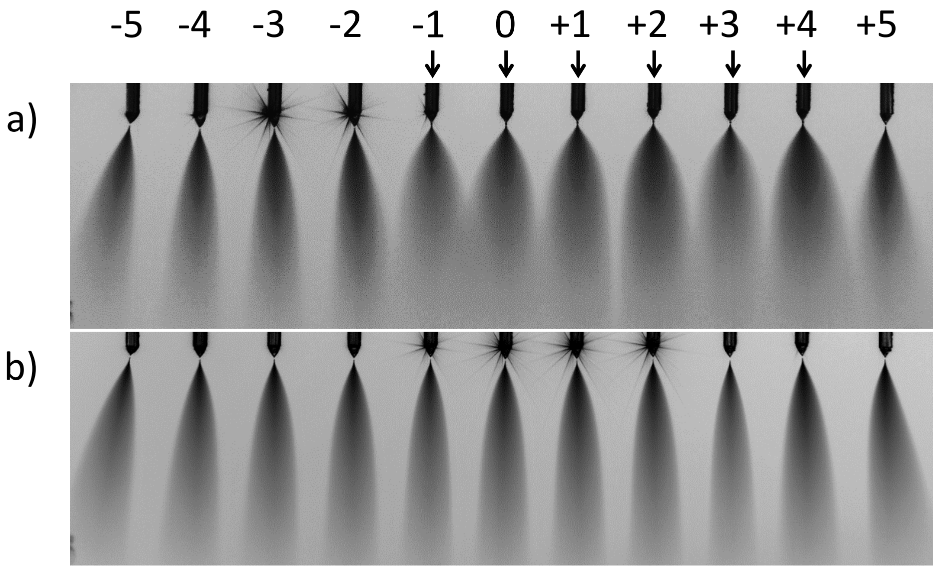

Figure 2.10. Images of electrospray plumes from 11 emitters, a) The arrows indicate the emitters in the intermittent cone-jet mode where V_c = -6.3 kV (I_{avg} = 62.8 nA). b) All the emitters transient to the steady cone-jet mode as the collector voltage was raised to -6.7 kV, (I_{avg} = 135.5 nA). Array configuration B, flow rate per needle Q = 0.5 µL/min, solution SC900, distance from needle tip to collector H = 8.3 mm, P = 2.5 mm and T = 21.9 °C. These images were obtained from darkfield photographs after inverting the tone scale.

voltage for which all the emitters in the array have attained the steady cone-jet mode from the intermittent mode. The recorded individual current traces have allowed us to accurately pinpoint these voltages. Fig. 2.11 shows the evolution as N_{on} grows from 1 to the maximum possible number for two different size arrays, with N = 7 and 11. At each condition the voltage is the one at which the *last* emitter in the array has stabilized into the steady cone-jet mode. Note that this voltage increases as N_{on} is raised. This is probably due to the increased space charge. Similarly, the voltages in figure 2.11b are comparatively higher than in 2.11a for the same equal number of sprays, and this can be attributed to the larger liquid conductivity (K) for the former causing increased space charge.

The plumes geometry is symmetric about the central emitter (position i=0). The plumes are clearly separated (i.e., do not overlap), while the spray plume widths increase with emitter index i. For both arrays (Fig. 2.11) the central plume (i=0) gets narrower as N_{on} increases from 1 to 3, and from 3 to 5, but does not change appreciably from 5 to 7, and so on from 7 to 9, and to 11 in the larger array (Fig. 2.11b). Similar trends are observed with the next emitter positions, i = +1, -1, as their circumstance changes from being at the array edge to being in the "inner region" of the array. We observe that the "edge region" of the array defined above appears to occupy one or at most two sprays at either end of the array.

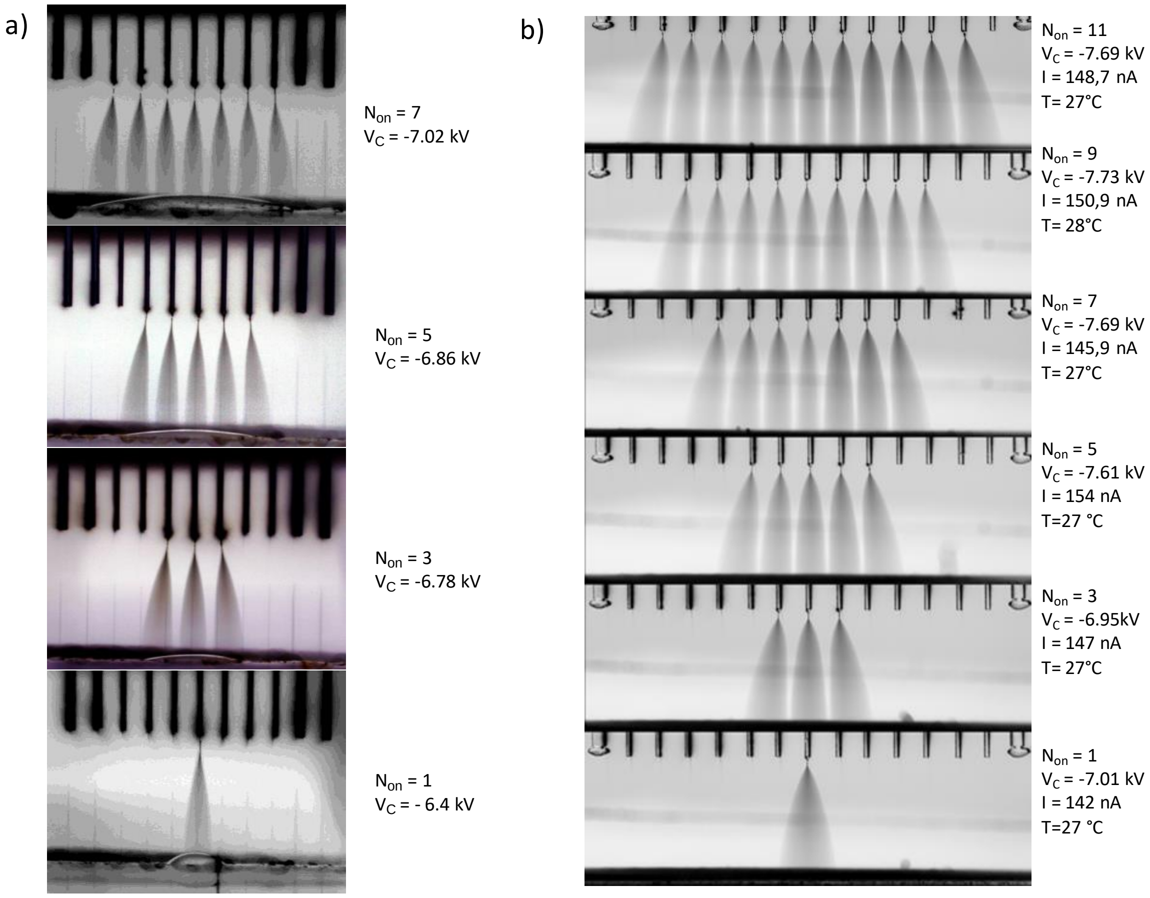

Fig. 2.11. Evolution of the spray pattern as a function of the number of operated emitters when the voltage is near the onset value (V_{up}) in a 2.5 mm pitch array of a) 7 emitters, and b) 11 emitters. Conditions: (a) Solution = AW, end electrode configuration A, H = 13 mm, L= 16 mm, Q = 0.76 µl/min. (b) solution = SC250, end electrode configuration C, H = 10 mm, L = 23 mm, Q = 1.3 µl/min. Common to (a) and (b): P = 2.5 mm. The vertical lines visible on the (a) panels are reflections of the light source on the emitters. Inverted grey tone brightfield images. Q and I are the average per emitter. I is not available for the 7-emitter array runs. Some liquid accumulation is visible in panels (a).

2.5.2 Symmetry breaking at high voltages

At high enough values of the applied voltage (raised at fixed liquid flow rate), the Taylor cones bend away from the emitter axis. Meanwhile, the sprays adopt asymmetric static shapes, as shown in Fig. 2.12. At this condition, the cones retract, becoming small and difficult to visualize; while the light scattered from the various sprays differs in intensity despite being in the same mode. For these reasons, the individual current traces can be a useful tool for identifying the cone-jet mode.

As discussed in section 2.3, when the voltage is raised at constant flow rate, the Taylor cone-jet momentarily experiences an increased electric pull, and the cone becomes shorter ("retracts" towards the capillary). Simultaneously, since the droplets' speeds increase (while the droplet mobility is not significantly affected), the spray space charge is reduced, hence reinforcing the field strength in the cone-jet region. On further increases in applied voltage, the cone-jet retracts further, but eventually must tilt. Tilting of the Taylor cone is a familiar phenomenon in conventional electrospraying from single emitters without extractor. Yet to our knowledge the underlying mechanism has not been discussed in the literature. We know that the specific direction of the jetting is repeatable in each experiment, but we ignore what determines it. We may list as potential factors: (i) imperfections in the emitter leading to asymmetries in the liquid flow, and (ii) asymmetries in the electric field surrounding the Taylor cone (the so called "far field"). Category (i) includes both imperfections at inner emitter surfaces which can induce asymmetric hydrodynamics, and different outer emitter morphology and/or composition which can induce non-symmetric wetting conditions, influencing the contact line. The use of a linear array allows us to probe into the role of category-(ii) factors, i.e. the asymmetries in the electric field. We can see in Fig. 2.6b that the electric field is slightly more intense on the two "exposed" sides of the emitter (angles $\pm\pi/2$) than on its "within array" sides (angles 0 and pi). In addition, emitters closer to the array edge experience stronger field (Fig. 2.6a and b). Finally, the field may be influenced by emitter misalignment.

We have used stereoscopic imaging to determine the direction at which each of the jets aims, as shown in Fig. 2.13. The array was not perturbed between the two experiments; the only difference in configuration being the height of the emitter ends relative to the collector plate (H). Panels (a) and (b) show the front and rotated views of the sprays. These images are used to determine the $(\Delta x, \Delta y, \Delta z)$ location of a point on the jet relative to the center of the tip of its emitter. The point on the jet is chosen in all cases to be relatively far downstream from the Taylor cone, near the end of the straight section of the jet, before it "flares out" as a spray. Therefore, it may be located downstream the actual jet breakup point. These "jet" coordinates are then plotted with the (x, y) positions of the emitters in the top views of panel (c). The emitters' coordinates are independently obtained from a bottom view photo of the emitter array taken in absence of liquid and voltage (not shown), obtained by means of a mirror at 45º from the camera's optical axis. A rotated view of a low voltage condition for which the sprays are straight is provided in Fig. 2.13d for comparison. Fig. 2.14 shows another case.

Comparing panels (c) between Figs. 2.13 and 2.14, we find that the jets' positions relative to the emitters are very similar with only one exception (i = -4), and that they do not follow any symmetric pattern about the central emitter. To understand how the jets "choose" a particular direction, it helps to analyze each side of the array separately. On the left side, the emitters' misalignments and jet directions follow a zig-zag pattern (except for the end emitter, i = -5, in Fig. 2.13), and are correlated. The jets' are deflected toward the same side as their emitter misalignment in the y-direction. This suggests that the emitters' misalignments distort the electric field sufficiently. On the right side of the array, the emitters are aligned better, and this may explain why there is no zig-zag pattern in this case, as their jets mostly aim toward one side of the array (y<0). Therefore, other factors are at play. This experiment does not resolve what these factors are, but may be related to the emitter geometry, as mentioned earlier, or wetting. That the electric field is not the sole factor can be seen by the fact that many jets point toward the array center, while the electric field should be pointing outward (see section 2.3.1).

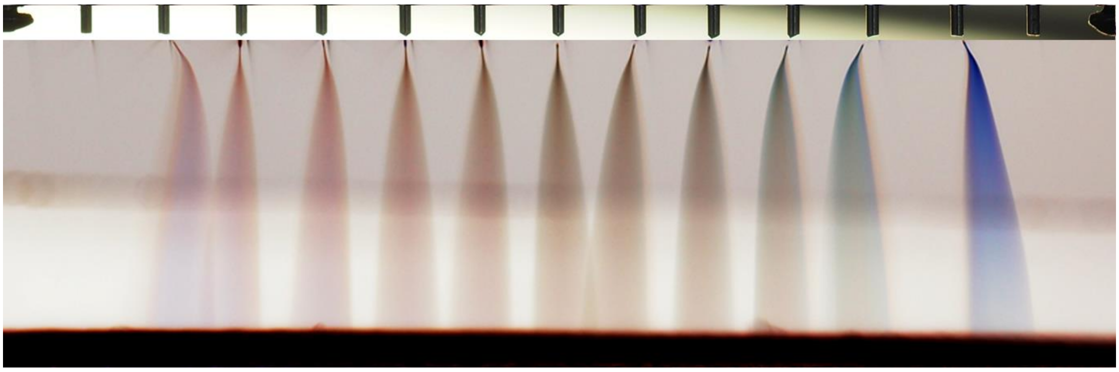

Fig. 2.12. Composition of a bright-field image (top) and the tone inverted dark-field image (bottom) of the linear array. Parameters V_c = 9.17 kV, H = 10 mm, solution= SC250, T = 27.1 °C, Q =0.6 μl/min, I = 99.5 nA (Q and I are per emitter.).

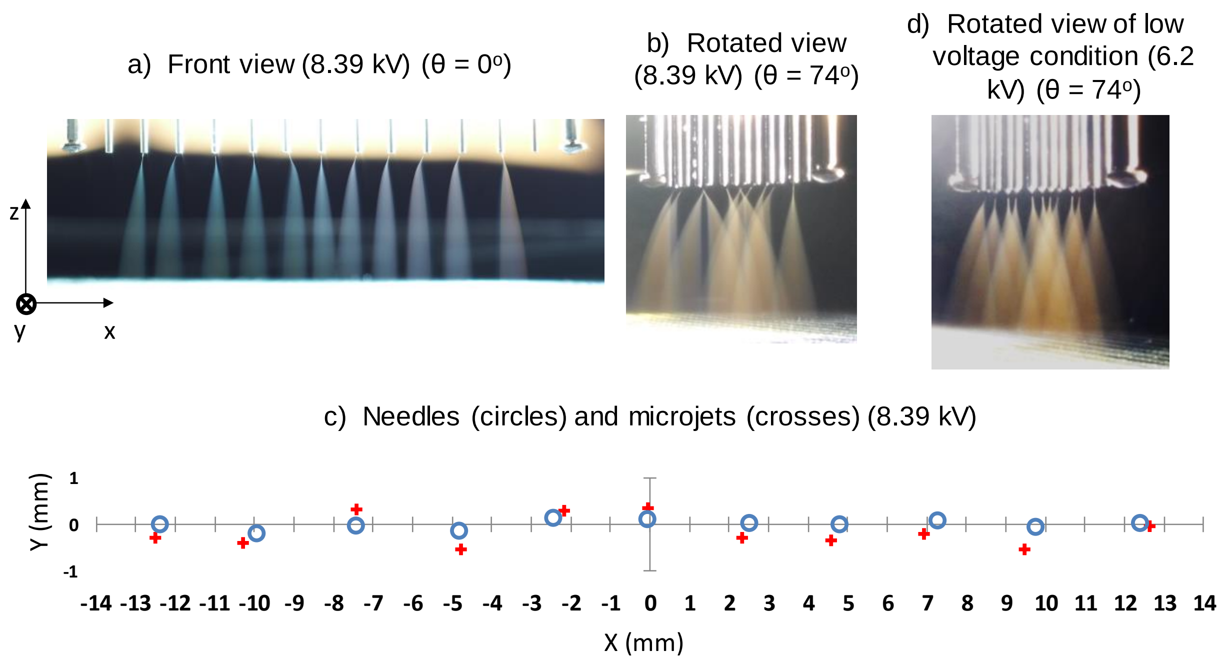
a) Front view (8.39 kV) (θ = 0°)

b) Rotated view (8.39 kV) (θ = 74°)

d) Rotated view of low voltage condition (6.2 kV) (θ = 74°)

c) Needles (circles) and microjets (crosses) (8.39 kV)

Fig. 2.13. Stereoscopic reconstruction of the azimuthal angle of the cone-jet in a high voltage situation for 11-emitters array (P = 2.5 mm, H = 7.9 mm). a) Front view. b) View rotated to the right (by 74° off the front-view optical axis). c) x-y positions of the emitters (circles) and the microjets (crosses) (see text). Q = 0.6 µl/min, V_c = -8.39 kV, I= 79 nA, T= 24°C, solution = SC250. d) Rotated view of a lower voltage condition, shown for comparison (V_c = 6,2 kV, I = 83 nA, other parameters being the same as for b)). (Q and I are per emitter.)

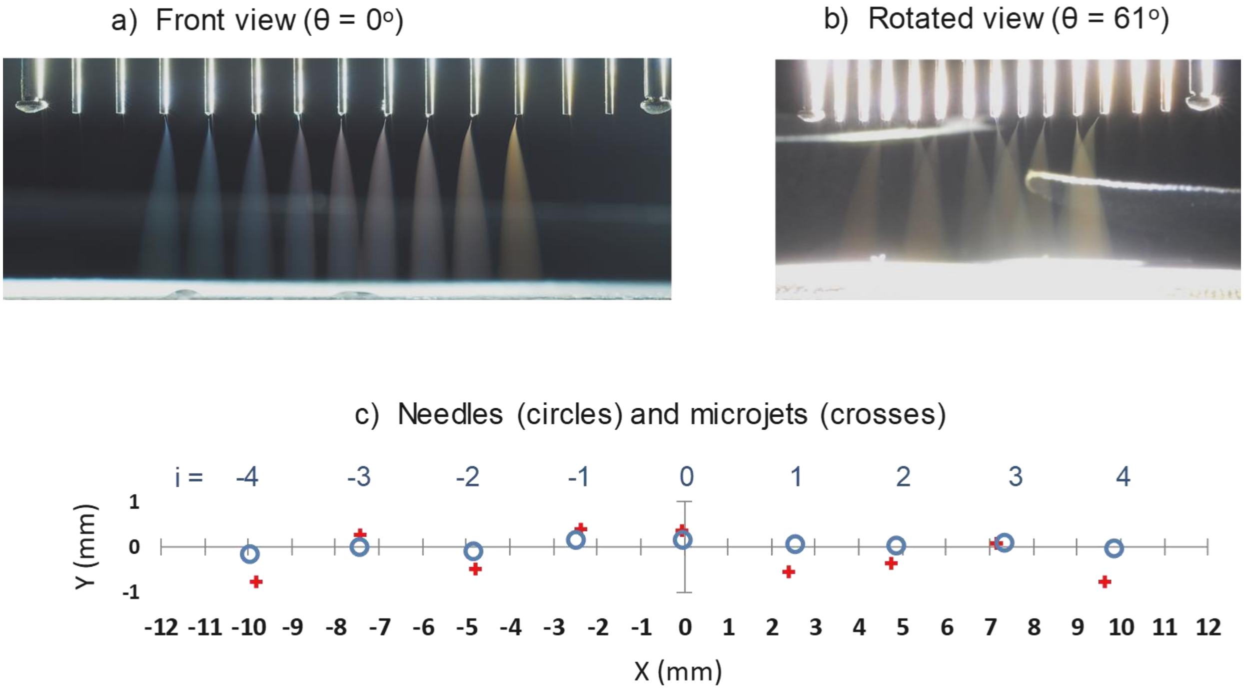
a) Front view (θ = 0°)

b) Rotated view (θ = 61°)

c) Needles (circles) and microjets (crosses)

Fig. 2.14. Stereoscopic reconstruction of the azimuthal angle of the cone-jet in a high voltage situation for 9-emitters array (P = 2.5 mm, H = 10 mm). a) Front view. b) View rotated to the right (by 61° off the front-view optical axis). c) x-y positions of emitters (circles) and the microjets (crosses) (see text). Q = 0.5 µl/min, V_c = 7,23 kV, I= 82 nA, T= 28°C, solution = SC250.

2.6 Cone-jet mode transitions near the onset voltage

The transition from intermittent to steady spraying happens at a critical condition of the electric field acting on the liquid in the Taylor cone region. The changes in spraying mode can be identified for each emitter as jumps in current (see Fig. 2.2). This capability has allowed us to investigate how uniform the electric field stays along the array, for different arrays and operating conditions. In addition, we address whether the electric field in the central region of the array becomes bounded as the number of operated sprays is increased as done in Fig. 2.11.

2.6.1 Taylor cones stabilization and destabilization sequences within the array

Using the 11-emitter array with end-electrode configuration C, we have studied the order in which the spraying stabilizes in the cone-jet mode for each emitter in the array, as the applied voltage is raised, and as a function of the number of emitters being operated, N_{on}. These configurations always include the center emitter, and N_{on} attains values 1, 3, 5, …11. For each configuration, we have scanned the collector voltage to determine V_{up}, the *onset voltage* for the steady cone-jet spraying at each emitter, and once all of the emitters are in steady cone-jet mode we have lowered the voltage to determine, V_{down}, the *minimum voltage* at which the steady cone-jet mode is no longer be sustained and the intermittent mode sets in. V_{up} and V_{down} do not coincide, due to a hysteresis well known for individual emitters (Smith, 1986). For convenience we refer to positive voltage values, i.e. minus the collector voltage values.

Fig. 2.15 shows the V_{up} versus emitter position for different combinations of spraying-emitter number N_{on}, flow rate per emitter Q, and emitter-to-collector distances H. We find that the onset voltage at each position in the array increases with N_{on} and with Q. This result implies that the spray electric charge (space charge), which increases with these parameters, influences the electric field strength at the Taylor cones. As more sprays are turned on, the repulsive force exerted by the sprays on the Taylor cones increases, thus weakening the electric field in that region, which must be overcome by an increment in the voltage to achieve enough field strength to sustain a stable Taylor cone. However, for the centrally located emitters (i = 0 and ±1), this effect weakens or disappears as the number of sprays becomes large enough. For them, the onset voltage tends to a plateau value. When the plateau condition is approached by an emitter, the repulsive forces from the additional sprays contribute negligibly to the weakening of the field at the emitter in question. These observations confirm the existence of two kinds of regions in long arrays, an inner region and two outer regions near the array edges.

We also confirm that the electric field is stronger near the edges of the array, since this is where the transition to the steady cone-jet mode is met first. (Note that the voltage differences between array center and edge would get wider if the passive end electrodes were absent, possibly even preventing stabilization of the entire array.) The electric potential difference at the mode transition depends on any factors influencing the electric field, including the geometry of the electrodes and the presence of space charge. Therefore, in a linear array *without* extractor plate such as ours, it is not surprising to detect this transition at different voltage values for different emitter positions.

The role played by space charge is revealed also in the transient behavior of the sprays at the voltages preceding complete stability, while still some of the sprays are in the intermittent mode. In this "transient regime" sprays flip-flop transiently into and out of the cone-jet mode. As one spray in intermittent mode becomes stable, a neighboring spray already in that mode will feel a decrease in field strength due to the increased space charge, and may therefore revert to the intermittent cone-jet mode. Such cross-talk between sprays is more pronounced at large Q and H (due to the increased space charge), revealed in more frequent "flickering" of the sprays, and the sudden global stabilization of the array when a critical value of the voltage was reached. This is the case for $Q =$1.9 µL/min and $H =$ 10 mm at which V_{up} is flat across much of the array (Fig. 2.15).

Figure 16 shows the onset voltage at which all the emitters have stabilized for a given Q, as a function of number of operated emitters, at three different H. This onset voltage tends towards a plateau as expected from the trends observed in Fig. 2.15. For collector distance H of 13 mm, at high enough voltage a corona and in some cases, spark discharges were audible. Although these took place at some unknown location on the collector electrode edges, they interfered with the current measuring equipment. Therefore, as a precaution, for these experiments the current data acquisition was disconnected, and the mode transitions were identified by changes in the Taylor cones and the spray plumes. However, no gaseous discharges were present for the data points shown.

Fig. 2.17 shows V_{down} for similar parameters. We would expect to find similar trends as for V_{up} except for a space-charge dependent shift in the transition voltages, responsible for the well-known hysteresis mentioned earlier. The transition is observed sooner (i.e. at higher voltage) in the central emitters, where the field is weaker and the Taylor cones are more elongated (Fig. 2.9c), than at the outer emitters, where the field is strongest. Unlike for V_{up}, we do not find for V_{down} in Fig. 2.17 a monotonous dependence on the number of operated emitters. Here too, we observe in some cases that the transition of a single spray causes the destabilization of neighboring sprays in cascade, resulting in the flat portions of the curves shown in Fig. 2.17. In this case, destabilization in one spray leads to reduced space charge, and therefore the field strength intensifies at nearby spraying emitters. However, instead of reinforcing the steady cone jet mode, the sudden intensification of the electric field causes destabilization. Perhaps such sudden perturbations result in the emission of a large fragment from the meniscus causing a drop in the field at the liquid meniscus, which then transitions into the intermittent cone-jet.

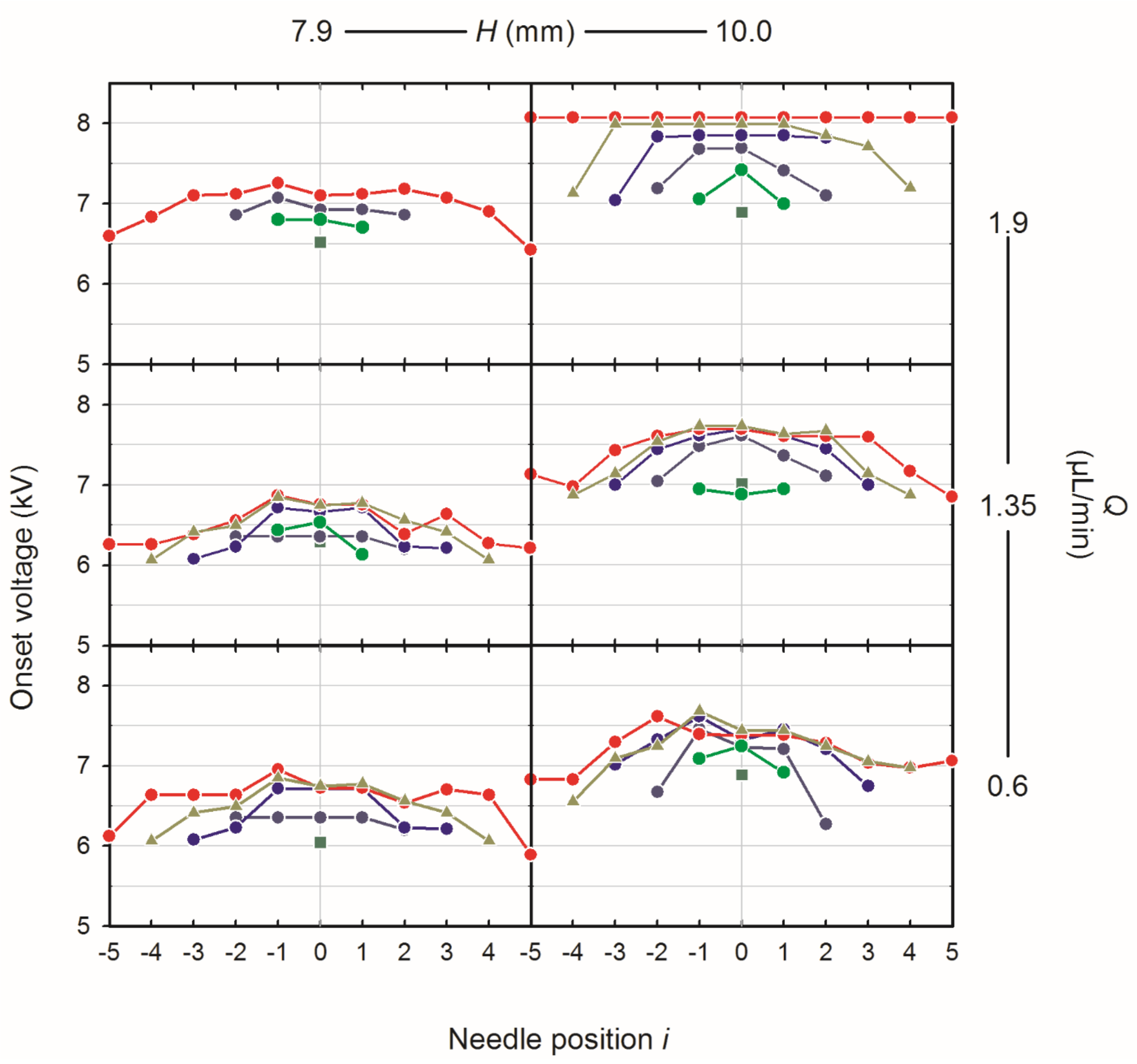

Fig. 2.15. Stabilization sequence into the cone-jet mode for the 11-emitter array, as minus the collector voltage is slowly increased, for different H and Q values. The graphs show the voltage (minus voltage applied on the collector plate) at which each emitter transitioned into the steady cone-jet mode (V_{up}) *versus* emitter position i. Liquid= SC250, configuration C. Q is the flow rate per emitter.

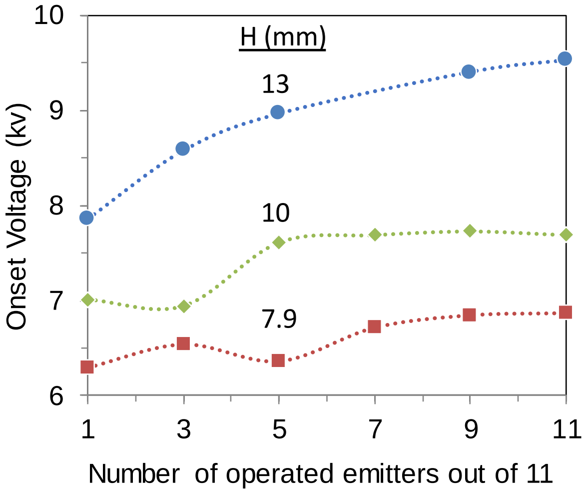

Fig. 2.16. Onset voltage for the 11-emitter array versus number of operated emitters at different emitter to collector separations. The flow rate is the same for all (1.35 μl/min).

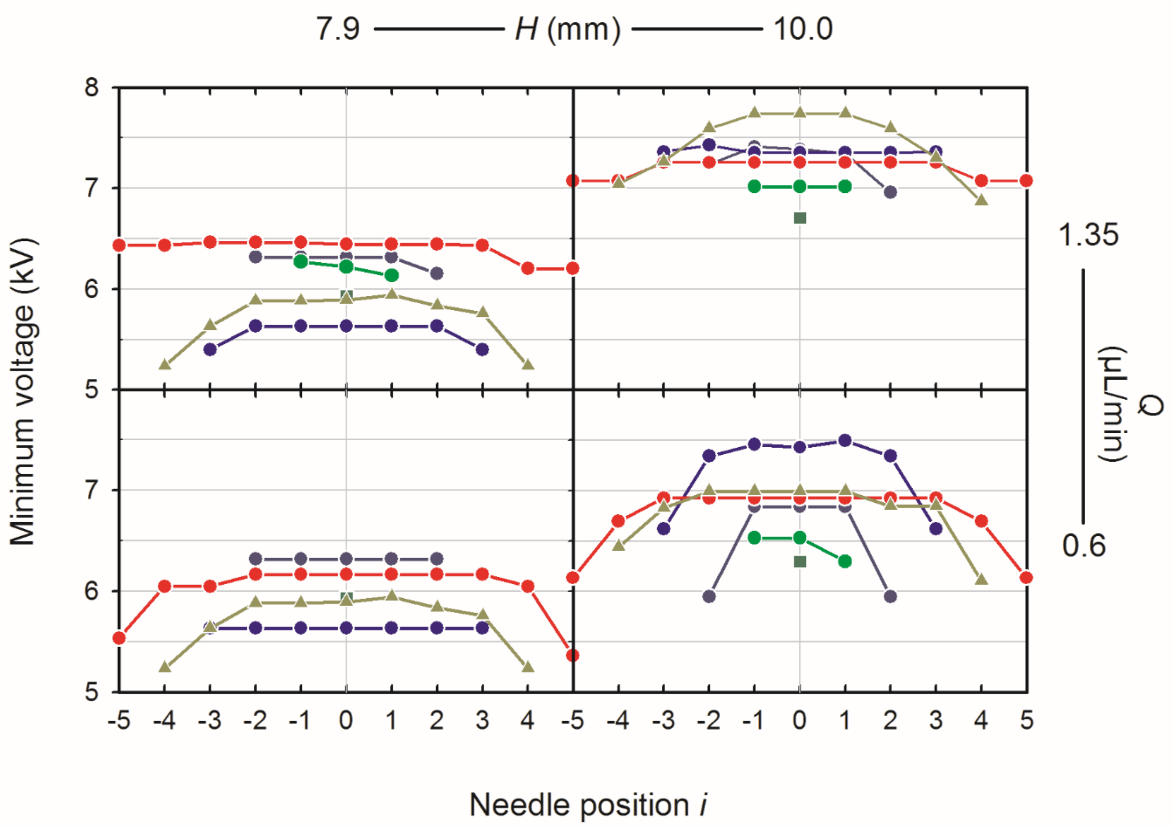

Fig. 2.17. Destabilization sequence from the cone-jet mode for the 11-emitter array, as minus the collector voltage is slowly decreased, for different H and Q values. The graphs show the voltage (minus voltage applied on the collector plate) at which each emitter transitioned from the steady cone-jet mode to the intermittent cone-jet mode (V_{down}) *versus* emitter position i. Liquid= SC250, Cconfiguration C. Q is the flow rate per emitter.

An interesting qualitative observation is that the array can be stabilized at a lower voltage than V_{up}. While the array is operating in the intermittent cone-jet, at a voltage a few hundred volts lower than V_{up} (but larger than V_{down}), a sudden gush of air is directed towards it, strong enough to blow the sprays away from under the emitters. The array recovers itself directly into the steady cone-jet mode (see complementary video data). We believe that the space charge below the emitters was momentarily carried away, causing the local field at the tip of the emitters to reach the required value to enter the stable cone-jet mode stability region. Due to hysteresis, the array remains stable (Smith, 1986; Cloupeau and Prunet-Foch, 1989).

2.6.2 Role of electrical conductivity (K) on the onset voltage (V_{up})

The role of space charge also becomes apparent when changing the electrical conductivity of the liquid, K When K is reduced, the transition voltage V_{up} from intermittent to steady spraying is reduced significantly. This is shown in Fig. 2.18 for the 11-emitter array, which compares data obtained with liquids differing in K by a factor of ~8. The comparison is made at equal flow rate per emitter (Q) and emitter-collector separation (H). In Fig. 2.18b, we observe similar patterns of the emitter transition voltage for the two K values, except for the shift to lower voltages as K is decreased. Fig. 2.19 shows that the plume configurations obtained with these liquids are strikingly different.

We interpret the reduction in V_{up} when K is decreased as caused by differences in the spray space charge. The electric field required to sustain the Taylor cones should be nearly the same for both liquids, as their surface tensions are similar. However, the contribution from the space charge to this electrical field is different depending on K, being lower for the low-K liquid. This is due both to the lower amount of charge, and the fact that it is distributed farther away (Fig. 2.19). Order of magnitude analysis considering charge conservation under steady state shows that the electrical charge contained in a spray is proportional to the electrical current and inversely proportional to the applied voltage and the electrical mobility of the droplets. The reduction in K causes a decrease in electrical current (per emitter) from 149 to 43.7 nA, a factor of about 3.4, which is close to the square root of the electrical conductivity values (2.8), in approximate agreement with scaling laws proposed in the literature (Fernandez de la Mora & Loscertales, 1994; Gañán-Calvo et al., 1997; Rosell-Llompart et al., 2018). The electrical mobility of the droplets can be compared for the two conductivities considering the scaling laws of droplet charge and size, resulting in larger mobility for the low K case. Both of these effects lead to higher space charge for the larger K case, despite the difference in applied voltage.

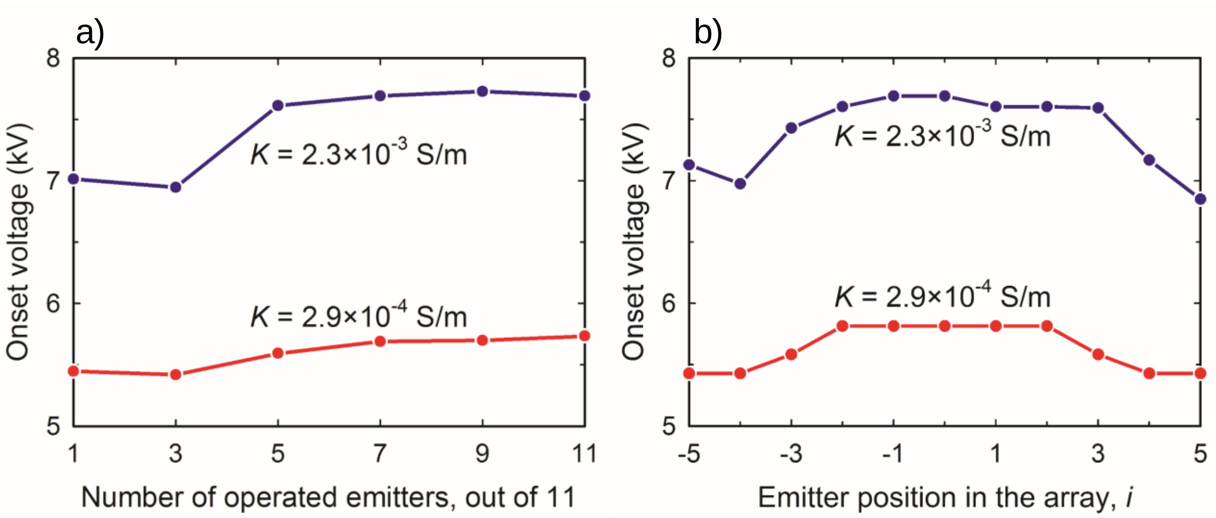

Fig. 2.18. Effect of liquid electrical conductivity for a 11-emitter array, (a) on the transition voltage V_{up} versus number of operated emitters, and (b) V_{up} versus emitter position i in the array. Parameters: Q = 1.35 µl/min (per emitter), H = 10 mm, P = 2.5 mm and end electrode configuration C. Reported conductivities are from Table 2.2. For (b) the current per emitter was approximately uniform along the array, with mean values of 149 nA for the high conductivity liquid (SC250) at 27 ºC, and 43.7 nA for the low conductivity liquid (SC025) at 24.5 ºC.

a. 2.3 × 10^{-3} S/m

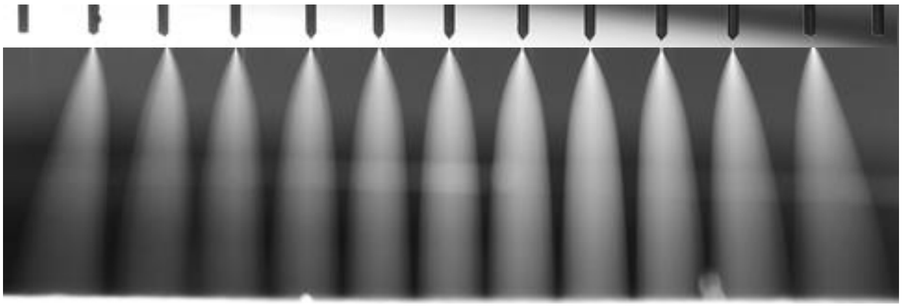

b. 2.9 × 10^{-4} S/m

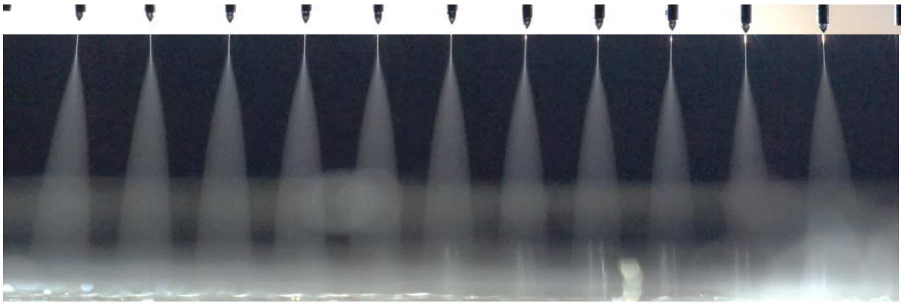

Fig. 2.19. Effect of conductivity on the electrospray plume shapes, for the same flow rate per emitter (1.35 µL/min) and array geometry (configuration C with equal emitter tip to collector distance, H = 10 mm). In a) the solution is SC250, with K= 0.0023 S/m, Vc = -8.39 kV, T = 27 °C, current per emitter I = 149 nA. In b) the solution is SC025, K = 0.00029 S/m, Vc = -5.78 kV, T = 23°C, I = 43.7 nA. Images are composites of brightfield and darkfield images in graytone.

2.7 Conclusions

The scaling up of the electrospray process is not trivial, as it involves operating multiple Taylor cones in a small space in the presence of strong electrostatic fields. The aim of this study is to define the conditions of robust operation for extractor-free linear arrays of electrosprays in simple, and dense geometries. By "simple" we mean geometries in which only two electrodes are used: the spray emitters and a counter electrode. And by "dense" we mean that the separation between the counter electrode and the electrospraying emitters is large compared to the spacing between adjacent emitters (pitch). Our approach excludes the use of so-called extractor electrodes, which can compromise reliability. We include a backplate, which is a conducting plate set behind the emitters and set at their same electric potential (voltage). The two plates define a parallel-capacitor gap that hosts the linear array and sprays, and shields them from external perturbations.

First we have gained physical insights into the question of scalabilility from electric field computations of arrays of lines-of-charge (section 2.3). These computations have revealed that the electric field at the edge of the array does not increase indefinitely as the array grows. Instead, the field converges towards a plateau value as the number of lines increases, and such plateau is approached when the width of the array is as small as the plate's gap (H). We have shown also that image charges in the two plates speed up the convergence of the electric field. We also reach this conclusion for 2D square arrays of lines-of-charge.

Next, we have numerically solved the electric field for linear arrays of emitter tubes protruding from the backplate, in absence of space charge (sprays), to identify if array-end non-spraying electrodes are needed in the array-in-capacitor design. We have found that at the two last positions at the extremes the electric field is significantly stronger and azimuthally less uniform than at the other positions. Therefore, we have identified as optimal array configurations the ones having on either end two non-spraying electrodes, positioned at the same pitch as the spraying emitters. We have implemented experimentally several configurations. Our most robust one has a passive (non-spraying) emitter in the innermost position and a much thicker electrode in the outermost position to prevent the appearance of gas discharges at that location. We have estimated the difference in electric field strength at the Taylor cones between the central and edge spraying emitters of only a few % (section 2.3.1).

By acquiring the individual time traces of the electrical current transmitted through each emitter separately, we have established two voltages when the spraying mode changes at each location on the array: The *onset voltage*, reached when the steady cone-jet mode is established as the applied voltage difference is increased while in the intermittent mode, and the *minimum voltage*, the voltage when the steady cone-jet stops after the voltage difference is lowered. We have found that near the onset voltage the sprays are straight and are similarly shaped for the central locations of the array, whereas the sprays progressively expand near the edge of the array (section 2.5.1). In another experiment (section 2.6.1), we have studied the onset voltage progression as the number of operated emitters is increased in a fixed array from 1 to 11, by turning on only the central emitter, and progressively adding adjacent emitters. We have found that the onset voltage depends on the number of operated emitters, because the spray space charge reduces the electric field in the Taylor cone region. However, the onset voltage reaches a plateau for the innermost emitters. Its value increases when the electrical conductivity is increased, as expected from the increase in space charge (section 2.6.2). We conclude from these experiments that the electrostatic field experienced by the central region of very long arrays is not dependent of how large the array is. So, the array is expandable indefinitely while the voltage is bounded, averting gas breakdown discharges. We have shown this for arrays characterized by a small pitch of 2.5 mm (4 emitters/cm) and a collector distance as large as 13 mm.

We have also reported on "symmetry breaking" of the electrosprays, observed at high enough voltage, caused by the tilting of the Taylor cones (section 2.5.2). Tilting of a Taylor cone is a familiar phenomenon in conventional electrospraying from single emitters without extractor. Here, we have used stereoscopic imaging to identify the directions at which the microjets are pointing. We have found that those directions correlate with the slight emitters' misalignments when they have a zig-zag pattern, with the jets roughly pointing in the direction of strongest field strength. In absence of a pattern, other factors are important in this phenomenon, as, sometimes, the array end sprays point inward toward the array, instead of outward where the field is most intense. These experiments suggest that symmetry breaking may be exploited to actively control the collection of the generated droplets/particles.

2.8 Acknowledgements

I want to thank Prof. Jordi Grifoll for providing the electric field computations and further participation in the discussion of the results, without the help of whom this work would prove much more challenging. I also thank Jordi Mare for the printing of the nano-ameter circuit boards. This work has been supported by the Spanish Government under grants DPI2015-68969-P (MINECO/FEDER), and the Catalan Government under grant 2017SGR1516, and by Universitat Rovira i Virgili (URV) through grant 2015PFRURV-B2-57. Nikolas Sochorakis also acknowledges scholarships from the URV and from the Spanish Government (BES-2013-064098).

2.9 References

Almekinders, J.C., Jones, C., (1999). Multiple jet electrohydrodynamic spraying and applications. J. Aerosol Sci. 30, 969–971. https://doi.org/10.1016/S0021-8502(98)00755-1

Almería, B., Deng, W., Fahmy, T.M., Gomez, A., (2010). Controlling the morphology of electrospray-generated PLGA microparticles for drug delivery. J. Colloid Interface Sci. 343, 125–133. https://doi.org/10.1016/j.jcis.2009.10.002

Almería, B., Fahmy, T.M., Gomez, A., (2011). A multiplexed electrospray process for single-step synthesis of stabilized polymer particles for drug delivery. J. Control. Release 154, 203–210. https://doi.org/10.1016/j.jconrel.2011.05.018

Bhatnagar, P., (2007). Multiplexed electrospray deposition for protein microarray with micromachined silicon device. Appl. Phys. Lett. 91, 14102. https://doi.org/10.1063/1.2754642

Bober, D.B., Chen, C.-H., (2011). Pulsating electrohydrodynamic cone-jets: from choked jet to oscillating cone. J. Fluid Mech. 689, 552–563. https://doi.org/10.1017/jfm.2011.453

Bocanegra, R., Galán, D., Márquez, M., Loscertales, I.G., Barrero, A., (2005). Multiple electrosprays emitted from an array of holes, J. Aerosol Sci. 36, 1387–1399. https://doi.org/10.1016/j.jaerosci.2005.04.003

Cloupeau, M., Prunet-Foch, B., (1989). Electrostatic spraying of liquids in cone-jet mode. J. Electrostat. 22, 135–159. https://doi.org/10.1016/0304-3886(89)90081-8

Deng, W., Gomez, A., (2011). Electrospray cooling for microelectronics. Int. J. Heat Mass Transf. 54, 2270–2275. https://doi.org/10.1016/j.ijheatmasstransfer.2011.02.038

Deng, W., Gomez, A., (2007). Influence of space charge on the scale-up of multiplexed electrosprays. J. Aerosol Sci. 38, 1062–1078. https://doi.org/10.1016/j.jaerosci.2007.08.005

Deng, W., Klemic, J.F., Li, X., Reed, M.A., Gomez, A., (2006). Increase of electrospray throughput using multiplexed microfabricated sources for the scalable generation of monodisperse droplets. J. Aerosol Sci. 37, 696–714. https://doi.org/10.1016/j.jaerosci.2005.05.011

Deng, W., Klemic, J.F., Li, X., Reed, M.A., Gomez, A., (2007). Liquid fuel microcombustor using microfabricated multiplexed electrospray sources. Proc. Combust. Inst. 31, 2239–2246. https://doi.org/10.1016/j.proci.2006.08.080

Deng, W., Waits, C.M., Morgan, B., Gomez, A., (2009). Compact multiplexing of monodisperse electrosprays. J. Aerosol Sci. 40, 907–918. https://doi.org/10.1016/j.jaerosci.2009.07.002

Fenn, J.B., (2003). Electrospray wings for molecular elephants (Nobel lecture). Angew. Chemie Int. Ed. 42, 3871–3894. https://doi.org/10.1002/anie.200300605

Fernández de la Mora, J., (1992). The effect of charge emission from electrified liquid cones. J. Fluid Mech. 243, 561–574. https://doi.org/10.1017/S0022112092002829

Gañán-Calvo, A.M., Dávila, J., and Barrero, A. (1997). Current and droplet size in the electrospraying of liquids. Scaling laws. J. Aerosol Sci., 28(2):249–275.Grifoll J., (2018), personal communication.

Higuera, F.J., (2013). Multifluid Eulerian model of an electrospray in a host gas. J. Fluid Mech. 734, 363–386. https://doi.org/10.1017/jfm.2013.450

Hogrefe, O., Drewnick, F., Lala, G.G., Schwab, J.J., Demerjian, K.L., (2004). Development, operation and applications of an aerosol generation, calibration and research facility. Aerosol Sci. Technol. 38, 196–214. https://doi.org/10.1080/02786820390229516

Hubacz, Marijnisen, (2003). The scale-up of electrohydrodynamic atomization, in: J Aer. Sci. - Proc. European Aerosol Conference. pp. S1269–S1270. https://doi.org/10.1016/S0021-8502(03)00171-X

Jackson, J.D., (1998). Classical Electrodynamics, 3rd ed. John Wiley & Sons.

Jaworek, A., Lackowski, M., Krupa, A., Czech, T., (2006). Electrostatic interaction of free EHD jets. Exp. Fluids 40, 568–576. https://doi.org/10.1007/s00348-005-0096-3

Kawakami, K., (2012). Miscibility analysis of particulate solid dispersions prepared by electrospray deposition. Int. J. Pharm. 433, 71–78. https://doi.org/10.1016/j.ijpharm.2012.04.082

Kelly, R.T., Page, J.S., Tang, K., Smith, R.D., (2007). Array of chemically etched fused silica emitters for improving the sensitivity and quantification of electrospray ionization mass spectrometry. Anal. Chem. 79, 4192–4198. https://doi.org/10.1021/ac062417e

Kelly, R.T., Page, J.S., Zhao, R., Qian, W.J., Mottaz, H.M., Tang, K., Smith, R.D., (2008a). Capillary-based multi nanoelectrospray emitters: Improvements in ion transmission efficiency and implementation with capillary reversed-phase LC-ESI-MS. Anal. Chem. 80, 143–149. https://doi.org/10.1021/ac701647s

Kelly, R.T., Page, J.S., Marginean, I., Tang, K., Smith, R.D., (2008b). Nanoelectrospray emitter arrays providing interemitter electric field uniformity. Anal. Chem. 80, 5660–5665. https://doi.org/10.1021/ac800508q

Kempen, L., Hartmer, R., Brekenfeld, A., Holle, A., Lang, W., (2016). A multi-nozzle electrospray emitter for pneumatically assisted electrospray in LC-MS analysis. Procedia Eng. 168, 1366–1369. https://doi.org/10.1016/j.proeng.2016.11.378

Kim, W., Guo, M., Yang, P., Wang, D., (2007). Microfabricated monolithic multinozzle emitters for nanoelectrospray mass spectrometry. Anal. Chem. 79, 3703–3707. https://doi.org/10.1021/ac070010j

Kim, H., Kim, S.S., (2014). Development and characterization of saw-tooth-type slit nozzle for electrospray. Aerosol Sci. Technol. 49, 11–15. https://doi.org/10.1080/02786826.2014.989956

Krpoun, R., Shea, H.R., (2009). Integrated out-of-plane nanoelectrospray thruster arrays for spacecraft propulsion. J. Micromechanics Microengineering 19, 045019.

Krpoun, R., Shea, H.R., (2009). Integrated out-of-plane nanoelectrospray thruster arrays for spacecraft propulsion. J. Micromechanics Microengineering 19, 045019. https://doi.org/10.1088/0960-1317/19/4/045019

Kumar, V., Srivastava, A., Shanbhogue, K.M., Ingersol, S., Sen, A.K., (2018). Electrospray performance of interacting multi-capillary emitters in a linear array. J. Micromechanics Microengineering 28, 35005 (10pp). https://doi.org/10.1088/1361-6439/aaa1d5

Kyritsis, D.C., Coriton, B., Faure, F., Roychoudhury, S., Gomez, A., (2004). Optimization of a catalytic combustor using electrosprayed liquid hydrocarbons for mesoscale power generation. Combust. Flame 139, 77–89. https://doi.org/10.1016/j.combustflame.2004.06.010

Lhernould, M.S., Lambert, P., (2011). Compact polymer multi-nozzles electrospray device with integrated microfluidic feeding system. J. Electrostat. 69, 313–319. https://doi.org/10.1016/j.elstat.2011.04.006

Lojewski, B., Yang, W., Duan, H., Xu, C., Deng, W., (2013). Design, fabrication, and characterization of linear multiplexed electrospray atomizers micro-machined from metal and polymers. Aerosol Sci. Technol. 47, 146–152. https://doi.org/10.1080/02786826.2012.734936

Mao, P., Wang, H.-T., Yang, P., Wang, D., (2011). Multinozzle emitter arrays for nanoelectrospray mass spectrometry. Anal. Chem. 83, 6082–6089. https://doi.org/10.1021/ac2011813

Quang Tran, S.B., Byun, D., Nguyen, V.D., Yudistira, H.T., Yu, M.J., Lee, K.H., Kim, J.U., (2010). Polymer-based electrospray device with multiple nozzles to minimize end effect phenomenon. J. Electrostat. 68, 138–144. https://doi.org/10.1016/j.elstat.2009.11.011

Rosell-Llompart, J., Grifoll, J., Loscertales, I.G., (2018). Electrosprays in the cone-jet mode: From Taylor cone formation to spray development. J. Aerosol Sci. In press. https://doi.org/10.1016/j.jaerosci.20

Rulison, A.J., Flagan, R.C., (1993). Scale-up of electrospray atomization using linear arrays of Taylor cones. Rev. Sci. Instrum. 64, 683–686. https://doi.org/10.1063/1.1144197

Sandengen, K., Kaasa, B., (2006). Estimation of monoethylene glycol (MEG) content in water + MEG + NaCl + NaHCO3 solutions. J. Chem. Eng. Data 51, 443–447. https://doi.org/10.1021/je0503711

Smith, D.P.H., (1986). The electrohydrodynamic atomization of liquids. IEEE Trans. Ind. Appl. IA-22, 527–535. https://doi.org/10.1109/TIA.1986.4504754

Steiner, G., Franchin, A., Kangasluoma, J., Kerminen, V.M., Kulmala, M., Petäjä, T., (2017). Production of neutral molecular clusters by controlled neutralization of mobility standards. Aerosol Sci. Technol. 51, 946–955. https://doi.org/10.1080/02786826.2017.1328103

Tang, J., Gomez, A., (2015). Control of the mesoporous structure of dye-sensitized solar cells with electrospray deposition. J. Mater. Chem. A 3, 7830–7839. https://doi.org/10.1039/C5TA00288E

Velásquez-García, L.F., Akinwande, A.I., Martínez-Sánchez, M., (2006). A micro-fabricated linear array of electrospray emitters for thruster applications. J. Microelectromechanical Syst. 15, 1260–1271. https://doi.org/10.1109/JMEMS.2006.879707

Wang, D., Zhu, X., Liang, J., Ren, T., Zha, W., Dong, W., Rocks, S.A., Dorey, R.A., Xu, Z., Wang, X., (2015). Electrohydrodynamic jet printing of PZT thick film micro-scale structures. J. Eur. Ceram. Soc. 35, 3475–3483. https://doi.org/10.1016/j.jeurceramsoc.2015.05.013

Wang, L., Stevens, R., Malik, A., Rockett, P., Paine, M., Adkin, P., Martyn, S., Smith, K., Stark, J., Dobson, P., (2007). High-aspect-ratio silica nozzle fabrication for nano-emitter electrospray applications. Microelectron. Eng. 84, 1190–1193. https://doi.org/10.1016/j.mee.2007.01.116

Xie, J., Jiang, J., Davoodi, P., Srinivasan, M.P., Wang, C.H., (2015). Electrohydrodynamic atomization: A two-decade effort to produce and process micro-/nanoparticulate materials. Chem. Eng. Sci. 125, 32–57. https://doi.org/10.1016/j.ces.2014.08.061

Yang, W., Lojewski, B., Wei, Y., Deng, W., (2012). Interactions and deposition patterns of multiplexed electrosprays. J. Aerosol Sci. 46, 20–33. https://doi.org/10.1016/j.jaerosci.2011.11.004

Zhao, X.-Y., Li, C., Yang, W., Deng, W., (2017). Paper-based electrospray emitters. J. Aerosol Sci. 113, 108–113. https://doi.org/10.1016/j.jaerosci.2017.07.013

Zhou, F.L., Gong, R.H., Porat, I., (2009). Mass production of nanofibre assemblies by electrostatic spinning. Polym. Int. 58, 331–342. https://doi.org/10.1002/pi.2521

Chapter 3

Use of linearly multiplexed electrosprays to produce PVP-curcumin submicron particles, collected on paper and Si substrates.

Abstract

A Linear Electrospray System (LEsS) was implemented for the production of polymer micro/nano particles loaded with an active pharmaceutical substance (API). Below each emitter the particles accumulated over time, produce 2D-ovoidal deposition spots due to the electrostatic interaction between the spray-plumes of neighboring emitters. The spots diverge from the array axis reflecting the misalignment of the emitters within the linear array. An horizontal electrode configuration implemented to restored the symmetry of the deposition spots potentially facilitating the collection of the produced particles. Apart from a silicon wafer that was used, to collect particles we demonstrate for the first time that it is possible to collect particles directly on paper, at ambient conditions. Paper can be used to facilitate collection of electrospray particles on roll-to-roll process and can present interest for other applications. Position sensitive analysis at areas of interest (AOI) in each spot was performed using Scanning Electron Microscopy (SEM) to identify the distribution of sizes and morphology of the deposited micro-particles. Finally, the API used throughout this study was turmeric, a potent anti-inflammatory natural substance that is non-water soluble and therefore has low bio-availability. We propose a formulation of a highly hydrophilic polymer (PVP) to formulate below 1-micron particles, for improved solubility and subsequently bioavailability of our API.

Keywords: Electrospray multiplexing, Curcumin nanoparticles, bioavailability, water solubility, pharmaceutical carriers, paper, electrospray deflection

3.1 Introduction

A key feature of micro processed materials is the high surface to mass ratio (Rajiv Saini et al. ,2010). Electrospray provides a very efficient way of converting electrical energy into surface energy, electrostatically inducing break-up of liquids into droplets. Furthermore, the size of the produced droplets, is accurately dictated by the supplied liquid flow rate (Rosell-Llompart et al., 2018). This allows precise control over droplet size, but comes out as a shortcoming of electrospray systems when high throughput is required. Maintaining the required flow rate while increasing the throughput is resolved by the multiplexing of the electrospray emitters.

Highly charged liquid droplets have direct uses, namely, mass spectrometry (Fenn,1989), satellite propulsion (Demmons,2016) bioprinting (Eagles et al., 2006), cooling systems

(Deng et al., 2011), environmental forensics (Rostad et al., 2007), wind energy harvesting (Djairam et al. 2014), sanitization (Pyrgiotakis et al., 2016, Jaworek et al., 2006) etc.

On the other hand, polymeric liquid solutions in combination with electrospray droplet drying, is a straightforward method to create micro/nano particles (Hwang et al., 2012, Bodnár et al., 2018) of very narrow size distributions, or continuous film coatings. Moreover, an Active Pharmaceutical Ingredient (API) can be combined with polymeric solutions, upgrading electrospray drying into a powerful technique for micro/nano-sized pharmaceutical carrier formulations (Mehta et al., (2017). Even polymer/API systems with no common solvents can be made into encapsulations using coaxial electrospray emitters, where layered shell - core particles are formed (Loscertales et al. 2002, Lee et al. 2011). Tailored sized particles can penetrate selectively the body physiological barriers from the epidermis down to the cellular membrane, for targeted drug delivery (Chauhan et al., 2012).

The oral administration route is one of the most convenient to use as it is not intrusive for the patient. In this case not only the size of the particle formulations but also the aqueous solubility of the API/polymer formulations affecting API bioavailability (Williams et al., 2013). The aim is to minimize the administered API dosage, reducing side-effects and increase residence time in systemic blood circulation. More than 50% percent of the newly developed APIs are BCS class II compounds, meaning they suffer from low water solubility. This led to intense research in the field with huge interest to the pharmaceutical and chemical industry (Ting et al., 2018). Out of several strategies (Williams et al., 2013) for improving water solubility electrospray (Es) can be directly applied for API nano/micronization, simultaneously with the solid dispersion method where, the hydrophobic API is conjugated to a water-soluble polymer (Zelikin A.,2018). Other more elaborate strategies that may also be applied through Es for the same purpose is particle shape engineering Zhao et al., 2017, Bodnár et al., 2018), crystal engineering (isomer) (Patil et al., 2017, Rietveld et al., 2010) and quite possibly charge assisted surface functionality modification as has been demonstrated for electrospun fibers (Stachewicz et al., 2012).

Curcumin was chosen as our model API due to its great promise as a drug (Bharat et al., 2007, Jurenka et al., 2009, Mouthuy et al., 2017, Wang et al., 2015, Cartiera et al., 2010), its aqueous insolubility and its general handling safety, classified as GRAS- (Generally Recognized As Safe by the FDA (Gad et al.,2014).

Here we propose a linearly multiplexed system (LEsS) previously developed and studied by our research group (Sochorakis, N., et al, 2018) for the scaled-up production of polymeric particles through droplet drying. These particles are loaded with a potent API (curcumin) that suffers however from low water solubility. The proposed formulation of a water-soluble polymer combination with the micron sized of produced particles, is a single step process to increase water solubility and therefore Curcumin bioavailability. The process can be easily adapted to other API formulations and the whole system is up scalable without bound (see chapter 2). We propose, for the specific system, a novel design horizontal electrode, parallel to the array axis, that creates a uniform deposition pattern on the collector surface. A paper (non-conducting) fibrous collector, never proposed before, to our knowledge, for electrospray systems has been used as an alternative collection surface. Paper is a trending material promoted for applications such as printed sensors, microfluidics, flexible electrodes etc. (Lan et al., 2013, Carrilho et al., 2009) due to its low price and popularity. Other non-conducting, absorbent flexible materials (fabrics,garments etc) may be also eligible for Es, opening new perspectives in the field.

3.2 Materials and methods

Polyvinylpyrrolidone (PVP), (CAS Number 9003-39-8, average Molecular weight (Mw) 40kDa, ethyl cellulose (EC), (4 cP viscosity, 48% ethoxyl content, density 1.14 g/ml), butanone (Sigma–Aldrich, ACS reagent grade),rhodamine 6G (Rh6G, Sigma–Aldrich) ethanol (laboratory reagent 96%, CAS Number 64-17-5), acetic acid glacial (CAS Number: 64-19-7) and curcumin/Turmeric powder (CAS Number 458-37-7, Mw 368.38 gr/mol) were purchased from Sigma-Aldrich and used with no further purification. The solutions prepared for the experiments are shown in

Table 3.1.

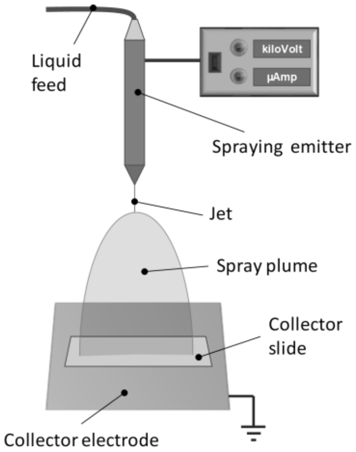

Figure 3.1: This is a schematic of a single emitter Es setup that has been used for trial solution testing.

A single emitter Es setup was deemed necessary to screen trial solutions, before porting to the Linear Electrospray System (LEsS). For example, distance from tip to collector (H), solution composition and flow rate (Q) are core parameters which control droplet drying, for the production of particles, that can quickly be screened prior to LEsS testing. Additionally, during the same tests, we get an estimation of the voltage range within which, for each set of screening parameters, the single Es operates in the stable Taylor cone-jet mode. Figure 3.1 shows the emitter is of the same dimensions as the ones used in the multiplexed system. The “collector slide” is the material inserted for a limited amount of time to collect the generated particles. The “spraying emitter” is connected directly to the positive channel of a high voltage power supply and the “collector electrode” grounded. The liquid is supplied by a syringe pump (KDS legacy 100) with dial-in flow rate input panel. A positive voltage is applied at the emitter producing positive Es.

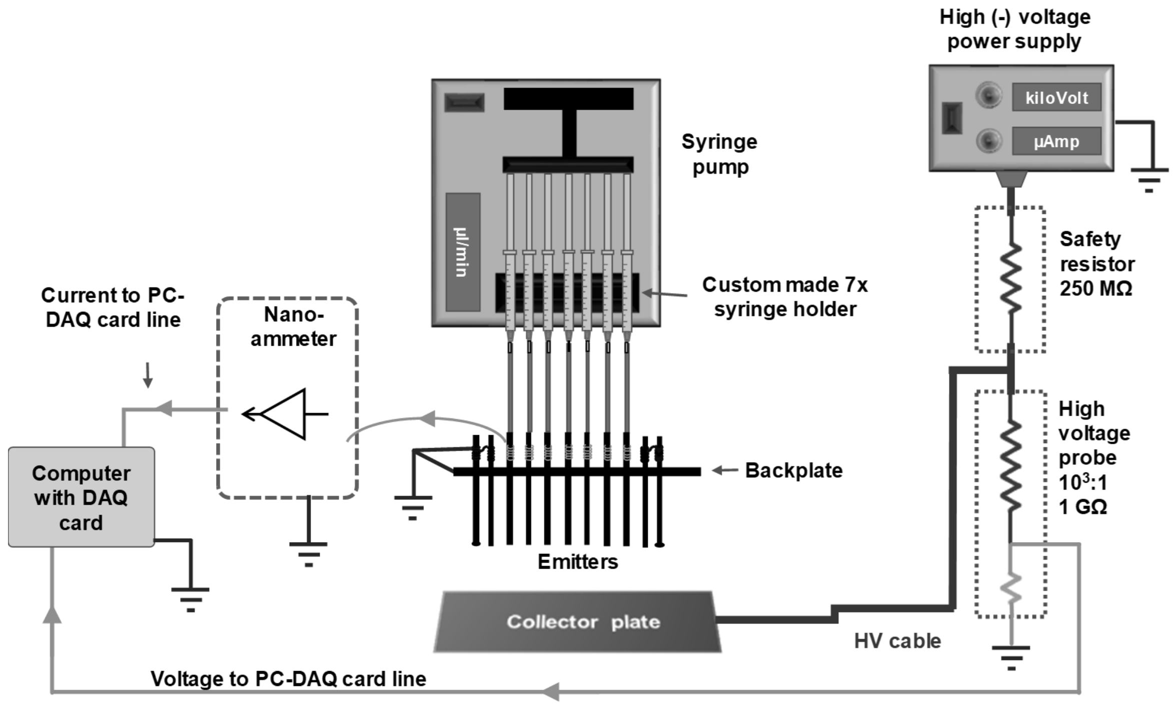

Figure 3.2: LEsS01 schematic. The material where the particles are collected is inserted between the collector and the emitters always in contact with the collector plate.

The electrospray emitters are 100 mm long sections of 304 stainless-steel capillary tubing (Tubos Capilares, Spain; O.D. 400 µm, I.D. 160 µm) flat-cut and polished on their exit end. They protrude out of the backplate, which is a perforated metal plate held parallel to the collector plate. The support structure rests on the collector plate with four Delrin© legs which sit on insulating spacers used for controlling height (not shown). Initially a rectangular brass plate was used as collector. The collector plate and backplate are sized 85 x 235 mm, defining a parallel-capacitor in which the emitters and the electrosprays are shielded from external electrical conditions and perturbations. The emitters are sandwiched in a sub-assembly consisting of two Delrin© mirror blocks with precut groves, press fit together by two screws (not shown). Additional electrodes are placed at the ends of the array, as described later. For the 11 emitters at 2.5 mm pitch, the standard deviation for the emitter separations (along the array or x-axis) is only 0.09 mm, and that for the cross-array (y-axis) displacements from a perfect line is only 0.06 mm.

The electric field necessary for electrospraying is provided by a negative high voltage (HV) power supply connected (Ultravolt, HV-RACK-4-250-0032, 0 to -15 kV range) to the collector through a high voltage-rated 250 MΩ safety-resistor. We continuously monitor the applied electric potential at the collector V_c by means of a HV probe (Testec, TT-HVP-40, 109 Ω), as shown in Fig. 3.2.

The emitters and the backplate are earth-grounded, either through a nanoammeters(s) of homemade design housed in a shielded box, or directly on the return of the power supply. The output voltages from the nanoammeters(s) and the high voltage probe are fed to a National instruments PCI 6221 DAQ card on a desktop computer. A negative high voltage is applied on the collector plate in order to obtain a positive electrospray, as in the single emitter setup (Fig. 3.1). The schematic of the 7-emitter setup is shown in Fig. 3.2. This was the setup we used initially where the syringe pump (Harvard apparatus phd 2000) was modified to accommodate up to 7-syringes. In the experimental part presented later all the 7-spot polymer particle depositions (composed of EC-rhodamine) were generated using this setup. The current was globally recorded for all the emitters through a single nanoameter. Later-on to increase the number of emitters and get rid of the syringe pump minute fluctuations we re-designed the liquid feed system as well as multiplexed the current monitoring system, but kept the rest of the setup essentially intact.

The individual nanoammeters -1 per emitter- allow us to distinguish between spray modes at each sprayer, record and diagnose system stability. Additionally, the pressure driven liquid feeding system, gives us the advantage of low cost scalability and is described in chapter 2 materials and methods (section 2.2). The later was used for all the experiments related to PVP-curcumin polymer particle formulations. We used two methods to calculate the volumetric flow rate for our experiments. The first method is based on a direct calibration curve of gas pressure vs volumetric flow rate. Another method for estimating the volumetric flow rate for each experiment was grabbing images of the pendent drops formed at the tip of the emitters with time tags and then using the ImageJ "Pendent drop" plugin (Daerr & Mogne, 2016) to estimate the droplet volume/unit time for each experiment. The necessary information can be extracted by the sample image of a growing drop, shown in Fig. 3.3.

Figure 3.3: Time evolution sample stack of pictures of the pendent drop (10 sec intervals), that was used to estimate the volume and subsequently the volumetric flow rate using ImageJ software.

The current traces are indicative of the Es mode (dripping, intermittent jet, stable jet). In addition, the current is a monotonous function of flow rate. Therefore, differences in current can be used to detect differences on the hydrodynamic resistance of the supply lines, or occasional changes caused by partial clogging.

Es protocol

Electrospraying was carried in laboratory air, whose temperature (T) and relative humidity (between 25% and 40% for all the experiments) was determined with a Vaisala HM34 meter. A typical experimental run starts with setting the gas pressure to achieve the desired flow rate. Sometime (minutes) is required for the pressure to stabilize and for the liquid to fill the lines. Once the flow rate is steady, the data acquisition is initiated, and the applied voltage is ramped-up manually and pictures are shot frequently. The main spraying modes which we differentiate in the experiments described are the intermittent cone-jet and the steady cone-jet modes (Rosell-Llompart et al., 2018). The former one, also known as pulsating mode (Smith, 1986; Bober & Chen, 2011), is characterized by a lower current level, and is encountered before the steady mode, as voltage is increased.

For the collection of particles, a slide (weighed before and after the deposition) was swiftly (< 1 sec) positioned under the Es emitters always in contact with the collector electrode using glass insulating rods. The collection time was monitored with a hand chronometer. A camera with a macro lens, and in some cases current measurements, ensured that for the whole duration the sprayers were operating. After the collections the slides were swiftly retracted over the same path as the slide insertion. The samples collected were photographed under the same lighting conditions and then transported to the SEM where they were sputtered with a gold layer from the operating at 30mA for 180 sec (~40nm) and the samples were analyzed in the SEM to confirm the particle formation and obtain info about size distribution, shape, morphologies etc.

For some of the experiments a cylindrical copper wire with a diameter of 1.1 mm, termed as the “horizontal electrode” was attached to the backplate. The horizontal electrode was at the same height as the emitter tips, parallel to and at 2,5 mm distance from the emitter axis.

Two different types of collector slides were used Si wafer (Siltronix, 0.525 mm thickness, 1-30 ohm resistivity, P-Bor 100) and cellulose filter paper (0.16 mm thickness, 0.0085 gr/cm^2).

Imaging of sprays and cones

The spraying modes could be identified by following the current traces as well as the liquid meniscus shape at the exit of each emitter tube. The meniscus is imaged best under brightfield conditions, for which a LED backlight was positioned behind the emitter array, and the array was imaged from the opposite side (front view). In this case, image contrast arises from attenuation of light by the cones, while attenuation by the sprays is small. To image the spray plumes darkfield illumination was used, whereby image contrast arises from light scattered (rather than attenuated) by the droplets. In this case, the backlight was replaced by a black velvet cloth, which provided a dark background, while the sprays were illuminated from two white LED spot lamps positioned symmetrically at roughly 45º from the array mid plane. Additional views of the sprays were taken at an angle using a second camera, to give a perspective of the directions of the micro-jets. Front view images were shot with an OLYMPUS PEN E-PL7 photo camera with a Nikkor macro lens (60 mm, 1:2.8). Side images were taken with an OLYMPUS PEN EP-1 photo camera and a ZUIKO 14-42 mm zoom lens. Most of the images we show later are enhanced for brightness and contrast, while some are presented with their tone scale inverted ("negative images") to better show the spray outline. For evaluating the linear alignment of the emitters in the LEsS a bottomview of the emitters was captured using a mirror and the OLYMPUS PEN EP-1 photo camera and a ZUIKO 14-42 mm zoom lens as shown in Fig. 3.4.

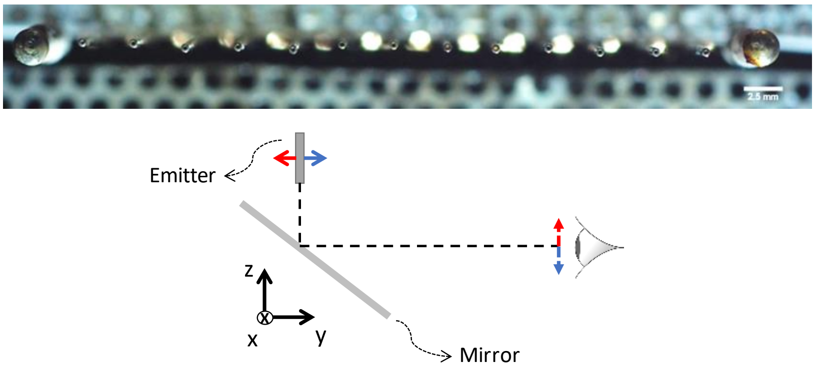

Figure 3.4: The mirror method used to acquire images of the emitter tip positions without disturbing the emitter holder.

Table 3.1

Liquid solutions used in this work

Solution batch code	Solvent 1	w/w (%)	solvent 2	w/w (%)	Solute 1	w/w (%)	solute 2	w/w (%)	conductivity (μS/m)
BREC	Butanone	98.99	NA	0	EC	1	Rhodamine	4.21×10^{-4}	NA
EP	Ethanol 96%	67.13	Acetic acid	22.1	PVP	10.4	NA	0	NA
EPCuPA1	Ethanol 96%	49.97	Acetic acid	46.06	PVP	2	Curcumin	2	NA
EPCuPA2	Ethanol pure	82.45	Acetic acid	14.21	PVP	3.25	Curcumin	0.085	15

*NA = not available

3.3 Results and discussion

3.3.1 Single emitter

The Es deposition spot (Fig.3.5) is shown to highlight the symmetric circular shape of the deposition that is typical for a single emitter setup operating in the stable cone-jet mode. The liquid jet emanating from the Taylor cone tip breaks-up into highly charged droplets. These droplets follow electrophoretic trajectories (axisymmetric) towards the collector electrode. During flight the droplets shrink as solvent evaporates and polymer residues are collected at the collector surface. The deposition spot is populated by the polymer residues and approximately visualizes the electrostatic field lines shape, penetrating the collector surface. Notice the visible halo on the periphery of the spot. This halo is in accordance to the deposition thickness profile discussed in Bodnar et al., 2013 as well as Rodriguez-Perez et al., 2007 and mostly holds the satellite droplets generated during jet-breakup.

Figure 3.5: A single needle deposition spot top-view, when no other emitters are operated at close proximity. Q=2μl/min, RH=40.1 percent, T=20.4 C, H=22 mm, solution BREC. Single emitter setup, applied voltage= 6.1 kV.

Observation 1: In Fig. 3.6 the effect of the adjacent emitters, which only act as electrodes, is apparent by the deformed shape of the deposition spots. The deformations occur in the direction of the array axis, as expected, with the adjacent emitters affecting the axial - symmetricity of the electric field around the operating emitter.

The paper deposition shape and overall appearance, is unexpected, as paper is a non-conducting material that should accumulate charge and quickly deflect the droplets and destabilize the cone-jet (see supplementary video DFLCT of Es deflection over a Kapton insulating slide). At best we would expect a spot with many wet patches. However, the produced spot shapes are very similar to one another with the deposition on paper covering 12% more area for the same depositing time.

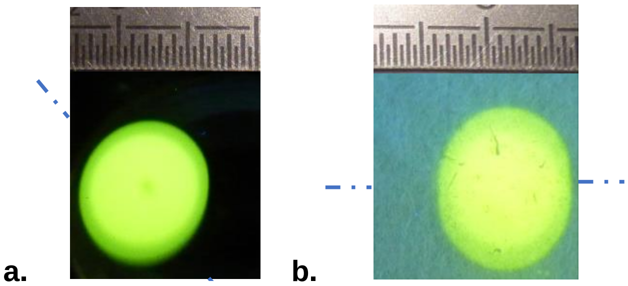

Figure 3.6: LEsS configuration central emitter deposition, spot top-view, when adjacent emitters only act as electrodes. For (a) the collector slide is Si wafer (applied voltage=9.7 kV) and for (b) the collector slide is paper (applied voltage=9.9 kV). The duration of the depositions was the same for both samples. The intermittent line represents LEsS axis direction. LEsS pitch P=2.5mm Q=7 μl/min, RH=28.1 percent, T=20.1 C, H=23 mm, solution=ECuPA.

All the experiments mentioned for paper were realized at ambient conditions of > 28% air Relative Humidity (RH). Water vapor absorption on the paper, may have permitted for sufficient charge drainage, to sustain the Es. Considering the paper a “bad” conductor would also explain the increase in area that depends on the charge dissipation mechanism (Bodnár et al., 2013).

A simple experiment was conducted, where a square (1 cm^2) piece of paper was heated to 100 °C Celsius and then moved to a precision scale and weighted over time in the laboratory environment. The paper increased ~2x in weight after 5 minutes. The same experiment was conducted after reheating to 100 degrees Celsius, measuring the conductivity along the diagonal line of the square paper which also increased ~2x after 5 minutes of exposure in laboratory air (RH=45%, T=24.3°C). Even though the discharge mechanism is still under research we demonstrate here forth, experimentally that common filter paper succeeds as an Es collector. This is an important finding as cellulose based platforms (paper) are intensively studied among many others, for applications in biosensors, antibacterial surfaces etc (Münch et al., 2018).

3.3.2: LEsS emitter setup

Electrostatic interactions are of outmost importance in a multiplexed Es system as not only adjacent emitters but spray plumes as well interact with each other. In our LEsS system the inter-emitter distance, namely the pitch (P) is a critical parameter as all the emitters lie in a single line.

In both ends of the LEsS emitter line we used passive end-electrodes of different shapes and protrusions to control the cone tilting at the array ends aka “end effect” (chapter 2). The configurations used in this work are shown in Fig. 3.7.

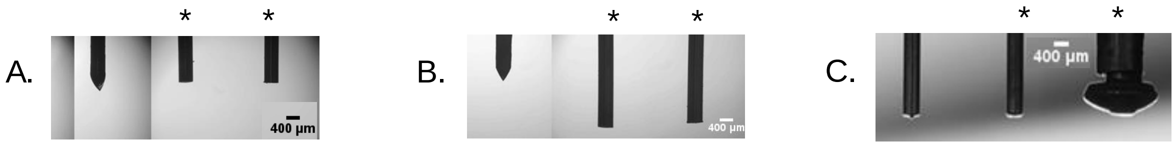

Figure 3.7. Configurations of array-end electrodes used in this study. Such electrodes are marked with a *, while the spraying needles show Taylor cones. The end electrode configuration is symmetric for both ends of the LEsS (right side shown). Emitter diameter (D) is 400 µm.

Pitch **4.3mm** **2.5 mm**

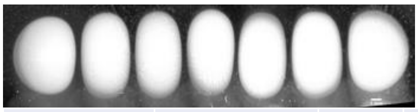

Depostion duration	30 sec
Deposition length	38.31 mm
Flow rate	1.5 μl/min
Applied Voltage	-5.9 kV
Configuration	no end electrodes
Deposition length/over sprayer array length	1.33

Depostion duration	30 sec
Deposition length	25 mm
Flow rate	1.5 μl/min
Applied Voltage	-7.35 kV
Configuration	no end electrodes
Deposition length/over sprayer array length	1.82

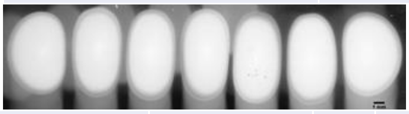

Depostion duration	30 sec
Deposition length	36.01 mm
Flow rate	1.5 μl/min
Applied Voltage	-6.4 kV
Configuration	A
Deposition length/over sprayer array length	1.25

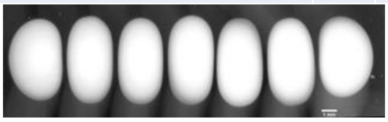

Depostion duration	30 sec
Deposition length	35,26 mm
Flow rate	1.5 μl/min
Applied Voltage	-6.3 kV
Configuration	B
Deposition length/over sprayer array length	1.22

Depostion duration	30 sec
Deposition length	21,1 mm
Flow rate	1.5 μl/min
Applied Voltage	-7,25 kV
Configuration	B
Deposition length/over sprayer array length	1.54

Figure 3.8: As the pitch is decreasing the deposition spots become distorted. LEsS of 7-in total- emitters, scale bars are 1 mm, Q=1.5 μl/min, RH=19 percent, T=28.9 C, H=20.3 mm, solution= BREC, parameters same for all depositions.

<u>Observation 2:</u> The end electrode configurations influence the produced deposition spots as they suppress the outward expansion of the extreme spots and decrease the total deposition length (rows 1-3 of Fig. 3.8).

A comparison between column 1 and 2 of Fig. 3.8 shows the effect of the pitch on the deposition spots under the same other parameters. For an inter-emitter pitch (P=4.3 mm) the spots are squeezed and elongate in the orthogonal to the LEsS axis direction, but stay aligned in the LEsS axis direction. However, for an even smaller pitch of P=2.5 mm both the alignment of the spots and the spot symmetry are broken.

The orderly appearance of the deposition spots in column one is more practical for the collection of particles while smaller pitch is preferable for the scale-up of the LEsS. Based on observations 1 & 2, I introduced a horizontal electrode parallel to and at 1 pitch distance from the emitters axis at the same potential as the emitters. This horizontal electrode controls the tilting of the cones and deflects the Es plumes to the opposite direction producing orderly deposition spots at P=2.5 mm (Fig. 3.9).

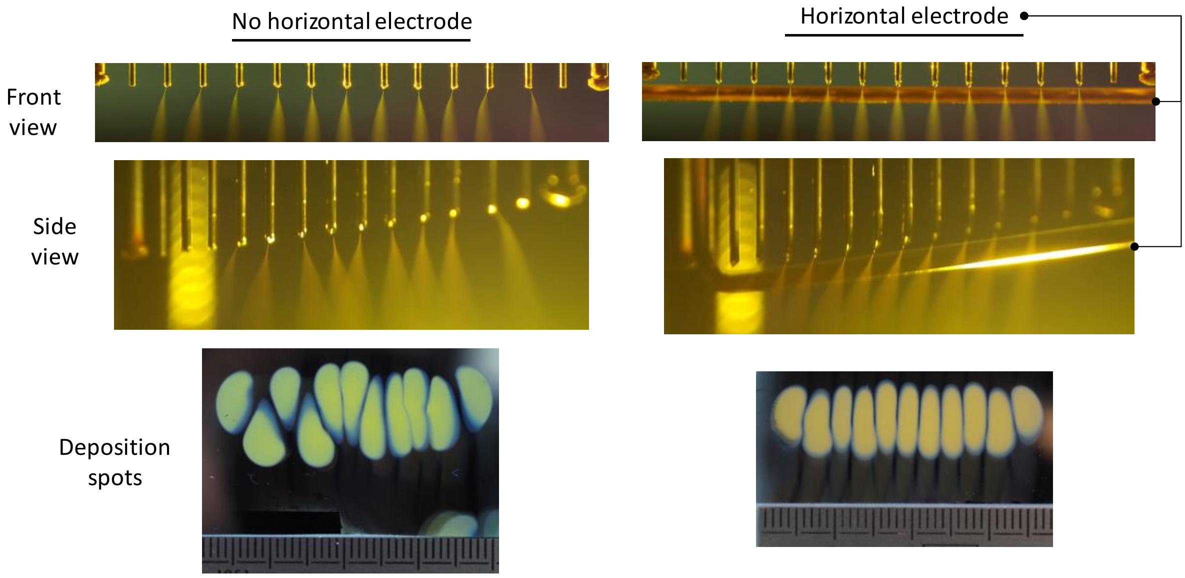

Figure 3.9: The effect of the horizontal electrode, almost eliminating the spot deformation and random misalignment from the array axis. LEsS of 11-emitters Q=0.7 μl/min, RH=28.7 percent, T=19.9 C, H=27.8 mm, solution= ECuPA, parameters same for all depositions.

To quantify the effectiveness of the horizontal electrode it was necessary to define the position of the deposition spots. This was done using the same images shown above and defining the center of mass for each spot with photo processing software. This point is what we from now on we will refer to as “spot position”. Combined the spot position analysis with the bottomview image of the emitters in the LEsS (method described in Fig. 3.4) the applied suppression of spot misalignment from the LEsS axis is apparent in Fig. 3.10. The applied voltage exceeded the scale of the data acquisition device (10.6 kV), but it can be said that the voltage required to operate the LEsS with the hor. electrode was 0.5 kV higher than without the hor. electrode.

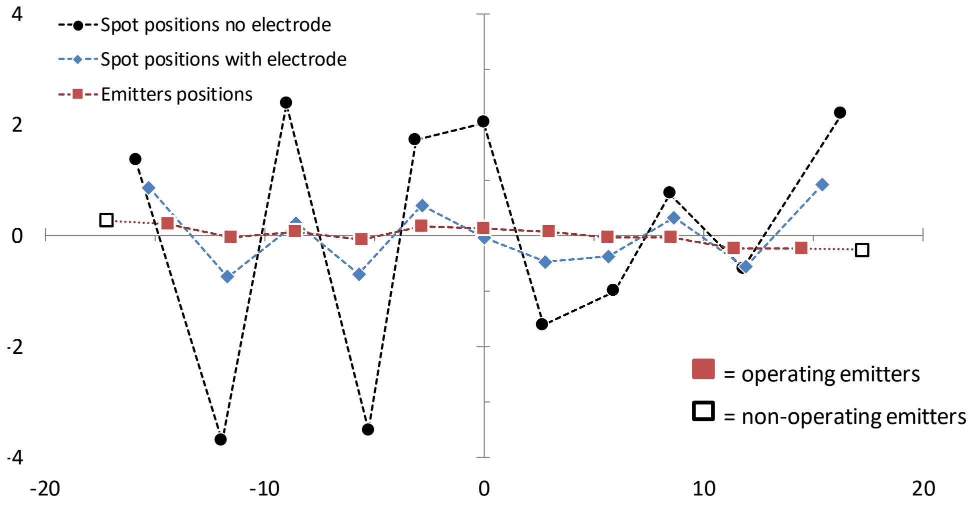

Figure 3.10: Spot positions under the same conditions with and without the horizontal electrode overlapped with the emitter positions.

3.3.3 Generated Particles

In this section the we demonstrate the LEsS versatility in producing particles. Ethyl Cellulose (EC) and Polyvinyl-pyrrolidone (PVP) were used to produce the polymer residues, while different solvents (Ethanol, Butanone, Acetic acid) and solvent additives (Rhodamine, Curcumin) were used to change solution properties (i.e. conductivity). The distance from tip to collector (H) was modified to control droplet drying as well as the flow rate (Q) through the emitters. A detailed review on polymer particle formation is presented in Bodnár et al., (2018).

For the EC, BREC solution, and the specific parameters of the system (Fig. 3.11) the particles assumed the shape of platelets upon collection with approximate sizes between 0.4- 0.8 micrometers, with uniform particle shapes and sizes, sampled out of all the deposition spots. EC has been proposed for controlled release of drugs (Li et al., 2017) as it is not water soluble, it is not suitable for our aim of enhancing Curcumin aqueous solubility.

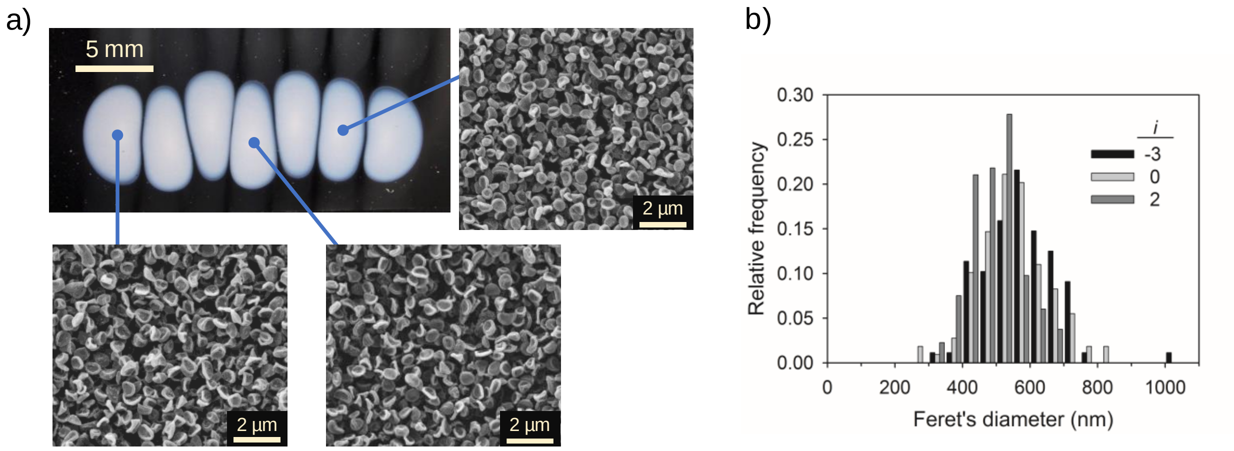

Figure 3.11: a) Particles produced using a 7-emitter LEsS showing the conformal shapes and sizes of the produced particles from all the emitters. b) corresponding histograms of particle sizes. Experimental parameters RH<20%, T=29.5 C, H=20 mm, P=2.5mm, Applied Voltage=9 kV, Q=1.5 µl/min, solution= BREC, configuration A. Deposition sample and Scanning Electron Microscope (SEM) images with scale bars.

PVP on the other hand is a water-soluble polymer, approved by the FDA as drug excipient. It has also been shown to act as a solid dispersion to improve water solubility of organic substances (Tachibana et al., 1965). Other advantages of PVP as candidate drug carrier is its antifouling properties (Munch et al., 2018) and its extensive usage in commercial pharmaceutical products.

Initially solution EP was prepared and used with the 11-emitter LEsS. The produced particles were between 100 nm and 2 μm. At the outer region (halo) particles seemingly arrived wet because they collapsed to continuous structures (Fig. 3.12). Additional solution optimization using the single emitter setup was done to come up with the solutions EPCuPA1 and EPCuPA2.

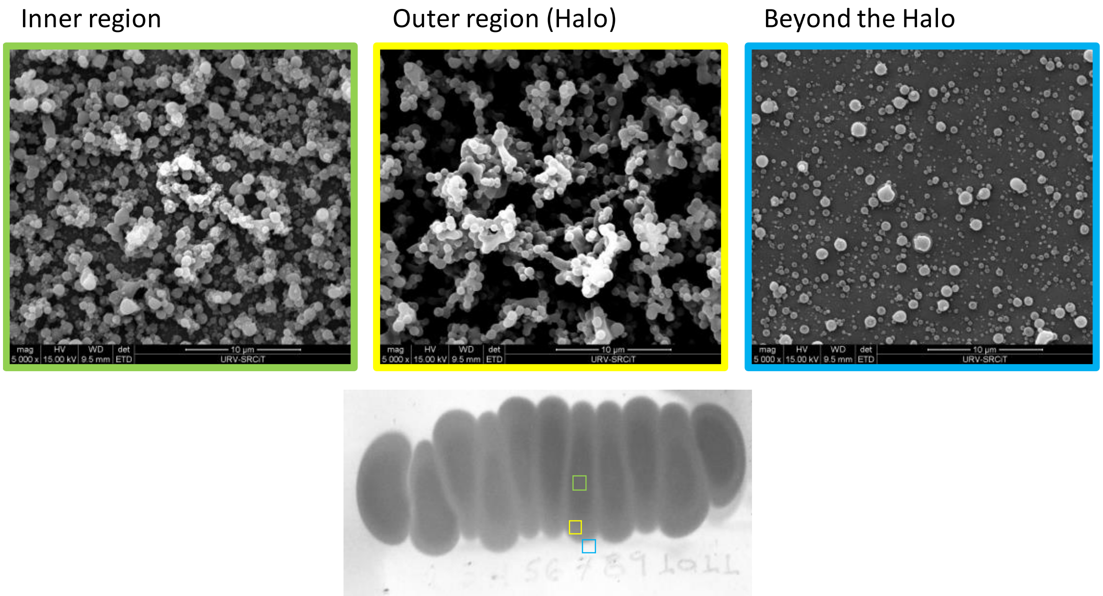

Figure 3.12: SEM images at the POIs marked on the Si collector sample. RH=29.9 %, T=21.4 C, H=25 mm, P=2.5mm, applied voltage>10.6 kV, Q=0.85 μl/min, solution= EP. The spot deposition's tone is inverted (negative) for improved contrast.

Curcumin and Ethanol was added to solution EP to create solution ECuPA1. This solution was electrosprayed operating 4-emitter of the LEsS. The produced particles had an elongated spindle shape with a long axis between 1-4 μm (Fig. 3.13).

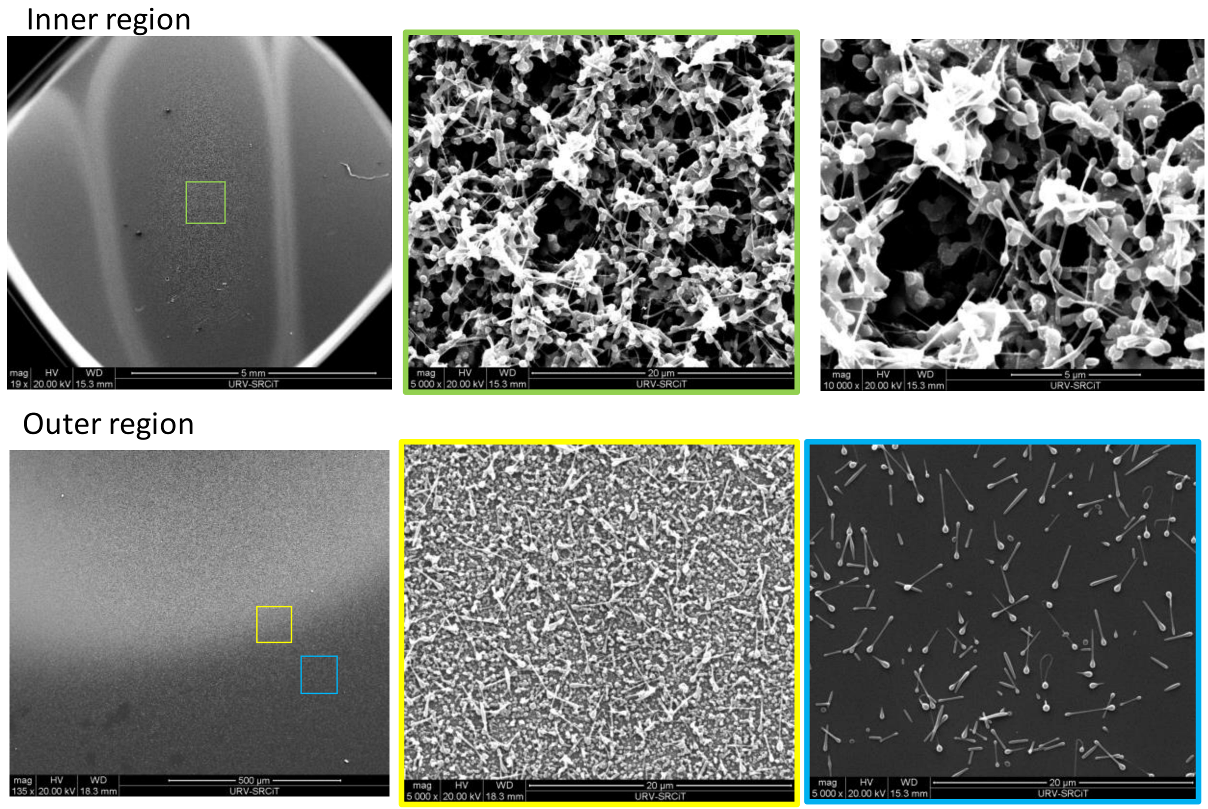

Figure 3.13: Representative SEM images at different locations of the 4 deposition spots. RH=25.7 %, T=21.2 C, H=25 mm, P=2.5mm, applied voltage>10.6 kV, Q=0.75 µl/min, solution= EPCuPA1

Particles in the inner region of each of the 4 spots have the same morphologies, spindle shape and sizes. The situation changes as we approach the outer border region of each spot similarly in all directions as shown in the second row of figure 3.13. At the outer regions the particle population decreases and particle shapes and sizes vary heavily. These polymer residues originate from both primary and satellite droplets generated upon jet breakup.

Es from 9 operating emitters of the LEsS on paper was performed to verify that there were no structural changes on the produced particles. The produced particles had the same size and quite similar morphology, shown in Fig. 3.14.

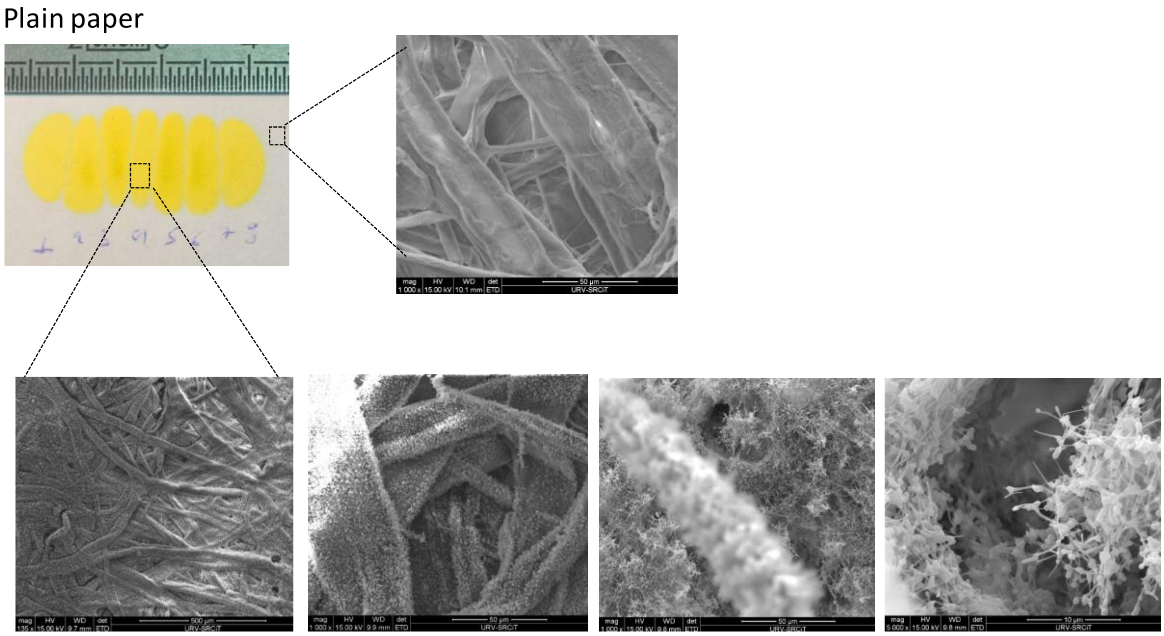

Figure 3.14: SEM images of the blank paper (shown on the first row) and deposited Curcumin-PVP particles. RH=25.7 %, T=21.2 C, H=25 mm, P=2.5mm, applied voltage>10.6 kV, Q=0.75 µl/min, solution= EPCuPA1. Observed distortion of the images is caused by the charge up of the paper, in the vacuum of the SEM despite the applied gold coating.

The polymer curcumin particle formulation premise is satisfied at this point as we have produced microrod shaped particles. It is interesting to point out, that rod shaped nano particles (~50 nm) have been reported in the literature to enhance bioavailability more than the commonly encountered spherical particles (Zhao et al.,2017). Based on the results shown in Fig. 3.13 and Fig. 3.14, the LEsS system can be optimized to produce microrod shaped particles.

Nevertheless, smaller particles (<1 µm) are known to have better bioavailability. In order to decrease the size of our particles, a new SOLUTION was prepared. The distance emitter tip to collector was increased and the flow rate was reduced. All these changes led to the collection of spherical particles shown in Fig. 3.15 and Fig. 3.16 with quite monodisperse average sizes of 500 nm in the central region of the collection spots. A scratch was deliberately done to show the homogeneity of the particle layers and absence of smaller particles in the bottom layers.

Inner region

spot 8 center- scratch

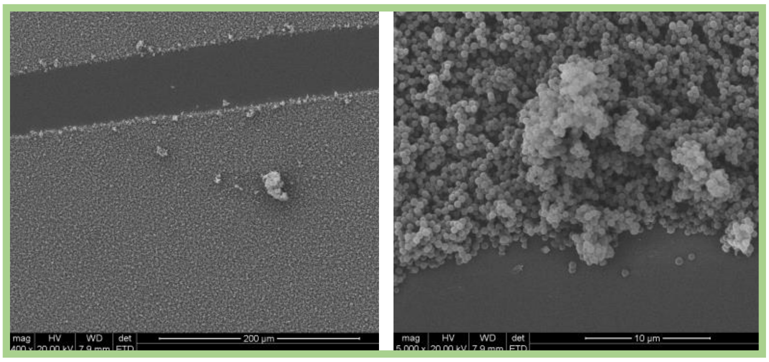

spot 9 center

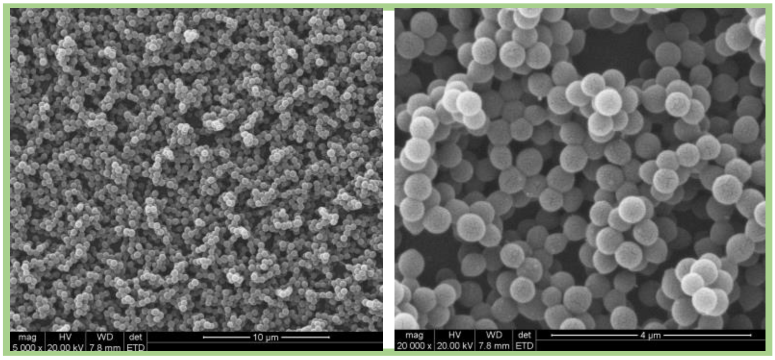

Figure 3.15: SEM images of spherical particles collected on a Si wafer. RH=31.4%, T=19.7 C, H=25 mm, P=2.5mm, applied voltage>10.6 kV, Q=0.5 µl/min, solution= EPCuPA2.

Inner region

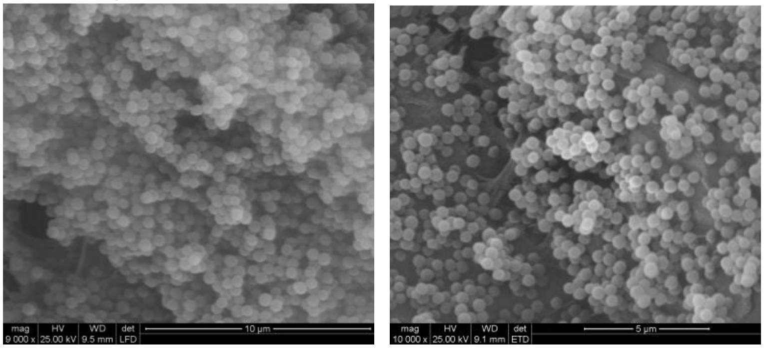

Figure 3.16: SEM images of spherical particles collected on paper. RH=31.4%, T=19.7 C, H=25 mm, P=2.5mm, applied voltage>10.6 kV, Q=0.5 µl/min, solution= EPCuPA2. Poor image quality is due to charge accumulation in SEM High Vacuum.

The particles collected on Si waffer do not have structural differences compared to the ones collected on paper, as discussed before. A separate experiment where the Si sample was weighed before and after a 13-min. 11-sec. deposition using 10-emitters resulted in a yield of 0.0123 gr/hour. Since the 3 min mark the array was not operating consistently in cone-jet mode. Some of the emitters were swiftly transitioning back and forth to intermittent mode suggesting charge accumulation of the sample. However, a moving collection surface is a quick solution to this issue for long term LEsS stability. Other methods such as neutralization of particles with soft x-rays, ionization or carrier gas flow has also been suggested for long term consistent operations of a multiplexed Es system.

Dissolution tests for the particle formulations were not performed. However, electrospun fibers of high molecular weight PVP were loaded with Curcumin in the work by Chuan Wang et al. (2015). The Curcumin was incorporated in the polymer matrix and showed improved solubility in vitro and potency as an orally administered anticancer drug in vitro animal testing.

3.4 Conclusions

Two different polymers (Ethyl cellulose and PVP) have been used to produce micro/nano particles of various morphologies demonstrating the particle engineering capability of the LEsS. Some other aspects from literature, were briefly mentioned like the capability of Es for crystal engineering another way to modify water solubility of an API.

Curcumin was chosen as a model API. Curcumin is intensively researched for its therapeutical properties but suffers from low bioavailiability due to its insolubility in water. The proposed
PVP – Curcumin formulation facilitates the dissolution in water. Furthermore, decreasing the particle sizes below 1 micrometer is expected to improve the API absorption through the gastrointestinal tract.

Paper is first time reported to be suitable for particle collection in the stable cone jet mode. The advantages are not only cheap price and wide availability but implores us to look into a other water absorbing, porous, materials (i.e. fabrics) traditionally considered “bad” collectors.

Taylor cone direction is manipulated with a horizontal electrode and create a uniform deposition pattern in well-arranged spots improving the particle-mass to surface ratio on the collection surface.

Regarding the scale-up capability of a LEsS; we operated up to 11-emitters but from our previous work (chapter 1) it is shown that the system can be scaled up to a very large number of simultaneously operating emitters. A 1000 emitter LEsS (assuming consistent operation) could produce 1.13 gr / hour of particulate matter, with an array length of 2.5 m. Stacking up of LEsS is also an option where the spacing between each line can be as small as 10 mm where electrostatic interactions would be negligible.

3.5 References

Bharat B. Aggarwal, Young-Joon Surh, S. S. (2007). The Molecular Targets and Therapeutic Uses of Curcumin in Health and Disease. doi.org/10.1021/acs.bioconjchem.7b00646

Bober, D.B., Chen, C.-H., 2011. Pulsating electrohydrodynamic cone-jets: from choked jet to oscillating cone. J. Fluid Mech. 689, 552–563. https://doi.org/10.1017/jfm.2011.453

Bodnár, E., & Rosell-Llompart, J. (2013). Growth dynamics of granular films produced by electrospray. Journal of Colloid and Interface Science, 407, 536–545. https://doi.org/10.1016/j.jcis.2013.06.013

Bodnár, E., Grifoll, J., and Rosell-Llompart, J. (2018). Polymer solution electrospraying: A tool for engineering particles and films with controlled morphology. J. Aerosol Sci., 125:93–118.

Carrilho, E., Martinez, A. W., & Whitesides, G. M. (2009). Understanding wax printing: A simple micropatterning process for paper-based microfluidics. Analytical Chemistry, 81(16), 7091–7095. https://doi.org/10.1021/ac901071p

Cartiera, M. S., Ferreira, E. C., Caputo, C., Egan, M. E., Caplan, M. J., & Saltzman, W. M. (2010). Partial correction of cystic fibrosis defects with PLGA nanoparticles encapsulating curcumin. Molecular Pharmaceutics, 7(1), 86–93. https://doi.org/10.1021/mp900138a

Chauhan, V. P., Stylianopoulos, T., Martin, J. D., Chen, O., Kamoun, W. S., Bawendi, M. G., & Fukumura, D. (2012). Normalization of tumour blood vessels improves the delivery of nanomedicines in a size-dependent manner. NIH Public Access, 7(6), 383–388. https://doi.org/10.1038/nnano.2012.45.Normalization

Daerr, A., & Mogne, A. (2016). Pendent_drop: an imageJ plugin to measure the surface tension from an image of a pendent drop. Journal of Open Research Software, 4, 2–6. https://doi.org/10.5334/jors.97

Demmons, N. R., Lamarre, N., Ziemer, J. K., Parker, M., & Spence, D. (2016). Electrospray Thruster Propellant Feedsystem for a Gravity Wave Observatory Mission (AIAA 2016-4739). In 52nd AIAA/SAE/ASEE Joint Propulsion Conference. American Institute of Aeronautics and Astronautics. https://doi.org/doi:10.2514/6.2016-4739

Deng, W., & Gomez, A. (2011). Electrospray cooling for microelectronics. International Journal of Heat and Mass Transfer, 54(11–12), 2270–2275. https://doi.org/10.1016/j.ijheatmasstransfer.2011.02.038

Djairam, D., Morshuis, P. H. F., & Smit, J. J. (2014). A Novel Method of Wind Energy Wind Energy Converter. IEEE Electrical Insulation Magazine, 30(4), 8–20. https://doi.org/10.1109/MEI.2014.6843763

Eagles, P. A. M., Qureshi, A. N., & Jayasinghe, S. N. (2006). Electrohydrodynamic jetting of mouse neuronal cells. Biochem. Journal, 394, 375–378. https://doi.org/10.1042/BJ20051838

Fenn, J. B., Mann, M., Meng, C. K., Wong, S. F., & Whitehouse, C. M. (1989). Electrospray ionization for mass spectrometry of large biomolecules. Science, 246(4926), 64–71. Retrieved from http://science.sciencemag.org/content/246/4926/64.abstract

Gad, S. E., & Sullivan, D. W. (2014). Generally Recognized as Safe (GRAS). Encyclopedia of Toxicology: Third Edition, (686), 706–709. https://doi.org/10.1016/B978-0-12-386454-3.00848-4

Hwang, W., Xin, G., Cho, M., Cho, S. M., & Chae, H. (2012). Electrospray deposition of polymer thin films for organic light-emitting diodes. Nanoscale Research Letters, 7(1), 52. https://doi.org/10.1186/1556-276X-7-52

Jaworek, A., Balachandran, W., Lackowski, M., Kulon, J., & Krupa, A. (2006). Multi-nozzle electrospray system for gas cleaning processes. Journal of Electrostatics, 64(3–4), 194–202. https://doi.org/10.1016/j.elstat.2005.05.006

Jurenka, J. (2009). Anti-inflammatory Properties of Curcumin, a Major Constituent of Curcuma longa: A Review of Preclinical and Clinical Research. Alternative Medicine Review, 14(2), 141–151

Lan, W. J., Maxwell, E. J., Parolo, C., Bwambok, D. K., Subramaniam, A. B., & Whitesides, G. M. (2013). Paper-based electroanalytical devices with an integrated, stable reference electrode. Lab on a Chip, 13(20), 4103–4108. https://doi.org/10.1039/c3lc50771h

Lee, Y. H., Bai, M. Y., & Chen, D. R. (2011). Multidrug encapsulation by coaxial tri-capillary electrospray. Colloids and Surfaces B: Biointerfaces, 82(1), 104–110. https://doi.org/10.1016/j.colsurfb.2010.08.022

Li, X.-Y., Zheng, Z.-B., Yu, D.-G., Liu, X.-K., Qu, Y.-L., & Li, H.-L. (2017). Electrosprayed sperical ethylcellulose nanoparticles for an improved sustained-release profile of anticancer drug. Cellulose, 24(12), 5551–5564. https://doi.org/10.1007/s10570-017-1498-0

Loscertales, I. G., & Gañán-Calvo, A. M. (2002). Micro / nano encapsulation via electrified coaxial liquid jets. Science, 295(5560), 1695–1698. https://doi.org/10.1126/science.1067595

Mehta, P., Haj-Ahmad, R., Rasekh, M., Arshad, M. S., Smith, A., van der Merwe, S. M.,Ahmad, Z. (2017). Pharmaceutical and biomaterial engineering via electrohydrodynamic atomization technologies. Drug Discovery Today, 22(1), 157–165. https://doi.org/10.1016/j.drudis.2016.09.021

Mouthuy, P. A., Škoc, M. S., Gašparović, A. Č., Milković, L., Carr, A. J., & Žarković, N. (2017). Investigating the use of curcumin-loaded electrospun filaments for soft tissue repair applications. International Journal of Nanomedicine, 12, 3977–3991. https://doi.org/10.2147/IJN.S133326

Münch, A. S., Wölk, M., Malanin, M., Eichhorn, K. J., Simon, F., & Uhlmann, P. (2018). Smart functional polymer coatings for paper with anti-fouling properties. Journal of Materials Chemistry B, 6(5), 830–843. https://doi.org/10.1039/c7tb02886e

Patil, S., Mahadik, A., Nalawade, P., & More, P. (2017). Crystal engineering of lactose using electrospray technology: carrier for pulmonary drug delivery. Drug Development and Industrial Pharmacy, 43(12), 2085–2091. https://doi.org/10.1080/03639045.2017.1371733

Pyrgiotakis, G., Vasanthakumar, A., Gao, Y., Eleftheriadou, M., Toledo, E., Dearaujo, A.,Demokritou, P. (2015). Inactivation of foodborne microorganisms using engineered water nanostructures (EWNS). Environmental Science and Technology, 49(6), 3737–3745. https://doi.org/10.1021/es505868a

Rajiv Saini, Santosh Saini, S. S. (2010). Nanotechnology: The future medicine. Journal of Cutaneous and Aesthetic Surgery, 3(1), 32–33. https://doi.org/10.4103/0974-2077.63301

Rietveld, I. B., Kobayashi, K., Honjo, T., Ishida, K., Yamada, H., & Matsushige, K. (2010). Electrospray induced ferroelectricity in poly(vinylidene fluoride) thin films. Journal of Materials Chemistry, 20(38), 8272. https://doi.org/10.1039/c0jm01265c

Rodríguez-Pérez, D., Castillo, J. L., & Antoranz, J. C. (2007). Density scaling laws for the structure of granular deposits. Physical Review E - Statistical, Nonlinear, and Soft Matter Physics, 76(1), 1–5. https://doi.org/10.1103/PhysRevE.76.011407

Rosell-Llompart, J., Grifoll, J., & Loscertales, I. G. (2018). Electrosprays in the cone-jet mode: From Taylor cone formation to spray development. Journal of Aerosol Science, In press. https://doi.org/10.1016/j.jaerosci.2018.04.008

Rostad, C. E., & Hostettler, F. D. (2007). Profiling refined hydrocarbon fuels using polar components. Environmental Forensics, 8(1–2), 129–137. https://doi.org/10.1080/15275920601180677

Smith, D.P.H., 1986. The electrohydrodynamic atomization of liquids. IEEE Trans. Ind. Appl. IA-22, 527–535. https://doi.org/10.1109/TIA.1986.4504754

Sochorakis, N., Grifoll, J., and Rosell-Llompart, J. (2018). Scaling up of extractor-free electrosprays in linear arrays. Chem. Eng. Sci., In Press. https://doi.org/10.1016/j.ces.2018.09.006

Stachewicz, U., Stone, C. A., Willis, C. R., & Barber, A. H. (2012). Charge assisted tailoring of chemical functionality at electrospun nanofiber surfaces. Journal of Materials Chemistry, 22(43), 22935–22941. https://doi.org/10.1039/c2jm33807f

Tachibana, T., & Nakamura, A. (1965). A methode for preparing an aqueous colloidal dispersion of organic materials by using water-soluble polymers: Dispersion of B-carotene by polyvinylpyrrolidone. Kolloid-Zeitschrift & Zeitschrift Für Polymere, 203(2), 130–133. https://doi.org/10.1007/BF01507758

Ting, J. M., Porter, W. W., Mecca, J. M., Bates, F. S., & Reineke, T. M. (2018). Advances in Polymer Design for Enhancing Oral Drug Solubility and Delivery. Bioconjugate Chemistry, https://doi.org/10.1021/acs.bioconjchem.7b00646

Wang, C., Ma, C., Wu, Z., Liang, H., Yan, P., Song, J., … Zhao, Q. (2015). Enhanced Bioavailability and Anticancer Effect of Curcumin-Loaded Electrospun Nanofiber: In Vitro and In Vivo Study. Nanoscale Research Letters, 10(1), 1–10. https://doi.org/10.1186/s11671-015-1146-2

Williams, H. D., Trevaskis, N. L., Charman, S. A., Shanker, R. M., Charman, W. N., Pouton, C. W., & Porter, C. J. H. (2013). Strategies to Address Low Drug Solubility in Discovery and Development. Pharmacological Reviews, 65(1), 315–499. https://doi.org/10.1124/pr.112.005660

Zelikin A,,2018 personal communication

Zhao, Y., Wang, Y., Ran, F., Cui, Y., Liu, C., Zhao, Q., … Wang, S. (2017). A comparison between sphere and rod nanoparticles regarding their in vivo biological behavior and pharmacokinetics. Scientific Reports, 7(1), 1–11. https://doi.org/10.1038/s41598-017-03834-2

Chapter 4

EHD direct printing of protein - DNA solutions for paper-based biosensors

Abstract

Paper one of humanity's oldest technological achievements has been retrofitted into high-tech devices. Foldable electronics, microfluidic devices and biosensors are few of the new areas of application. Not only, is paper common, cheap and biodegradable, it is also the model platform for our current printing technology. These characteristics make it the perfect candidate for the development of low cost biosensors in the form of lateral flow assays, able to revolutionize point-of-care diagnostics. We developed an Electrohydrodynamic (EHD) printing device that can jet-print or electrospray lines directly on cellulose or nitrocellulose paper with no prior treatment. A laminar co-axial gas co-flow around the EHD emitter proved detrimental for stabilizing a cone-jet of a water based solution without corona discharges. The advantage of our EHD method is the size of the printed features which are several times smaller than the emitter capillary ID preventing clogging of the device. Additionally, the EHD method does not require high pressure to produce the liquid jet, that in some cases has been shown to damage sensitive biological "inks". The three "inks" used in this work are water based protein solutions without any other polymer addition: a) HRP (horseradish peroxidase) protein for direct evaluation of the protein activity, initial testing and setup optimization, b) single-chain form of the Cro DNA binding protein (scCro) for the test line on the lateral flow assay and c) pre-incubated streptavidin-biothynlated DNA probe for the control line on the lateral flow assay.

It is demonstrated that EHD deposited proteins and DNA retain their activity and ability to bind their matching complexes, qualifying the EHD deposition methods (jet print and electrospray) of biological species directly onto paper-based surfaces as an excellent alternative for bioprinting.

Keywords: EHD jetting, bioprinting, DNA binding protein, paper, biosensors, nitrocellulose.

4.1 Introduction

With the adaptation of printing technologies and the development of new "inks" it became possible to print electrical circuits (Khan et al., 2012), biomolecules (Li, et al., 2015), polymer microfluidics (Sun et al., 2015). As paper has been the model platform of the printing industry for decades, it is now retrofitted to a new age material (Wu et al., 2018). Paper is biodegradable, flexible, foldable and most importantly cheap and globally available. Paper based biosensors hold the premise to revolutionize modern day diagnostics especially in low resource regions of the planet (Carrilho et al., 2009, (Morbioli et al., 2019). The purpose of this research is to demonstrate the capability of electrohydrodynamic (EHD) deposition techniques, as potential candidates for single-step, direct printing of water-based protein solutions on paper platforms. It has been demonstrated that EHD deposition is a gentle method that does not damage biomolecules even complex and sensitive ones such as proteins and enzymes (Gomez et al., 1997, Morozov & Morozova,1999a, Morozov, 2009, Jayasinghe et al., 2006, Shigeta et al., 2012). Additionally, the capillary emitter size is several times bigger than the EHD emission point. This allows for large bio-macromolecules to flow freely without clogging the capillary emitter, in contrast with the tiny capillaries used in other techniques such as inkjet printing, and achieve similar deposition feature sizes (Gonzalez-Macia et al., 2010, Loh et al., 2008).

The lateral flow assays (LFA) are a paper-based platform for the detection of analytes in mixtures.The sample is placed on one end of the platform and under the effect of capillary action, it is absorbed through the platform passing various detection zones (printed lines). The results are visible within 6–30 min.A brief review that describes the mechanism of lateral flow assays is the one by Koczula & Gallotta, 2016.A typical nitrocellulose (Nc) detection strip is depicted in Fig. 4.1.

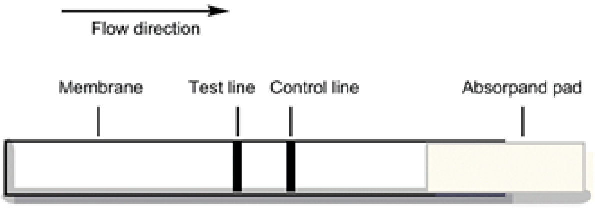

Figure 4.1: A typical lateral flow assay strip. The vertical black “Test line” represents the colorimetric signal produced upon target detection. The “Control line” appears in all cases, when there is flow through the LFA and verifies the LFA function.

Based on the findings of chapter 3 where we discovered that it was possible to deposit material directly on paper using EHD methods and we decided to apply this technique in depositing proteins for lateral flow assay biosensors. Even though our initial idea was to use stencil-masks and electrospray to deposit the line patterns on the strips (as has been shown before for conducting substrates by Morozov & Morozova, 1999b), during the initial phase of the experiments we observed that at high enough flow rates when using the gas co-flow system the jet wouldn’t brake up and would form a long thin liquid filament from the tip of the emitter to the Nc strip. Adjusting the liquid flow-rate we could control the width of the filament to approximately the width of the lines we wanted to produce for the biosensors but without the need for a stencil mask. We decided to look as well into the EHD jetting method as an alternate protein deposition method. Because of the apparent similarities with EHD jetting, we use the term EHD direct jet-printing to denote the direct application on paper like material like Nc. Direct deposition on nitrocellulose paper or plain paper substrates has not been previously reported using the EHD direct writing technique with any liquid (US patent US3949410A, only mentions **conducting** paper).

A gas co-flow is documented to enhance the performance of EHD jetting with a polymer solution (Lübbert et al.,2018, Zheng et al., 2016, He et al., 2013). Co-flow assisted EHD-jet printing as a term has been used by Tse and Barton at 2015, for the purpose of printing small features at low liquid flow rates. The main difference with the method used here is that the co-flow was at an angle relevant to the EHD emitter that breaks-up the jet in a train of droplets. We used a co-flow system that surrounds the EHD emitter with a gas layer which helped stabilizing the electrospray in cone-jet mode, as well as the EHD-jet for EHD direct printing of aqueous protein solutions, without the need for a controlled atmosphere chamber.

Horse Radish Peroxidase (HRP) enzyme catalyzes a chromogenic or chemiluminescent substrate to generate a quick and easy to detect response. Therefore, HRP is was used for verifying protein activity after the EHD deposition process and for optimizing the EHD jet printed trace.

However, for the assembly of a DNA-target detection LFA biosensor we used the novel, modular configuration shown by Aktas et al. 2017, of a DNA sensing platform, which was modified to provide signal upon specific DNA target detection without the use of enzymes. Our modification uses carbon nanoparticles that give a black line colorimetric signal on the Nc strip upon DNA target detection. The whole system was EHD jet-printed onto a lateral flow biosensor that can be modified to detect different DNA targets by changing only the primer sequence where it binds to the target sequence of the Polymerase Chain Reaction (PCR) amplicon. The protein-DNA cascade probe was bio-engineered by Dr Gulsen Betul Aktas, in house (Aktas et al. 2017),

4.2 Materials and methods

PCR reagents and DNA oligonucleotides from were purchased from Fisher Scientific (Barcelona, Spain). Horseradish peroxidase (HRP) enzyme was provided from Alka Aesar (Barcelona, Spain). AEC (3-amino-9-ethylcarbazole) was provided from Sigma Aldrich (Barcelona, Spain). Carbon nanoparticles was kindly provided from Dr. Aart van Amerongen, Wageningen University. Hi-Flow plus HF-135 nitrocellulose membrane was purchased from Merck (Madrid, Spain). All other reagents were purchased from Fisher Scientific (Barcelona, Spain), Sigma-Aldrich (Madrid, Spain), and Scharlau (Barcelona, Spain). The high voltage power supply is an Ultravolt, HV-RACK-4-250-0032, 0 to 15 kV range.

Electrospray deposition experimental setup

In figure 4.1 the schematic of the setup used for the electrospray experiments is presented. It is the same setup used for testing different solutions in chapter 3. The spraying emitter has 0.40 mm O.D. and I.D. 0.16 mm. The co-flow tube has an I.D. of 1.5 mm and an O.D. of 2.5 mm while it was filled with smaller capillaries to ensure laminar gas flow. The “collection slide” is a nitrocellulose paper (Nc-paper) strip covered with a mask. The slide is inserted under the spraying emitter. The mask only allows for the electrosprayed liquid to deposit on the nitrocellulose paper through a ~1 mm thick slit (Fig. 4.3) and produces a well-defined line upon removal; we have experimented with more mask designs and materials discussed later. The “spraying capillary emitter” is connected directly to the positive channel of a high voltage power supply, generating a positive electrospray and the “counter electrode” is grounded. The liquid is supplied by a syringe pump (KDS legacy 100) with dial-in flow rate input panel. The typical gas volumetric flow rate (Qg) range was between 90-150 ml/min, and for the liquid solution (Q) 0.01- 0.2 ml/hr. All experiments were performed in laboratory air where temperature (T) (21-27 °C) and relative humidity (RH) (25-60 %) were recorded for each experiment. To calculate the amount of protein deposited on the Nc we divide the total circular spot surface (S_t) with the surface of the slot (S_s) on the mask and multiply the ratio with protein concentration times the flow rate times the deposition time ($C_p \times Q \times t \times \frac{S_s}{S_t}$).

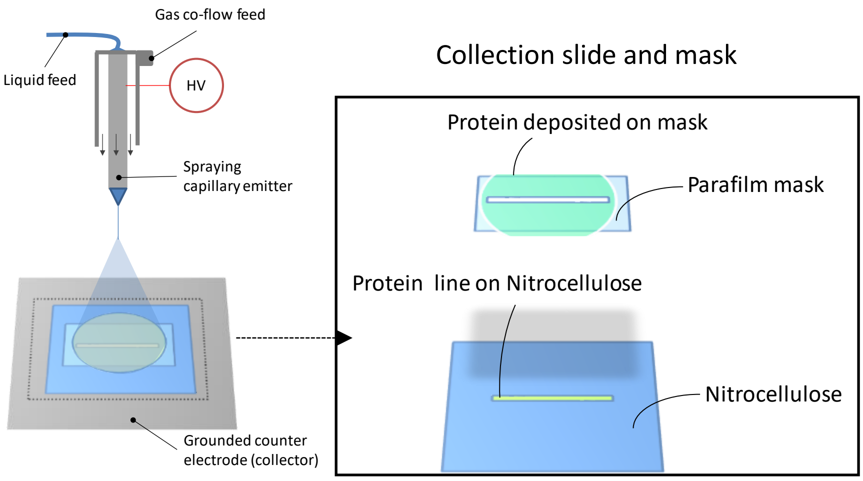

Figure 4.2: This is a schematic of a single emitter Es setup that has been used for trial solution testing

Direct EHD jet-printing experimental setup

The exact same emitter with a rotating-plate, in the role of the counter electrode, can be used to generate a long continuous jet of liquid (~10mm) of a smaller diameter than the capillary I.D. (Fig. 4.3). In order to print the liquid lines on nc-paper we need to move the collection slide, or the emitter. For this reason, we introduced a metallic rotating collector stage (5 cm radius) as seen in the sketch of Fig. 4.3 (a). An electric motor rotates the stage and the rotation speed is controlled reproducibly by adjusting the input voltage. To deduce the amount of protein deposited we calculate how much protein is deposited for a single rotation and then multiply with the number of rotations or passes.

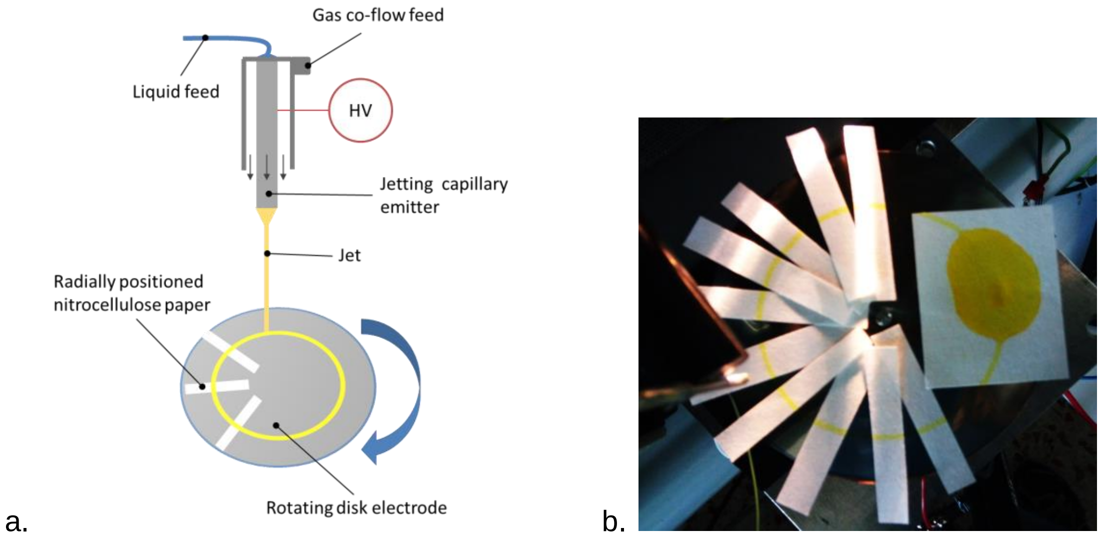

Figure 4.3: (a) The EHD jet printing emitter setup (same as Fig. 4.1) and the rotating collector, (b) Top view of a test EHD jet print using ethanol pigmented with curcumin, the big spot is where the jet is deposited initially before starting the rotation of the platform. Q= 1.5 ml/hr, Qg=243 ml/min, revolution time (tr) 1.24 ms.

Sometimes the jet may be tilted but maintains the same angle throughout the experiments meaning that the “printed” trail is a circle and the portions printed on the strips can be considered as straight lines with good approximation (Fig. 4.3b). The nitrocellulose paper (Ncw paper) strips were cut manually to 5 mm width and 25 mm length.

Nitrocellulose paper by itself is a brittle material. For the lateral flow assay applications, it comes in A4 sheets with an attached support material of insulating plastic termed Ncw hereforth. The support plastic is an additional challenge for us as now the deposition Nc surface is not in direct contact with the ground counter-electrode. We inserted the strips in a chamber for 30 seconds, where a piezoelectric atomizer was operated creating a humid water environment RH~97% to pre-moisturize the strips and then wrapped one end of the Ncw with aluminum foil that is in contact with the upper nitrocellulose layer and the grounding counter electrode. This was done to create a discharge path around the insulating plastic support. This step was not necessary when we Nc paper or normal paper. The temperature (T) and relative humidity (RH) were measured using the Vaisala HM34 handheld meter.

Determination of bioactivity of electrospray and EHD-jet deposited proteins

It is key feature to preserve the functional properties of the deposited proteins upon electrospray-electrojet and upon subsequent impact of the charged electrospray proteins with a substrate surface. The catalytic activity of the electro spray and EHD-jet deposited horse-radish peroxidase (HRP) is verified by adding the appropriate substrate that reacts with HRP to give a color-signal. First, different dilutions of the HRP enzyme (3 - 36 nanograms) were sprayed from a water solution (in 5% glycerol) onto the nitrocellulose surface. The nitrocellulose membranes were then incubated at room temperature for 1 hour to dry up. The EHD deposited HRP strips were incubated at 4 °C until use. Following, freshly prepared chromogenic dye (1 mM 3-amino-9-ethylcarbazole (AEC) and 1 mM hydrogen peroxide in 100 mM potassium phosphate pH 5) were used as substrate and incubated on nitrocellulose substrate for 5 min at room temperature, this process is called “development” a term borrowed from photography. The precipitated colour intensity and HRP activity was evaluated using ImageJ software and signal intensities were plotted against the amount of the HRP deposited.

Detection of PCR amplicon by NALFA (Nucleic Acid Lateral Flow Assay)

The test line and control line of the lateral flow assay, scCro DNA binding protein and dHP DNA binding protein respectively are printed in two steps by EHD jet printing method on the LFA surface for signal generation via conjugation to carbon nanoparticles (CNPs). The target DNA is amplified by PCR prior to use to increase the specificity and sensitivity in lateral flow assay (LFA). In our case target DNA amplify with the specific binding sequence of the bacteriophage lambda Cro DNA binding protein on forward primer and specific binding sequence of headpiece domain of the Escherichia coli LacI repressor DNA binding protein on reverse primer without any need of labeling of the primer set. The resulting PCR amplicon contains a scCro dsDNA binding protein site at one end and the dHP dsDNA binding site at the other. In this form, PCR amplicon is ready to be captured and detected in a sandwich on the test line. Moreover, preincubated streptavidin-biothynlated dHP DNA binding site complex is also ready to use to be captured with dHP DNA binding protein-CNPs. (Figure 4.4) CNPs are widely used for the visual detection on lateral flow assay due to their good sensitivity and signal-to-noise ratio owing to the high contrast between the dark black color of carbon on the white nitrocellulose membrane background. The direct absorption of carbon nanoparticles to protein complexes is easy and they are stable in their conjugated form (Posthuma-Trumpie et al., 2009).

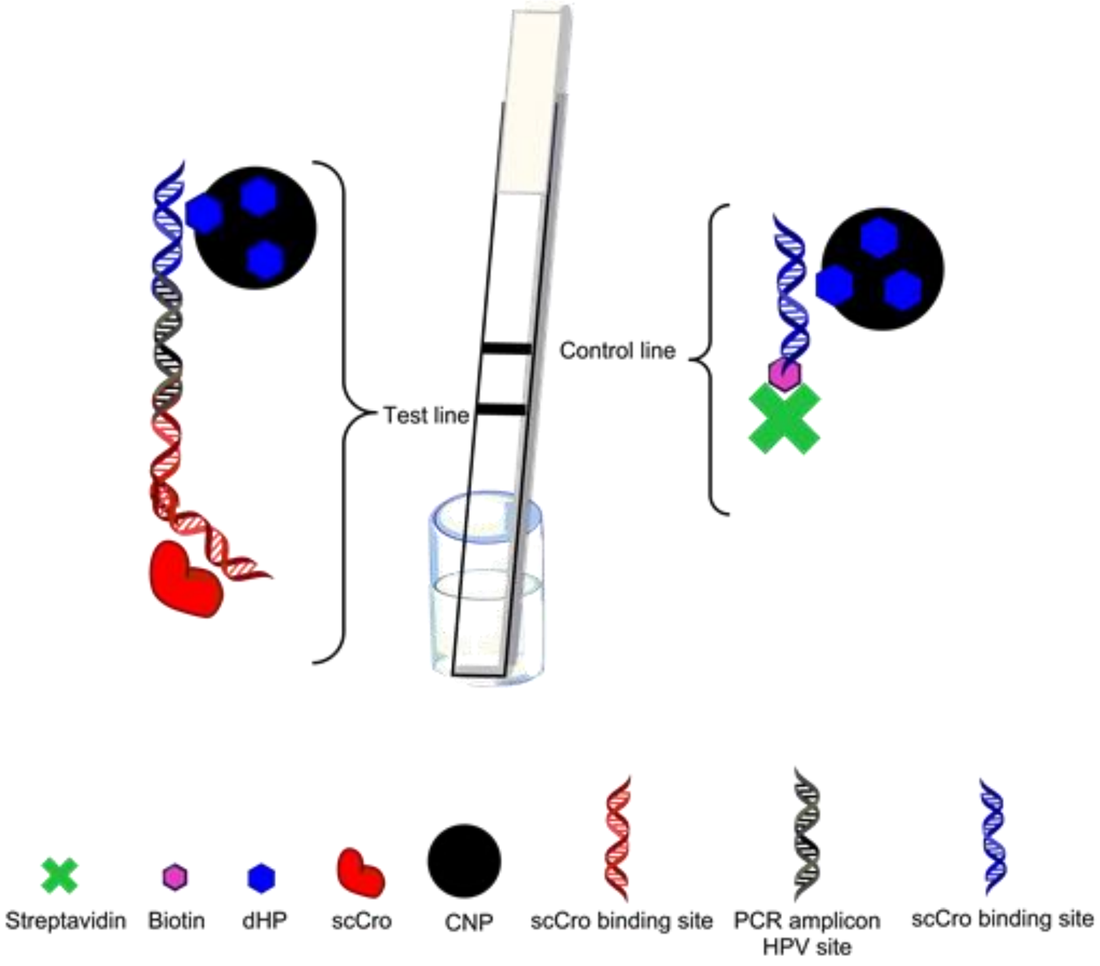

Figure 4.4: Detection of HPV16 gene via EHD jetted scCro DNA binding protein and dHP DNA binding protein-carbon nanoparticles.

The PCR amplicon with scCro DNA binding site on 5’ and dHP binding site on 3’ was sandwiched on the test line between scCro DNA binding protein and dHP/CNPs conjugate providing carbon black color. In the case of the control line EHD jetted streptavidin-biothynlated DNA probe complex was captured with dHP/CNPs conjugate.

For the LFA detection step the strips were dipped vertically in a low-binding 96-well microplate containing 100 ul of running-buffer (2 % BSA and 0.1 % Tween-20 in PBS) including the desired amount of the PCR amplicon. After reagents were absorbed through the whole length of the strips by the action of the capillary forces, the strips were dipped in 100 ul of running-buffer mixed with 1 ul of dHP/CNPs conjugate suspension. Black color signals from carbon nanoparticles were photographed after 10 minutes of incubation for qualitative results. The results were then compared within equal amount of electro spray deposited scCro and EHD jet printed scCro.

Polymerase chain reaction

The ssDNA gene target of human papilloma virus (HPV16) was used as target for the specific detection of HPV16. The primers used for the amplification of the target was designed according to literature. The forward was modified to include scCro DNA binding protein site while reverse primer was modified including dHP DNA binding protein site. PCR reaction was prepared total 50 ul including 1 ul of template, 0.25 ul Taq DNA polymerase, 1 ul of 10 mM dNTPs, 1 ul of each 10 mM primers and 5 ul of 10x standars Taq reaction buffer. Amplification was performed with an initial denaturation of 30 sec 95°C following by 25 cycles with a denaturation step 5 sec 95°C, annealing step of 5 sec at 58°C and an extension step of 5 sec 72°C, following by a final extension step of 1 sec 72°C. The PCR reactions were purified from ssDNA residues and primers using ethanol precipitation method. After the purification, dsDNA was suspended in MilliQ water, measured by UV absorbance 260 nm and calculated its concentration with its extinction coefficient.

Preparation of carbon nanoparticles – DNA binding protein conjugates

Carbon nanoparticles were labelled with DNA binding protein dimeric headpiece domain of the Escherichia coli LacI repressor protein dHP) following (Noguera et al., 2009) with minor modifications. In brief, 1 % (w/v) carbon (Spezial Schwartz 4, Degussa AG, Frankfurt, Germany) was prepared in Milli Q water and sonicated for 5 min (Branson model 250 Sonifier, Danbury, CT, USA). The carbon suspension diluted to 0.2% in binding buffer (5 mM carbonate-bicarbonate buffer pH 10.6) and sonicated for 5 min. Next, dHP binding protein was added to 0.2 % (w/v) carbon suspension and stirred overnight at 4 °C. Then, carbon nanoparticle-dHP suspension was centrifuged at 13,636xg for 15 min, supernatant was removed, and pellet was washed with washing buffer (5 mM borate pH 8.8, 1 % w/v BSA) to remove unbound protein. The washing procedure was performed for three times in total. After the washing procedure, pellet was resuspended in storage buffer (100 mM borate pH 8.8, 1% w/v BSA) and stored at 4 °C until use.

4.3 Results and discussion

Initial tests were carried out using HRP enzyme which given the appropriate substrate generates a color signal easy to detect by eye (colorimetric detection).
The parameters of the experiment are provided in Table 4.1. It is demonstrated (Fig.4.4) that, the electrospray can be stabilized in cone-jet mode, the stencil mask is working as expected

and the protein not only is deposited on the Nc paper (as would happen for a conducting substrate) but also maintained its activity. Moreover, the stability of the EHD deposited HRP checked after different time incubations.

Table 4.1

Q -liquid flow rate	0.6	(ml/hr)
Q_g- Gas flow rate	243	(ml/min)
H- tip to collector distance	13	(mm)
V_{HVPS}- Power Supply Voltage	7.9	(kV)
C_p – protein concentration	1.2	(mg/ml)
RH- Relative Humidity	39.5	(%)
T- Temperature	22	(ºC)
Solvent	water	
Deposition surface	Nc	
t- Deposition time	45	(sec)

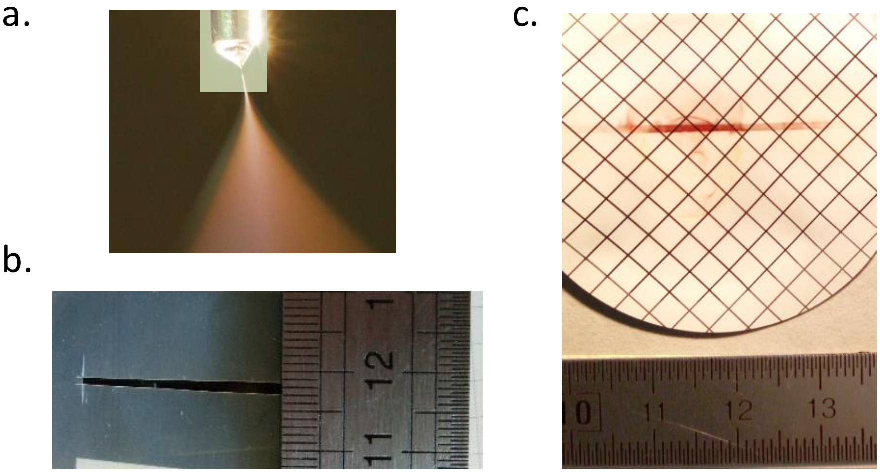

Figure 4.5: a. Composite image (darkfield & brightfield) of the electrospray operating in cone-jet mode b. The parafilm mask used on top of the nitrocellulose paper to create a proteinline and c. The HRP line after the addition of the AEC substrate for the development of the deposited trace. Total HRP mass electrosprayed ~900 ng .

From this point on all the deposition slides are nitrocellulose with plastic support backpacking (Ncw) and we follow the protocol described in the materials and methods section.

4.3.1 Comparing EHD- direct print method, electrospray deposition of HRP with mask and near-field electrospray deposition without mask.

The next experiment is a comparison between the electrospray deposition technique with a mask and the EHD-jet direct printing. The main issue with electrospray on a mask is wasting a lot of material depositing on the mask (even though it is an insulator). Additionally, the HRP is spread on more surface, which may be desirable for other applications but in a colorimetric assay reduces the intensity of the signal and therefore increasing the limit of detection (LOD). Table 4.2 holds the common parameters for both experiments while Fig. 4.6 shows the resulting lines after development and the amount of protein spent for each deposition.

HRP electrosprayed lines using mask and EHD-jet printed lines initial tests

Table 4.2

Q_g- Gas flow rate	155	(ml/min)
H- tip to collector distance	18	(mm)
V_{HVPS}- Power Supply Voltage	10	(kV)
C_p – protein concentration	0.05	(mg/ml)
RH- Relative Humidity	38.8	(%)
T- Temperature	19.7	(ºC)
Solvent	5% w/w glycerol in water	

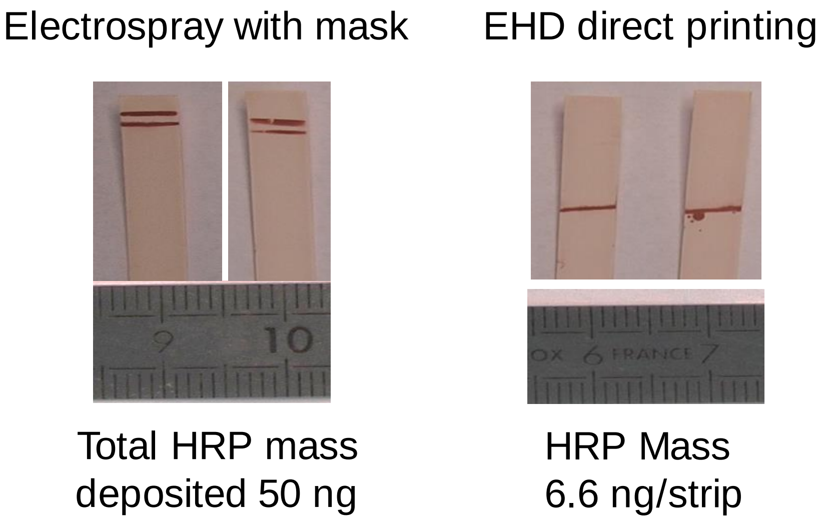

Figure 4.6: On the left Q=0.03 ml/hr, deposition time t=120 sec, On the right Q=0.7 ml/hr, average time that the emitter spends over each strip ts= 0.68 sec.

<u>Near field electrospray HRP spots (no mask)</u>

In the next experiment HRP was deposited with electrospray at very close proximity to the strips (near-field electrospray), bringing the emitter very close to the collector to avoid using a mask and therefore decrease the loss of material (parameters presented in table 4.3). Spot area (~32 mm^2) may be further reduced by decreasing emitter to collector distance (H). On the other hand, this technique does not produce the standardized line but a circular deposition spot (Fig. 4.7) Deposition time is only given for the 6 ng strip while it is multiplied by (HRP(ng) /6) for the rest. We designed this experiment to compare the results between electrospray and EHD-jet printing for equal mass of deposited protein.

Table 4.3

Q -liquid flow rate	0.03	(ml/hr)
Q_g- Gas flow rate	62	(ml/min)
H- tip to collector distance	3.4	(mm)
V_{HVPS}- Power Supply Voltage	8	(kV)
C_p – protein concentration	0.1	(mg/ml)
RH- Relative Humidity	35.6	(%)
T- Temperature	21.6	(ºC)
Solvent	5% w/w glycerol in water	
I-current	75	(nA)
t- Deposition time for the 6 ng strip	420	(sec)

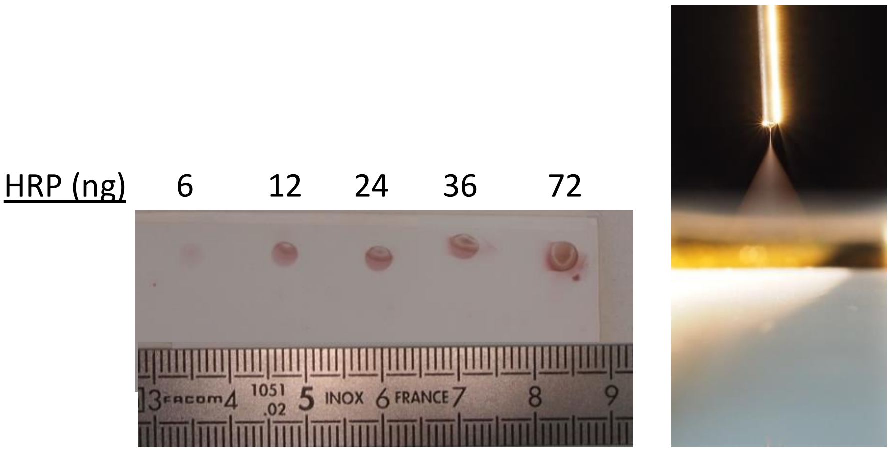

Figure 4.7: HRP spots after development with AEC deposited with near-field electrospray (without mask)

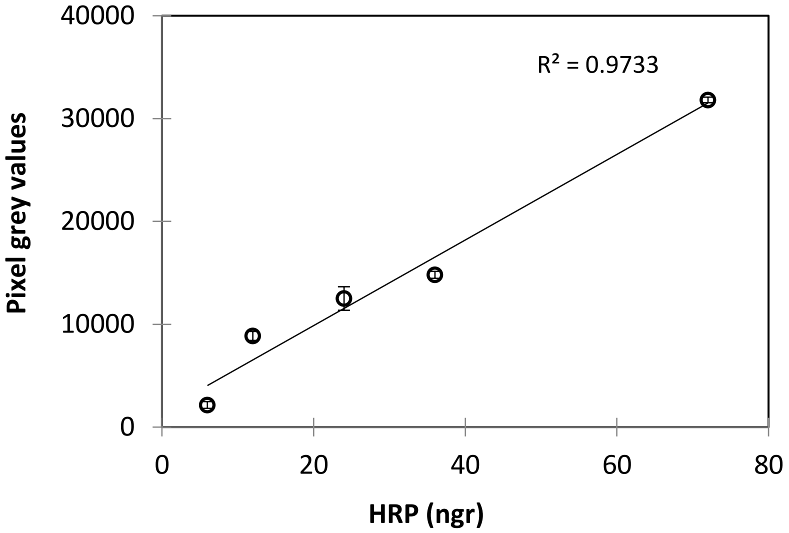

Figure 4.8: HRP calibration curve using the “maskless” electrospray method

The electrosprayed HRP provides visible color signal for as low as 6 ng of deposited enzyme. We don’t see the saturation plateau in the graph (Fig. 4.8)

In the last of our experiments with the HRP enzyme we used the EHD-jet printing technique to prepare the lines on the strips shown in Fig.4.9. The parameters of the experiment are presented in table 4.4.

Table 4.4

Q -liquid flow rate	0.7	(ml/hr)
Q_g- Gas flow rate	62	(ml/min)
H- tip to collector distance	9.5	(mm)
V_{HVPS}- Power Supply Voltage	9	(kV)
C_p – protein concentration	0.05	(mg/ml)
RH- Relative Humidity	35.0	(%)
T- Temperature	21.0	(ºC)
Composition	5% w/w glycerol in water	
t- Deposition time for the first strip (sec)	0.3	(sec)

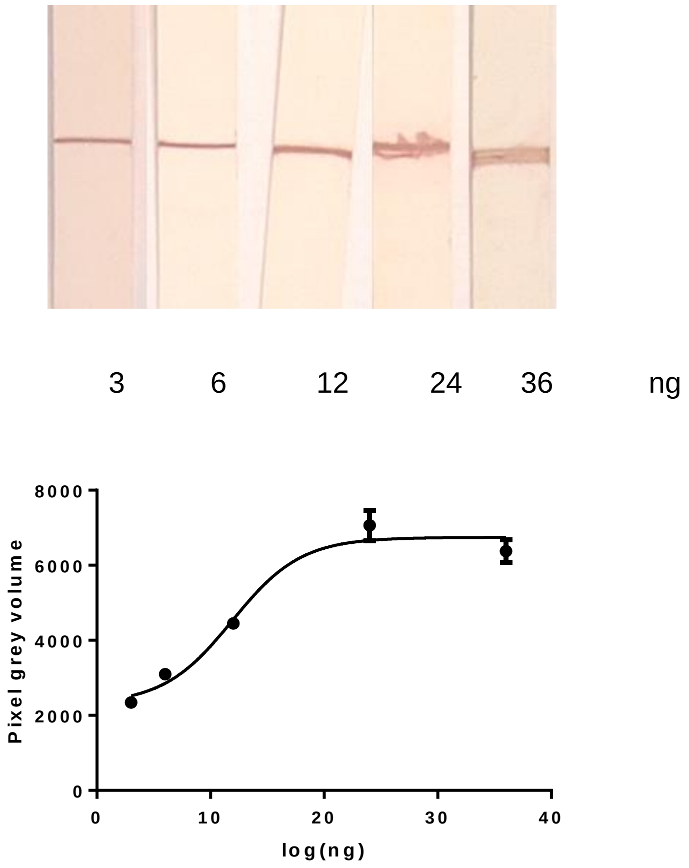

Figure 4.9:Developed lines of HRP protein deposited using the direct EHD-jet printing mode and LOD graph.

In fig. 4.9 not only the lines become more intense with the amount of HRP deposited but also become thicker which could be an effect of electrostatic charging as a result of the technique we used to print the lines; that is increasing the number of passes under the electrospraying emitter. In this case the 3 ng lines give a clear color signal while the signal quickly saturates with (Fig. 4.9 graph). From the experiments presented in section 4.3.1 we conclude that for the specific purpose of depositing lines the EHD-jet printing method provides more intense and clear signal for the same amount of deposited protein when compared to the electrospray method.

The electrospray wastes a lot of material deposited on the mask. Morozov and Morozova, 1999b propose a type of mask with multiple openings which reduces the overall area of the mask itself and limits the wasted solution. The near field electrospray can also be considered as a better method than electrospray with mask but with inferior results than the EHD-jet printing for the specific 'line printing" purpose.

4.3.2 Stability of the EHD jetted protein species

Not only the functionality and activity of the EHD-jet printed protein is important but also the viability and stability of the deposited protein for a long term stable biosensor. The stability is verified for different incubation timed after the EHD deposition process. In Fig. 4.10 , five strips, with 12 ng of HRP protein deposited on each, are developed after a maximum of 4 weeks stored at 4 °C. There is no observable change in the colorimetric signal intensity.

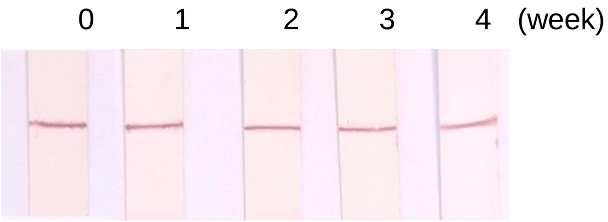

Figure 4.10: Activity check of EHD jet printed HRP protein on Ncw strip. The developed lines prove long term stability

4.3.2 Lateral flow assay complete system of ssCro-DNA binding cascade for HPV detection

A lateral flow assay strip (Fig. 4.1) requires two lines. After inserting the sample on one end the test line will produce a color signal only upon target detection while a signal should always be visible at the control line site after the sample has ran, to verify the function of the device and minimize the possibility of false negatives. We used the EHD-jet printing method to print both lines of the biosensor. We decided to prepare strips with spots instead of lines using the near field electrospray method to compare the two methods.

Near field electrospray deposition

Initially with near-field electrospray we deposited the two required spots. Test spot consisting of streptavidin-biothynlated dHP DNA binding site complexand control spot consisting of scCro DNA binding protein. The electrospray conditions are presented in table 4.5 and the results after we run the HPV-DNA target and the carbon nanoparticles through the strips appear in Fig. 4.11.

Table 4.5

Q -liquid flow rate	0.03	(ml/hr)
Q_g- Gas flow rate	62	(ml/min)
H- tip to collector distance	3.5	(mm)
V_{HVPS}- Power Supply Voltage	8-9	(kV)
C_p – protein concentration	0.05	(mg/ml)
RH- Relative Humidity	34	(%)
T- Temperature	21	(ºC)
Composition	5% w/w glycerol in water	
t- Deposition time	240	(sec)

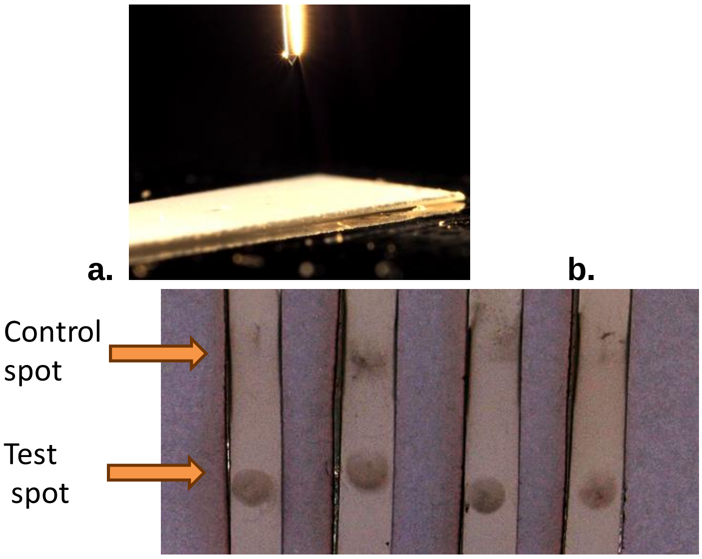

Figure 4.11: **a.** Near-field electrospray deposition on the strips, **b.** The latteral flow strips where a very fade circular spot appears for the test spot and almost no color for the control spot.

The test spots are unclear due to the spread of the capturing probes in the area of the spot that leads to colorimetric signal “dilution”. The control spots almost do not appear. The protein amount deposited for the control spot and for the test spot was the same for all strips, 150 ng and 250 ng respectively. We didn't proceed to the definition of the LOD as the control spot fails to appear.

EHD-jet direct printing method

The EHD-jet printing mode gave a much better result, as was expected from the initial HRP tests. The main reason is that for the same weight of deposited ssCro protein complex we get a much higher contrast that increases the limit of detection of the lateral flow assay biosensor (Fig. 4.12). The parameters of the experiment are provided in table 4.6.

Table 4.6

Q -liquid flow rate	1.4	(ml/hr)
Q_g- Gas flow rate	62	(ml/min)
H- tip to collector distance	7	(mm)
V_{HVPS}- Power Supply Voltage	8-9	(kV)
C_p – protein concentration	0.2	(mg/ml)
RH- Relative Humidity	34	(%)
T- Temperature	21	(ºC)
Composition	5% w/w glycerol in water	

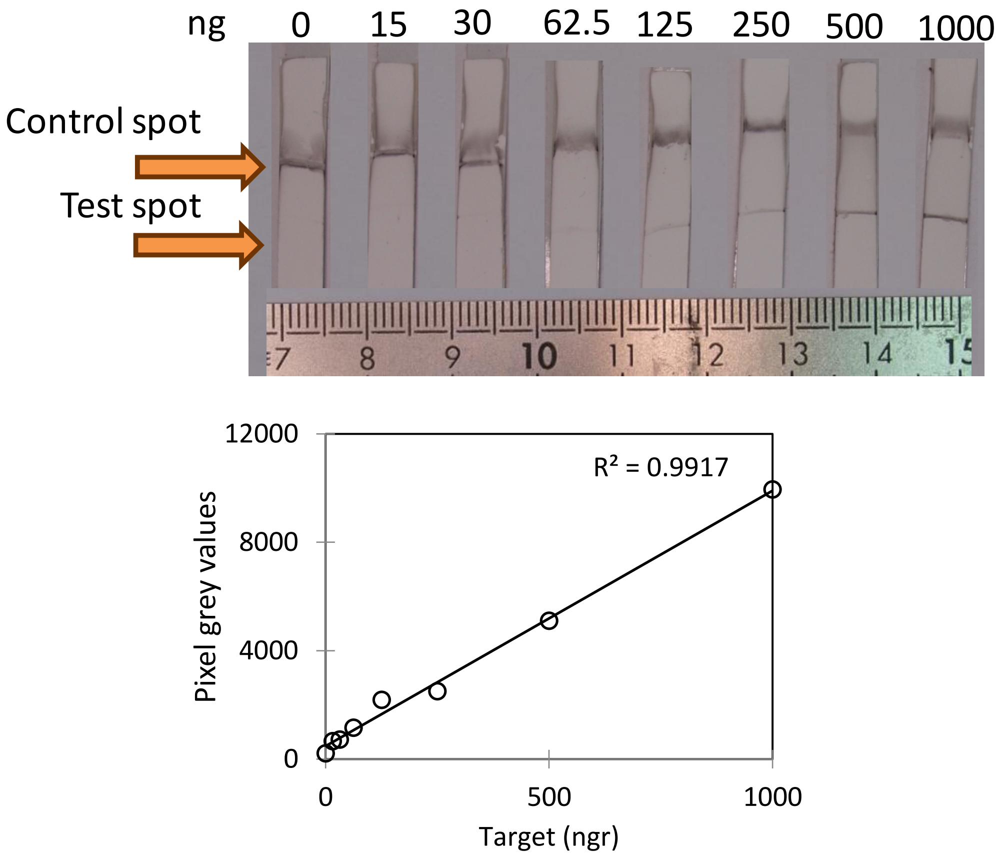

Figure 4.12: EHD-jet printed strips with both the control line and test line appearing. The numbers above the strips are the nanograms of target DNA on the sample per strip.

In Fig. 4.12 we see that all the control lines give a strong signal which means that the lateral flow assay runs normally. The amount of ssCro on the test line and the DNA-protein complex on the control line is 250 ng for all strips. The first faint control line appears at target DNA concentration 62.5 ng which sets approximately the DNA-target limit of detection. From the graph we see the signal intensity is linear to the amount of target DNA.

This is a functioning EHD-jet direct printed lateral flow biosensor able to detect an HPV DNA segment as a target. The ssCro protein used as a modular probe that can be easily modified for different DNA segments (Aktas et al., 2017).

The control lines of the strips prepared with near-field electrospray deposition method fail and we propose three possible mechanisms for that.

1) The target DNA is all captured in the test line and due to its wide surface.
2) The electrosprayed species of the control line are damaged during electrospraying.
3) Charge accumulates fast on the Ncw strip, due to the test line liquid properties, subsequently causing the electrosprayed droplets to avoid depositing on the strip surface.

The above assumptions remain to be tested in future work if “spots instead of lines” gain attention as a biosensor preparation standard.

4.4 Conclusions

In this paper we explore the capability of EHD techniques, for the direct printing on nitrocellulose paper of lateral flow assay biosensors. The main challenges we faced, regard depositing matter on non-conductive surfaces and electrospraying of water-based solutions

The direct deposition on paper has not been studied before in EHD literature and opens up new possibilities for insulating water absorbent materials to be used with this method (fabrics etc). In the case of cellulose or nitrocellulose paper the only requirement was a humid ambient. Even in the case of nitrocellulose with insulating support, artificial humidification was enough to create a charge diffusion path to ground and allow for EHD to function.

The co-flow system around the EHD emitter was essential for stabilizing a conical emission point of the used liquids for all the experiments. It is also supported by literature that the jet is better guided with a co-flow. This technique however has not been reported to our knowledge to be used for stabilizing long jets of aqueous liquids with no polymer content.

There are three techniques employed and compared which were electrospray deposition using a mask, near-field electrospraying and the newly developed EHD-jet direct printing.

In the first case of electrospray deposition with a mask we try to enforce the line pattern and much of the protein is wasted on the mask. One could argue that this material can be recycled and reused but still the time needed to deposit the required amount of protein on the small portion of surface uncovered by the mask increases the complexity and decreases the speed of the process.

For the second case of near field electrospray the main advantage of the electrospray technology, sought in other applications, becomes a disadvantage. The big liquid volume surface coverage, owing to the highly charged droplets repulsing each other, weakens the contrast of the produced spots. Essentially electrospray does the opposite of focusing the droplets on a spot, which dilutes the generated colorimetric signal. We were expecting to have better results in the enzymatic assay (HRP) that catalyzes the substrate and therefore the color signal, given substrate and time, should appear for the whole surface area covered, but as the experiment showed we had the similar colorimetric signal dilution effect comparing fig. 4.7 and 4.11.

The clear advantage of EHD techniques is that the jet diameter, therefore the print pattern resolution can be much smaller that the orifice diameter, preventing clogging of the emitter and increasing the robustness of the process. In the case of EHD-jet direct printing we got a good signal generation, good reproducibility and long-term stability between batches. The speed of printing is significantly reduced compared to electrospraying due to the higher flow rate. These reasons justify the EHD-jet printing technique as an alternative for printing colorimetric biosensor devices.

As a concluding remark we have manufactured, in one step, a functional LFA biosensor capable of detecting specific fragments of the HPV-DNA, using EHD deposition techniques. Furthermore, the detection platform that has been used can be modified to detect almost any DNA target, contributing to point-of-care diagnostics.

4.5 Acknowledgements

Aart von Amerongen for the Carbon nanoparticles, Wageningen Food & Biobased Research.
The URV groups Interfibio and DEW for providing the infrastructure, materials and space for the experimentation. Specifically Dr Vasso Skpuridou, Prof. Lluis Massip and Dr Joan Rosell for the support.

4.6 References

Aktas, G.B., Skouridou, V., and Masip, L. (2017). Nucleic acid sensing with enzyme-DNA binding protein conjugates cascade and simple DNA nanostructures. Anal. Bioanal. Chem., 409(14):3623–3632. https://doi.org/10.1007/s00216-017-0304-z

Carrilho, E., Martinez, A. W., & Whitesides, G. M. (2009). Understanding wax printing: A simple micropatterning process for paper-based microfluidics. Analytical Chemistry, 81(16), 7091–7095. https://doi.org/10.1021/ac901071p

Gonzalez-Macia, L., Morrin, A., Smyth, M. R., & Killard, A. J. (2010). Advanced printing and deposition methodologies for the fabrication of biosensors and biodevices. Analyst, 135(5), 845–867. https://doi.org/10.1039/b916888e

Gomez, A., Bingham, D., De Juan, L., and Tang, K. (1998). Production of protein nanoparticles by electrospray drying. J. Aerosol Sci., 29(5–6):561–574.

He, G., Zheng, G., Zheng, J., Lin, Y., Wei, J., Liu, H., Sun, D. (2013). Micro/nano structure written via sheath gas assisted EHD jet. 8th Annual IEEE International Conference on Nano/Micro Engineered and Molecular Systems, IEEE NEMS 2013, 1, 625–628. https://doi.org/10.1109/NEMS.2013.6559807

Jayasinghe, S. N., & Townsend-Nicholson, A. (2006). Stable electric-field driven cone-jetting of concentrated biosuspensions. Lab on a Chip, 6(8), 1086–1090. https://doi.org/10.1039/b606508m

Kalodimos, C.G., Folkers, G.E., Boelens, R., and Kaptein, R. (2001). Strong DNA binding by covalently linked dimeric Lac headpiece: Evidence for the crucial role of the hinge helices. Proc. Natl. Acad. Sci. U. S. A., 98(11):6039–6044.

Khan, A., Rahman, K., Kim, D.S., and Choi, K.H. (2012). Direct printing of copper conductive micro-tracks by multi-nozzle electrohydrodynamic inkjet printing process. *J. Mater. Process. Technol.,* 212(3):700–706.

Koczula, K. M., & Gallotta, A. (2016). Lateral flow assays, (June), 111–120. https://doi.org/10.1042/EBC20150012

Li, J., Rossignol, F., and Macdonald, J. (2015). Inkjet printing for biosensor fabrication: Combining chemistry and technology for advanced manufacturing. *Lab Chip,* 15(12):2538–2558.

Loh, O. Y., Ho, A. M., Rim, J. E., Kohli, P., Patankar, N. A., & Espinosa, H. D. (2008). Electric field-induced direct delivery of proteins by a nanofountain probe. Proceedings of the National Academy of Sciences, 105(43), 16438–16443. https://doi.org/10.1073/pnas.0806651105

Lübbert, C. and Peukert, W. (2018). The mass transfer at Taylor cones. J. Aerosol Sci., 123:39–51.

Morbioli, G. G., Mazzu-Nascimento, T., Stockton, A. M., & Carrilho, E. (2017). Technical aspects and challenges of colorimetric detection with microfluidic paper-based analytical devices (μPADs) - A review. Analytica Chimica Acta, 970, 1–22. https://doi.org/10.1016/j.aca.2017.03.037

Morozov, V. N. (2009). Electrospray depostion of biomolecules. Advances in Biochemical Engineering/Biotechnology, 123(July 2015), 127–141. https://doi.org/10.1007/10

Morozov, V. N., & Morozova, T. Y. (1999 a). Electrospray deposition as a method to fabricate functionally active protein films. Analytical Chemistry, 71(7), 1415–20. https://doi.org/10.1021/ac9808775

Morozov, V. N., & Morozova, T. Y. (1999 b). Electrospray Deposition as a Method for Mass Fabrication of Mono- and Multicomponent Microarrays of Biological and Biologically Active Substances, 71(15), 3110–3117.

Shigeta, K., He, Y., Sutanto, E., Kang, S., Le, A.P., Nuzzo, R.G., Alleyne, A.G., Ferreira, P.M., Lu, Y., and Rogers, J.A. (2012). Functional protein microarrays by electrohydrodynamic jet printing. Anal Chem, 84(22):10012–10018.

Sun Ju-Yen, Cheng Chao-Min, Liao Ying-Chih (2015). Screen printed paper-based diagnostic devices with polymeric inks. Analytical Sciences, 31(3), 145-151.

Pabo, C.O. and Sauer, R.T. (1984). Protein-DNA Recognition. Annu. Rev. Biochem., 53(1):293–321.

Posthuma-Trumpie, G.A., Korf, J., and van Amerongen, A. (2009). Lateral flow (immuno)assay: its strengths, weaknesses, opportunities and threats. A literature survey. Anal. Bioanal. Chem., 393(2):569–582.

Tse, L., and Barton, K. (2015). Airflow Assisted Electrohydrodynamic Jet Printing: An Advanced Micro-Additive Manufacturing Technique., Conference paper, Msec2015, Volume 1, 1–8. doi:10.1115/MSEC2015-9403

Wu, X., Suvarnapathaki, S., Walsh, K., & Camci-Unal, G. (2018). Paper as a scaffold for cell cultures: Teaching an old material new tricks. MRS Communications, 8(1), 1–14. https://doi.org/10.1557/mrc.2018.8

Zheng, J., Zhang, K., Jiang, J., He, G., Xu, L., Liu, Y., Zheng, G. (2016). Electrohydrodynamic direct-writing orderly pattern with sheath gas focusing. AIP Advances, 6(11), 115304. https://doi.org/10.1063/1.4967342

Patent: US20110187798A1, Rogers J. A., Park Jang-Ung, Ferreira Placid M., Deepkishore Mukhopadhyay, Original Assignee University of Illinois Priority date 2007-07-19.

Chapter 5

Conclusions

In the second chapter we have developed and characterized a linear electrospray system. First, we have gained physical insights into the question of scalabilility from electric field computations of arrays of lines-of-charge These computations have revealed that the electric field at the edge of the array does not increase indefinitely as the array grows. Instead, the field converges towards a plateau value as the number of lines increases, and such plateau is approached when the width of the array is as small as the plate's gap. Experiments have confirmed that the electrostatic field experienced by the central region of very long arrays is not dependent of how long the array is. So, the array is expandable indefinitely while the needed voltage is bounded, averting gas breakdown discharges. We have shown this for arrays characterized by a small pitch of 2.5 mm (4 emitters/cm) and a collector distance as large as 13 mm.

We have identified as optimal linear array configurations the ones having on either end two non-spraying electrodes, positioned at the same pitch as the spraying emitters; A passive (non-spraying) emitter in the innermost position and a much thicker electrode in the outermost position, to prevent the appearance of gas discharges at that location.

An individual current measurement per emitter has been used to identify the spray mode transitions, functioning as an excellent diagnostic of system stability.

We have also reported on "symmetry breaking" of the electrosprays, observed at high enough voltage, caused by the tilting of the Taylor cones it has been identified that those directions correlate with the slight emitters' misalignments when they have a zig-zag pattern, with the jets roughly pointing in the direction of strongest field strength. In absence of a pattern, other factors are important in this phenomenon, as, sometimes, the array end sprays point inward toward the array, instead of outward where the field is most intense. These experiments suggest that symmetry breaking may be exploited to actively control the collection of the generated droplets/particles.

In chapter 3 we have applied the Linear Electrospray System (LEsS) know-how and used the linear array in hand, to demonstrate the production of polymer particles loaded with an Active Pharmaceutical Ingredient (API). The "symmetry breaking" is avoided here by deflecting the Taylor cones direction with a horizontal electrode and create a uniform deposition pattern in orderly spots, facilitating the collection of the deposited matter.

Two different polymers (ethyl cellulose and PVP) have been used to produce micro/nano particles of various morphologies demonstrating the particle engineering capability of the LEsS. Curcumin was chosen as a model API. Curcumin is intensively researched for its therapeutical properties but suffers from low bioavailiability due to its insolubility in water.

The proposed PVP – curcumin formulation facilitates the dissolution in water. Furthermore, decreasing the particle sizes below 1 micrometer is expected to improve the API absorption through the gastrointestinal tract.

While working with this system we came upon an interesting discovery; paper can be used as an electrospray collector. Paper is first time reported to be suitable for particle collection in the stable cone jet mode. It is not only the low cost and wide availability of paper as a material, that has a practical value, but, we are also implored to investigate other water absorbing, porous, materials (i.e. fabrics) traditionally considered “bad” collectors for possible use as electrospray collectors.

Regarding the scale-up capability of a LEsS; we have operated up to 11-emitters. From our previous work (chapter 1) it is shown that the system can be scaled up to a very large number of simultaneously operating emitters. A 1000 emitter LEsS (assuming consistent operation) could produce 1.13 gr / hour of particulate matter, with an array length of 2.5 m. Stacking up of LEsS units is also a possibility for decreasing the footprint of the system.

In chapter 4 we tinker with the idea of EHD deposition on paper. A collaboration was initiated with the InterfiBio group and EHD deposition methods were investigated for the deposition of proteins on nitrocellulose paper for lateral flow assay biosensors. In the case of cellulose or nitrocellulose paper the only requirement has been found to be a humid ambient. Even in the case of nitrocellulose with insulating support, artificial humidification plus a connection to ground, has been enough to create a charge diffusion layer to the electrical ground and allow for EHD to function. The co-flow system around the EHD emitter has been essential for stabilizing a conical emission point in all the experiments.

Three deposition techniques have been used and compared in this final part: electrospray deposition using a mask, near-field electrospraying and the newly developed EHD-jet direct printing. In the case of electrospray deposition with a mask when trying to enforce the line pattern some amount of the protein is deposited on the mask. One could argue that this material can be recycled and reused but still the time needed to deposit the required amount of protein on the small portion of surface uncovered by the mask increases the complexity and decreases the speed of the process.

In the case of near field electrospray, the capability of great uniform dispersion of this technology, sought in other applications, seems to have adverse effects. The high surface coverage, owing to the highly charged droplets repulsing each other, weakens the contrast of the colorimetric signal of the deposited spots. Specifically for the ssCro protein complex, the signal is proportional to the immobilized carbon nanoparticles per DNA target detected. We also experimented with the (HRP) enzymatic assay that essentially catalyzes the amount of substrate offered and theoretically should amplify the colorimetric signal but, the experiment showed we still have had the signal dilution effect.

In the case of EHD-jet direct printing we have obtained a good signal generation and good reproducibility between batches. The speed of printing is significantly reduced comparing to the above two methods due to the higher flow rate. These reasons justify in our opinion the consideration of this technique for printing colorimetric biosensor devices. An added value to this technique is that the jet diameter therefore the print pattern resolution can be much smaller that the orifice diameter, therefore preventing clogging and increasing the robustness of the device. In conclusion we successfully produced a DNA specific lateral flow biosensor using the EHD-jet direct printing method.